11

AD 746457

PROJECT SQUID

TECHNICAL REPORT UARL-1-PU

ANALYSIS OF UNSTEADY AERODYNAMIC EFFECTS ON AN AXIAL-FLOW COMPRESSOR STAGE WITH DISTORTED INFLOW

BY

FRANKLIN O. CARTA
UNITED AIRCRAFT RESEARCH LABORATORIES
EAST HARTFORD, CONNECTICUT

DDC
RECEIVED
AUG 14 1972
B

PROJECT SQUID HEADQUARTERS
JET PROPULSION CENTER
SCHOOL OF MECHANICAL ENGINEERING
PURDUE UNIVERSITY
LAFAYETTE, INDIANA

JULY 1972

Project SQUID is a cooperative program of basic research relating to Jet Propulsion. It is sponsored by the Office of Naval Research and is administered by Purdue University through Contract N00014-67-A-0226-0005, NR-098-038.

This document has been approved for public release and sale;
its distribution is unlimited.

Rep[illegible]
NATIONAL TECHNICAL
INFORMATION SERVICE
[illegible] of Commerce
[illegible] 22151

124

Unclassified
Security Classification

DOCUMENT CONTROL DATA - R&D

(Security classification of title, body of abstract and indexing annotation must be entered when the overall report is classified)

1 ORIGINATING ACTIVITY *(Corporate author)*
Project SQUID
Jet Propulsion Center
Purdue University, Lafayette, Indiana 47907

2a REPORT SECURITY CLASSIFICATION
Unclassified

2b GROUP
N/A

3 REPORT TITLE

Analysis of Unsteady Aerodynamic Effects on an Axial-Flow Compressor Stage with Distorted Inflow

4 DESCRIPTIVE NOTES *(Type of report and inclusive dates)*
Technical Report

5 AUTHOR(S) *(Last name, first name, initial)*

Carta, Franklin O.

6 REPORT DATE
July 1972

7a TOTAL NO OF PAGES
126

7b. NO. OF REFS
13

8a CONTRACT OR GRANT NO.
N00014-67-A-0226-0005

b PROJECT NO.
NR-098-038

c

d

9a ORIGINATOR'S REPORT NUMBER(S)

UARL-1-PU

9b OTHER REPORT NO(S) *(Any other numbers that may be assigned this report)*
UARL Report L911103-4

10 AVAILABILITY/LIMITATION NOTICES
This document has been approved for public release and sale; its distribution is unlimited.

11 SUPPLEMENTARY NOTES
N/A

12. SPONSORING MILITARY ACTIVITY
Power Branch, Code 473
Department of the Navy
Arlington, Virginia 22217

13 ABSTRACT

An analytical procedure has been developed to predict the circumferential pressure profile at the exit of a compressor stage subjected to a spatially steady inlet distortion. Expressions have been developed relating the pressure ratio and weight flow characteristics of an axial-flow compressor stage to the normal force and drag characteristics of an isolated airfoil. These steady-state interrelations between rotor and isolated airfoil were used to apply available unsteady data for isolated airfoils in the study of distorted inflow effects. Both unsteady and quasi-steady predictions were made and were compared with available experimental results from low-speed compressor tests. It was found that, in general, the unsteady predictions are in better agreement with experiment than the quasi-steady predictions, but there are regions where both theories are in significant disagreement with the data. The results of the work reported herein have led to an improved analytical model which is briefly reviewed. Further analytical work, based on this improved model, will be the subject of future reports.

Unclassified
Security Classification

14 KEY WORDS	LINK A		LINK B		LINK C	
	ROLE	WT	ROLE	WT	ROLE	WT
Inlet distortion analysis						
Compressor response to stationary inlet distortion						
Circumferential distortion						
Unsteady fluid dynamic analysis						

DD FORM 1 NOV 65 **1473** (BACK)
S/N 0101-807-6821

Unclassified
Security Classification

United Aircraft Research Laboratories

UNITED AIRCRAFT CORPORATION

EAST HARTFORD, CONNECTICUT 06108

Project SQUID Technical Report UARL-1-PU

ANALYSIS OF UNSTEADY AERODYNAMIC EFFECTS ON AN AXIAL-FLOW COMPRESSOR STAGE WITH DISTORTED INFLOW

REPORTED BY Franklin O. Carta
Franklin O. Carta

APPROVED BY M. C. Cheney
M. C. Cheney, Chief
Aerodynamics Section

Work performed under Contract No. 4965-32
for Project SQUID (Subcontract under
ONR Contract N00014-67-0226-0005,
NR-098-038).

July 1972

TABLE OF CONTENTS

Page

SUMMARY. 1

INTRODUCTION 2

FLUID DYNAMIC ANALYSIS 5

  Assumptions Made in the Analysis. 5
  Quasi-Steady Flow Through a Blade Row 6
  Use of Unsteady Aerodynamic Data. 10

APPLICATION TO A COMPRESSOR ROTOR. 12

  Description of UARL Three-Stage Compressor Rig. 12
  Detailed Study of a Single Distorted Flow Condition 13
  Additional Distortion Profiles. 18
  Stage Pressure Rise 21
  Possible Sources of Error 24

CONCLUSIONS AND BRIEF REVIEW OF FUTURE WORK. 28

ACKNOWLEDGMENT 31

REFERENCES 32

LIST OF SYMBOLS. 34

APPENDIX I DERIVATION OF THE QUASI-STEADY FLUID DYNAMICS THROUGH A BLADE ROW 38

APPENDIX II CONVERSION OF STEADY-STATE COMPRESSOR CHARACTERISTICS TO ROTOR BLADE LIFT AND DRAG. 45

APPENDIX III UNSTEADY LIFT SCALING PROCEDURES. 50

APPENDIX IV UNSTEADY DRAG HYPOTHESIS AND SCALING PROCEDURES . . 55

APPENDIX V CALCULATION PROCEDURES. 62

APPENDIX VI RADIAL EQUILIBRIUM CORRECTION 70

TABLE I. 71

FIGURES. 72

Analysis of Unsteady Aerodynamic Effects on an Axial-Flow Compressor Stage With Distorted Inflow

SUMMARY

An analytical procedure has been developed to predict the circumferential pressure profile at the exit of a compressor stage subjected to a spatially steady inlet distortion. Expressions have been developed relating the pressure ratio and weight flow characteristics of an axial-flow compressor stage to the normal force and drag characteristics of an isolated airfoil. These steady-state interrelations between rotor and isolated airfoil were used to apply available unsteady data for isolated airfoils in the study of distorted inflow effects. Both unsteady and quasi-steady predictions were made and were compared with available experimental results from low-speed compressor tests. It was found that, in general, the unsteady predictions are in better agreement with experiment than the quasi-steady predictions, but there are regions where both theories are in significant disagreement with the data. The results of the work reported herein have led to an improved analytical model which is briefly reviewed. Further analytical work, based on this improved model, will be the subject of future reports.

INTRODUCTION

The performance of an axial-flow compressor can be seriously compromised by the presence of a nonuniform circumferential velocity distribution in the inlet of the compressor. Such an inlet velocity distortion could be caused by a poorly designed engine inlet, flow separation from some portion of the inlet cowl arising from a locally large incidence angle, or even by scavenging of a thick boundary layer from some adjacent aerodynamic surface. Whatever the cause, the primary effect will generally be the same; viz., if there exists, circumferentially, some region of reduced axial velocity, a compressor blade travelling at a constant rotational speed will experience a periodic change in incidence angle, as shown in Fig. 1. The aerodynamic performance of a blade in a distorted flow will depart from that for some nominal operating condition; the degree of this departure will depend largely on such parameters as the number of distortions per revolution, the circumferential extent of each distortion, the magnitude of each distortion, and the rate at which incidence angle changes due to the distortion take place. A change in compressor blade performance from some nominal value will affect the overall performance of the compressor stage. In many cases a distortion is severe enough to affect the performance of the entire engine to the extent that the engine surge margin will be compromised.

Current techniques for predicting engine stability with a distorted inflow treat the problem as quasi-steady and thus employ steady-state stage characteristics. These techniques assume that the compressor blading responds instantaneously to distortion-induced changes in the incidence angle. The response of a compressor blade to a rapid change in inflow is, in fact, a nonsteady phenomenon that is far from instantaneous. This is indicated by the results shown in Fig. 2 which were taken from Ref. 1. In this study, circumferential distortions having a total circumferential extent of 180 deg were configured in three possible ways: (a) a single 180 deg distortion, (b) two radially opposed 90 deg distortions, or (c) four equally spaced 45 deg distortions. This figure shows that the surge pressure ratio (plotted vertically) is strongly affected by the change in circumferential extent of each portion of the distortion, even though the total circumferential extent of the distortion remained invariant. (This observation is further substantiated by the results shown in Fig. 2 of Ref. 2 in which the total circumferential extent of the distortion was 90 deg.)

The sensitivity of compressor characteristics noted above to the time rate of change of the distortion pattern (as observed in the relative system of the blades) was anticipated by the analysis of unsteady aerodynamic blade response to variations in angle of attack described in Ref. 3. In this work use was made of a body of unsteady aerodynamic data for an isolated airfoil oscillating both in potential flow and well into the stall regime. By applying these unsteady aerodynamic data to a hypothetical distortion, the analysis examined the response of a compressor blade to several distortion variables, including time rate of the distortion pattern and degree of penetration into the stall regime. This preliminary analysis predicted the expected enhancement in lift and, within its limited framework, implied the resulting pressure rise that can result from certain distortion patterns, as well as the flow breakdown from other patterns.

The current investigation is directed toward assessing the extent to which the characteristics of compressors operating in distorted flow are influenced by unsteady aerodynamic effects. In this analysis, refinements have been made to the techniques of Ref. 3 to permit a more complete prediction of the characteristics of a compressor in an arbitrarily distorted inlet flow. In addition to refining the unsteady lift prediction developed in Ref. 3, a method for converting these results to stage pressure rise has also been developed, and results have been compared with available experimental data.

This report covers the results obtained during the first year of this contract. This includes the derivation of the basic fluid dynamic equations and the comparison between the predicted and measured unsteady compressor performance. Subsequent reports will cover the continuation of this analysis including an examination of the assumptions made in this first study and refinements made to the theory.

FLUID DYNAMIC ANALYSIS

Assumptions Made in the Analysis

The problem under consideration in this report involves the nonuniform flow of fluid through a compressor blade row. In its most general form this problem is virtually impossible to solve, and it is necessary to reduce its scope considerably to make it tractable. One essential characteristic of the problem is that a compressor blade row is moving at constant rotational speed through a fluid medium having a variable vector velocity. As described in the Introduction, this produces a time-varying angle of attack on the individual compressor blades, and it is this essential nonsteady characteristic that will be studied in the present report, although other elements of the problem will be simplified for clarity.

In the analysis which follows, a number of fundamental assumptions have been made to simplify this first effort at finding a solution. These assumptions are listed below.

1. The flow is inviscid and incompressible.
2. The flow through each blade passage is quasi-steady.
3. The axial velocity at any circumferential station is constant through the stage.
4. All cascading effects can be satisfactorily accounted for by the steady-state cascade characteristic.

5. The flow through adjacent blade passages is periodic.
6. Three-dimensional radial effects are negligible although radial equilibrium corrections are applied to the measured static pressure.
7. Unsteady effects manifest themselves at the exit plane through the unsteady aerodynamic response of the blading only.
8. Unsteady stalling on a cascade blade can be modeled from the unsteady stalling response of an isolated blade.
9. Unsteady drag can be computed as a departure from the steady drag, proportional to the unsteady lift departure from steady lift.

Quasi-Steady Flow Through a Blade Row

The blade row to be analyzed here is shown in Fig. 3 together with some of the nomenclature to be used. Station 1 is located at the blade row entrance plane and station 2 is located at the exit plane. The tangential blade gap is τ and the blade chord is $c = 2b$. The blade is oriented at a fixed chord angle, α_{CH}, relative to the tangential direction. Axial quantities are denoted by the subscript A and tangential quantities by the subscript Ω. The two right-hand velocity triangles are drawn for the absolute reference frame, stationary in space, and consist of the absolute velocity, V_o, the wheel speed, U, and the relative velocity, V. These quantities are subscripted 1 and 2 for entrance and exit, respectively. The left-hand velocity triangles are included for convenience and denote the quantities of major interest in the relative frame of reference which are the relative velocity, V, the axial velocity, V_A, and the tangential swirl component, V_Ω. The total force on each blade is denoted by F and is resolved into axial and tangential components, F_A and F_Ω, or into lift and drag components, L and D. For this analysis the lift is assumed to act normal to the inlet relative velocity vector, V_1.

In Fig. 4 the inlet and exit velocity triangles are shown in more detail. The absolute components are shown as solid vectors and the axial and tangential swirl components are shown as dashed vectors. In this diagram all angles are measured relative to the tangential direction. The angle of the relative velocity is denoted by β, and that of the absolute velocity is denoted by α. In addition, the yaw angle, α_y, of the inlet absolute velocity is shown on the inlet triangle. (This angle is the supplement to α_1.)

For a given inlet distortion the circumferential variations of the inlet total and static pressures, P_{01} and p_1, and of the inlet yaw angle, α_y, will be given quantities, usually obtained from an experiment. In keeping with the assumptions listed in a previous section, the steady form of Bernoulli's equation will be used to compute the instantaneous velocity magnitude into the blade row at any circumferential position, θ ,

$$p_1(\theta) + \frac{1}{2}\rho V_{01}^2(\theta) = P_{01}(\theta) \tag{1}$$

Note that the density is unsubscripted in accordance with the assumption that the flow is incompressible. This equation may be solved now for the absolute inlet velocity,

$$V_{01}(\theta) = \sqrt{\frac{2}{\rho}\left(P_{01}(\theta) - p_1(\theta)\right)} \qquad (2)$$

The aerodynamic force response of the rotor blades will depend on the circumferential variation in the inlet air angle, β_1. From the inlet velocity triangle of Fig. 4 it is easily shown that

$$V_{A_1}(\theta) = V_{01}(\theta) \sin \alpha_y(\theta) \qquad (3)$$

$$V_{\Omega_1}(\theta) = U + V_{01}(\theta) \cos \alpha_y(\theta) \qquad (4)$$

and hence

$$\beta_1(\theta) = \tan^{-1} \frac{V_{A_1}(\theta)}{V_{\Omega_1}(\theta)} = \tan^{-1}\left[\frac{V_{01}(\theta)\sin \alpha_y(\theta)}{U + V_{01}(\theta)\cos \alpha_y(\theta)}\right] \qquad (5)$$

It is more convenient to calculate blade aerodynamic response from the rotor blade angle of attack, α_R, which is shown in the upper half of Fig. 5 to be

$$\alpha_R(\theta) = \alpha_{CH} - \beta_1(\theta) \qquad (6)$$

The procedure to be followed in this analysis is as follows. From the circumferential variation of the inlet pressures and yaw angle we can calculate V_{01} from Eq. (2), β_1 from Eq. (5) and α_R from Eq. (6). If the compressor wheel rotates at a constant rate $\Omega = d\theta/dt$ then $\theta = \Omega t$ and these quantities become time histories. From the time history of α_R it is possible to enter a table of unsteady aerodynamic lift and drag data appropriate to the rotor blade and obtain unsteady lift and drag time histories versus θ. Details of this procedure will be given in a subsequent section. Next the lift and drag forces can be resolved into axial and tangential force components (see bottom of Fig. 5) from the equations

$$\begin{aligned} F_A(\theta) &= L(\theta)\cos\beta_1(\theta) - D(\theta)\sin\beta_1(\theta) \\ F_\Omega(\theta) &= L(\theta)\sin\beta_1(\theta) + D(\theta)\cos\beta_1(\theta) \end{aligned} \tag{7}$$

Further details of the quasi-steady through-flow analysis are given in Appendix I. Use is made of the continuity and momentum equations to obtain formulas for the static and total circumferential pressure distributions at the rotor exit plane, which are repeated below for convenience.

$$p_2(\theta) = p_1(\theta) + \frac{\rho V_1^2(\theta)}{2\,\tau/c}\; C_{F_A}(\theta) \tag{8}$$

$$P_{02}(\theta) = p_2(\theta) + \frac{1}{2}\rho\left[V_A^2(\theta) + \left(U - V_{\Omega_1}(\theta) + \frac{V_1^2(\theta)\, C_{F\Omega}(\theta)}{2(\tau/c)\, V_A(\theta)}\right)^2\right] \qquad (9)$$

In these equations C_{F_A} and C_{F_Ω} are the axial and tangential force coefficients, given by

$$C_{F_A} = \frac{F_A}{\frac{1}{2}\rho V_1^2 c \ell}$$

$$C_{F_\Omega} = \frac{F_\Omega}{\frac{1}{2}\rho V_1^2 c \ell} \qquad (10)$$

Use of Unsteady Aerodynamic Data

In attempting a solution of the unsteady inlet distortion problem, the unsteady lift and drag data which should be used should ideally be obtained for blades in cascade operating into the stall regime. Unfortunately such data are not available for cascades, and, moreover, there is no known body of unsteady drag data obtained on any lifting surface. An attempt has been made in the present analysis to overcome these deficiencies in the data by using available unsteady lift data on an isolated airfoil and by hypothesizing a reasonable unsteady drag model. Suitable transformations have been made to convert these isolated airfoil forces into their equivalent cascade counterparts, as described below. This approximation is justifiable in view of the total lack of unsteady cascade data, and the analysis is so structured that if cascade data were to become available it would be a simple matter to insert it in place of the isolated airfoil data.

A number of steps are required to introduce the available unsteady lift data for the isolated airfoil into the pressure equation to represent the unsteady lift on a rotor blade. These steps are summarized briefly in this paragraph to indicate how all of the parts fit together, and the details of each step are discussed in Appendix II. First the equations must be derived that relate steady-state cascade blade lift to compressor blade performance. This is done by manipulating Eqs. (7), (8), and (9) together with other relevant equations. Next a scaling law must be determined that will relate the lift on a cascaded airfoil to the lift on the isolated airfoil (see Appendix III). The unsteady isolated airfoil lift must then be introduced and scaled to yield an incremental change in the unsteady rotor blade lift which will subsequently be used to calculate the unsteady rotor pressure response. A similar procedure for scaling unsteady drag and details of the unsteady drag hypothesis are in Appendix IV.

A complete summary of all of these steps, including the sequence of computer operations, is in Appendix V.

APPLICATION TO A COMPRESSOR ROTOR

Description of UARL Three-Stage Compressor Rig

The brief description which follows of the three-stage compressor rig is included in the present report to assist the reader to understand the experimental data discussed later. It does not purport to be a detailed description of this facility, nor does it attempt to provide extensive coverage of the experimental results obtained.

The three-stage rig is a low-speed, low-pressure facility consisting of an inlet bellmouth, inlet guide vanes (IGV), and three conventional rotor-stator stages. The rotating parts were driven by a 500 hp dc electric motor. The airflow passage has an outer diameter of 24 inches, and the hub-to-tip ratio for the tests described herein was 0.7. A centerline section drawing is presented in Fig. 6, approximately to scale. The rotors are denoted by R1, R2, R3, and the stators by S1, S2, S3. The instrumentation stations are numbered above the drawing, and the pressure instrumentation used at each station is shown in the sketches at the bottom of the figure. Total pressure measurement locations are denoted by the circled points and static pressure measurement locations by the diamond points. In addition, yaw probes (not shown) were used to make flow angle measurements at the entrance to each rotor. The distortion screen was located in a constant area region of the annulus ahead of the IGV and consisted of an annular segment of thin perforated plate (approximately 50 percent porosity). The segment angle of most concern in the present study was 180 deg, although tests were also run with distortion screens of 90 deg and 135 deg angular extent.

The normal test procedure was to first obtain a baseline characteristic with no distortion by varying the downstream throttle and making pressure measurements at a constant speed condition. This is shown in Fig. 7 (and is described in Appendix II) for the first stage. A distortion screen was then inserted and measurements were made at the same rotor speed and at some fixed downstream throttle setting, representative of a given undistorted point on the characteristic curve. Because there were only eight circumferential measuring stations for each axial station, it was necessary to repeat this test a number of times with the distortion screen incremented circumferentially each time. Typically, a total of 10 or more test points might be taken to obtain the desired circumferential pressure variations.

Detailed Study of a Single Distorted Flow Condition

In the performance of this work a number of distorted flow conditions were studied, and many variants to the analysis were introduced, both to improve the correlation between analysis and test and to provide a deeper insight of the mechanisms involved. In this report we shall consider one of these distorted flow conditions in considerable depth. In addition, a more general discussion will follow in a later section of other cases considered in this study, and of the sensitivity of the results to variations in the inlet parameters. In all cases the analysis was confined to the first stage only.

In this detailed discussion we shall be concerned with a 180 deg distortion of the inlet flow with the compressor operating at the peak pressure point. If no distortion had been present this point would have been near the maximum point on the rotor $\phi - \psi$ curve in Fig. 7. The measured circumferential mid-annulus total pressure profiles at the rotor inlet and exit planes are shown in Fig. 8, the outer diameter static pressure profiles at the rotor inlet, rotor exit, and stator exit planes are shown in Fig. 9, and the yaw angle profile at the rotor inlet plane is shown in Fig. 10. The total pressure was measured in a stationary frame of reference so there is no significant change in total pressure from rotor exit to stator exit. The pressure profiles are plotted relative to the local atmospheric total pressure which in this case is $P_{ref} = 404.33$ in. H_2O. The position of the screen, which extended from $\theta = 270$ deg to $\theta = 90$ deg, is indicated by the shaded region along the abscissa of these and subsequent figures.

The procedures outlined above and in Appendix V were followed, and the pressure difference $P_{01}(\theta) - p_1(\theta)$, together with the yaw angle variation, were used to calculate the dimensionless stall angle parameter, σ, shown in Fig. 11 (where $\sigma > 1$ is above the stall angle and $\sigma < 1$ is below the stall angle). It is seen that the rotor blade operates above stall over most of the circumference, particularly in the regions behind the screens. This distribution was numerically differentiated to obtain the dimensionless angular velocity and angular acceleration parameters, A and B, as described in Appendix III, and unsteady lift and drag data on the rotor blade were obtained. These are shown in Figs. 12 and 13, respectively, where the unsteady result (solid line) is compared with the quasi-steady result (dashed line). The latter was obtained by setting A = B = 0 and performing the analysis.

It can be seen that there are large differences between the quasi-steady and the unsteady results over much of the range of operation in both Figs. 12 and 13. The only region where the quasi-steady and the unsteady results agree is the circumferential range $200 < \theta < 240$ deg. In that region σ has a consistently small gradient, as shown in Fig. 11. Very large fluctuations occur near the edges of the screen, particularly for the lift. This is most likely artificially caused by the magnification of error that occurs when a function that is not perfectly smooth is numerically differentiated. In the analysis and discussion that follows these effects are discounted, and we feel it will be possible to modify the analytical model in the future to overcome these wide excursions.

Let us consider, in greater detail, the large differences between the quasi-steady and the unsteady results. As suggested above, we will exclude from the present discussion the regions of very rapid change near the screen edges. In the region behind the screen, over the range $-40 < \theta < 40$ deg (or, using the θ values in Figs. 11, 12, and 13, 320 deg $<\theta$ and $\theta<40$ deg), σ is a steadily increasing function, and in this region the unsteady lift is greater than the quasi-steady lift, and the unsteady drag is smaller than the quasi-steady drag. Conversely, in the region of no screen, over the range $115<\theta<200$ deg, σ is a steadily decreasing function, and in this region the unsteady lift is smaller than the quasi-steady lift, and the unsteady drag is greater than the quasi-steady drag. The enhancement of the unsteady lift for increasing angle of attack and the deterioration of lift for decreasing angle of attack are to be expected in this high angle of attack regime (Ref. 3). The noted changes in unsteady drag appear to be reasonable when related to the lift behavior. These differences have a great deal of bearing on the prediction of the unsteady exit pressures for the rotor.

The circumferential rotor lift and drag variations were next transformed to axial and tangential force variations, which were then inserted into Eqs. (8) and (9) to predict the circumferential static and total pressure profiles at the rotor exit. This was done for both the quasi-steady and the unsteady conditions and the results are shown in Figs. 14 and 15 for the total and static pressures, respectively. The parameters used in the analysis leading up to Eqs. (8) and (9) were obtained at mid-annulus, and hence the predicted pressure profiles in Figs. 14 and 15 also represent mid-annulus values. The exit total pressures were measured at mid-annulus, and are shown in Fig. 14 as circled points. However, the measured static data were obtained from sidewall taps on the outer diameter and had to be corrected by a radial equilibrium criterion to yield mid-annulus results. This was done using the formula derived in Appendix VI and the results are plotted as the circled points in Fig. 15.

First consider the total pressure prediction in Fig. 14. The unsteady theory is in better agreement with the experimental data than the quasi-steady theory over most of the range $0 < \theta < 270$ deg. The sole exception here is the exit from behind the screen in the vicinity of $\theta = 90$ deg. At the entrance to the screen, over the range $270 < \theta < 360$ deg, both theories are in substantial disagreement with experiment. The static pressure comparison is shown in Fig. 15 and again it is seen that over much of the circumference (with the exception of the two screen edges and a small region surrounding $\theta = 0$ deg) the unsteady theory is consistently in better agreement with the measured results than is the quasi-steady prediction. Furthermore, over much of the range excellent agreement is achieved using the unsteady theory. However, this agreement tends to be masked by the large changes in both the unsteady and quasi-steady pressure profiles due to the circumferential changes in the inlet pressures.

Some of these masking effects can be eliminated by plotting the rotor static pressure coefficient, ψ_R, as a function of θ. This was computed from Eq. (40) in Appendix II using the measured, the quasi-steady, and the unsteady circumferential inlet and exit static pressure profiles, $p_1(\theta)$ and $p_2(\theta)$. The results are shown in Fig. 16. It is seen here that the unsteady prediction agrees reasonably well with the measured ψ_R over most of the circumference with improved agreement over the range $110 < \theta < 220$ deg. In contrast, the quasi-steady prediction, shown by the dashed line, has the correct order of magnitude but fails to predict the details of the measured static pressure variations. (Disagreement between the unsteady prediction and measured data occurs at the screen edges, caused by the sudden changes in the numerically determined derivatives, as explained earlier in connection with Fig. 12.)

Additional Distortion Profiles

Other cases were analyzed in the course of this investigation. Two additional distortion profiles of 180 deg extent were considered which are closely related to the case discussed above. The first of these was for a higher mass flow and lower pressure ratio than the peak pressure condition just examined and is denoted as the midflow condition. The nominal undistorted steady-state operating condition for this case is to the right of the peak value of ψ_R in Fig. 7. The second of these was for a highly loaded condition and is denoted as operation near the surge point. The nominal undistorted steady-state operating condition for this case is to the left of the peak value of ψ_R in Fig. 7.

The measured inlet and exit mid-annulus total pressure profiles, outer diameter static pressure profiles, and inlet yaw angle profile for the midflow condition are shown in Figs. 17, 18, and 19, respectively. This is followed by a comparison between the predicted and measured static pressure coefficient for the same case in Fig. 20. A similar set of figures for operation near the surge point is found in Figs. 21 through 24. In Fig. 20 for the midflow condition we have fair to good agreement between unsteady theory and experiment behind the screen (from $\theta \cong 290$ deg to $\theta \cong 80$ deg) and good agreement upon emergence from the screen (over the range $140 < \theta < 240$ deg). The same statements may be made for operation near the surge point, shown in Fig. 24, where the best agreement is found over the ranges $20 < \theta < 90$ deg and $160 < \theta < 350$ deg. In all of these cases exceptions must be made for regions of excessive scatter occasioned by the numerical differentiation process.

Additional cases were examined for a 135 deg distortion at peak pressure and for a 90 deg distortion near stall. Once again the measured total pressures, static pressures, yaw angles and unsteady pressure predictions, plotted as a function of θ, will be found in Figs. 25 through 28 for the 135 deg distortion and in Figs. 29 through 32 for the 90 deg distortion. In Fig. 28, for the peak pressure condition, both the unsteady prediction and the quasi-steady prediction are in poor agreement over most of the circumference. In Fig. 32, for operation near stall, the agreement between unsteady prediction and measured results is fair to good in the region of blade emergence from the distortion screen with the exception of some sharp discrepancies at the screen edge. This generally good agreement persists over the range $90 < \theta < 230$ deg. Beyond this point the agreement is poor.

A critical examination of all five cases (Figs. 16, 20, 24, 28, 32) shows that the best agreement between unsteady prediction and measured response occurs in the vicinity of blade emergence from the distortion screen, and poor agreement exists in the vicinity of blade entry behind the distortion screen. From the evidence available it appears that the unsteady model is most effective in characterizing the recovery from stall, with good agreement between the prediction and the measured data. Further, it appears that the quiet flow just prior to entry into the distortion, and the disturbed flow during and after distortion entry is more or less poorly modeled by the unsteady analysis. However, before too many generalizations are made it must be realized that the model as it is described herein is relatively primitive and is therefore limited in its capabilities. Work currently in progress has suggested that it may be possible to modify this model to obtain a significant improvement in the agreement between theory and experiment. This work will be the subject of a future report under the current subcontract.

Stage Pressure Rise

The results discussed above have been restricted to the rotor exit plane, or station 2 in Figs. 3 and 6. However, it is desirable to be able to predict (or measure) the stage static pressure rise which requires that the static pressure through the stator also be obtained. (The total pressure is referred to a stationary reference frame and does not change between the rotors.) Calculation of static pressure through the stator is a relatively straightforward procedure if the stator steady-state characteristics are known in advance, or can be accurately predicted.

In the present case the stator characteristics were available from prior measurement, and are shown in Fig. 33 as ψ_S versus stator inlet angle α_2 (see Figs. 3 and 4). The procedure to be followed here is outlined briefly below and is described in detail in Appendixes I and V. The rotor exit velocity triangle is used to compute the circumferential variation in stator inlet angle, α_2. At each θ station Fig. 33 is entered at the appropriate value of α_2 and the stator pressure coefficient, ψ_S, is obtained. Equation (40) in Appendix II is then rewritten for the stator, with p_3 and p_2 replacing p_2 and p_1, respectively, and the equation is solved for p_3 to yield

$$p_3(\theta) = p_2(\theta) + \left(p_2(\theta) + P_{ref}\right) \overline{N}^2 \psi_S(\theta) \tag{11}$$

Radial equilibrium corrections were also calculated here but were found to be negligible because the exit stator flow was nearly axial.

This equation for $p_3(\theta)$ was evaluated for all of the cases considered above and the results are shown in Figs. 34 through 36 for the 180 deg distortion. The p_3 distribution for the peak pressure condition in Fig. 34 may be compared directly with the p_2 distribution shown in Fig. 15 for the same condition. It is seen that the overall agreement between the unsteady prediction and the measured p_3 distribution is not as good as the agreement indicated in Fig. 15 for the p_2 distribution (in the regions away from the screen edges). A detailed examination of this case indicates that the stator inlet angle, α_2, is generally less than 50 deg over the range $10 < \theta < 160$ deg. From Fig. 33 this yields a relatively large value of ψ_s and from Eq. (11) this in turn produces a large term to be added to p_2. Over this same θ range the predicted p_3 overestimates the measured p_3 by a significant margin while the predicted p_2 is, on average, in good agreement with measured values. Beyond $\theta = 160$ deg α_2 grows larger, reaching a peak value of 68 deg in the neighborhood of $200 < \theta < 260$ deg, after which α_2 returns to a value of approximately 55 deg behind the screen. In the region of maximum α_2 the stator pressure rise, ψ_s, becomes very small and the additive term in Eq. (11) also becomes very small. In this same region the predicted p_3 underestimates the measured p_3 by a significant margin while the predicted p_2 is either in ement with or only slightly overestimates the measured values. It can be seen in Eq. (38) in Appendix I that α_2 is directly relatable to V_A through a tangent relationship. Thus α_2 becomes large in the undistorted region, where V_A is large, and it becomes small in the distorted region, where V_A is small. It would appear, then, that the increased discrepancies in the stator exit static pressures may be traced to the initial assumption that the axial velocity is constant through the stage along a constant θ path.

In Fig. 35 the p_3 distribution for the midflow condition is shown. Although there is no comparable p_2 distribution shown in this report for this case, a valid comparison may be made with the ψ_R distribution in Fig. 20. This time the calculation of p_3 at the stator exit appears to produce relatively little deterioration in the agreement between theory and experiment relative to the static pressure at the rotor exit. This case was run at a midflow condition which is removed a bit from the high stall conditions. Consequently the V_A distribution exhibits smaller deviations from the mean and the variations in α_2 are also small. Hence the additive term in Eq. (38) will remain relatively constant.

For completeness, Figs. 36, 37, and 38 show the p_3 distribution for the 180 deg distortion near stall, the 135 deg distortion at peak pressure, and the 90 deg distortion near stall. In general the agreement between the predicted and measured pressures at the stator exit for all five cases is comparable to the agreement between the predicted and measured pressures at the rotor exit, with minor deviations from case to case. However, the results shown here are not felt to be satisfactory in their present form to represent the compressor stage and should not be used for predictions of the distorted flow response of subsequent stages. Note that the remarks made at the end of the last section are pertinent here also, particularly in view of the dependence of p_3 on p_2.

Possible Sources of Error

There are many possible sources of error in this work which could not be examined during the first year's work. Indeed, many of these possible errors could not be anticipated until the work was well along. Some of these are being scrutinized as part of our current investigation and have contributed to the modifications made in the fluid dynamic modeling of this problem. This will be outlined briefly in the next section. The purpose of this section is to list these possible sources of error, to try to speculate on what their impact might be on the final results, and to indicate what means we might employ to eliminate or mitigate the effects of these errors.

Consider first the list of assumptions presented in the first section of this report. At the inception of this work it was felt that these assumptions were necessary to permit a rational beginning to be made in this analysis. This judgment is borne out by the ability of the analysis to yield the agreement that it does. Now that a tractable formulation exists it should be possible to re-examine each assumption and, where possible, to modify the analysis to determine the sensitivity of the results to changes in each assumption.

Within the framework of the experimental data used for comparison herein, Assumption 1 concerning the thermodynamic and inviscid behavior of this low-pressure ratio compressor is felt to be valid. Assumptions 2, 3, and 5 imply, in part, that each blade passage is independent of every other blade passage. This may have contributed to the sharp excursions observed in the predicted pressure rise at the screen edges in view of the influence that each blade exerts on the neighboring flow field and the fact that this influence is neglected here. Assumption 7 restricts the unsteady effects to blade aerodynamic response only. This too may have some bearing on the sudden sharp excursions mentioned above. Assumptions 4, 8, and 9 are interim measures which are necessary because there is no data both below and above stall for either the unsteady lift on a cascaded blade or the unsteady drag on any blade. Assumption 6 appears to be reasonable in view of the high (0.7) hub-tip ratio of the annulus.

In virtually all cases examined in this report a considerable portion of the circumference operated beyond the stall point and within this region a significant portion operated beyond the limit of the available unsteady airfoil data. For example, for the 180 deg distortion at the peak pressure condition it can be seen from Fig. 11 that 75 percent of the circumference was above stall, and over 35 percent of the circumference operated beyond $\sigma = 1.8$ which was the maximum value in the unsteady data tabulation. It can be assumed that the extremely deep penetration of the rotor blades beyond the static stall angle and the lack of unsteady data in that region contributed some error to the final results. At the other extreme it was necessary to extrapolate the steady-state rotor characteristics (see Appendix III) to small values of α_R (large β_1) for some portions of the midflow condition. This too could have contributed to our error. In addition, there may have been insufficient measuring stations in the experiment in the regions of steep gradients in pressure or yaw angle. Within the scope of our present contract the impact of these possible errors can only be guessed at. In each case the only rational corrective procedure is to perform experiments, either into the unsteady behavior of blades and cascades in deep stall, or into the steady behavior of rotors far beyond the normal operating range.

A final item for consideration here is not, strictly speaking, an error, but instead represents a deficiency in the theory which must be overcome in the future. The results shown earlier use measured upstream flow properties obtained at the inlet plane during an inlet distortion experiment. These upstream conditions are strongly dependent on the presence of the blade row, as shown in Fig. 39. Here we have plotted the measured stall angle parameter, σ, versus circumferential position, θ, for the peak pressure condition with a 180 deg distortion. The dashed line in Fig. 39 represents the angle of attack distribution that would be measured immediately behind the distortion screen far upstream of the blade row, and the solid line is the actual angle of attack distribution at the blade row inlet (repeated from Fig. 11). It is seen that the blade row has an important effect on the inlet flow, and produces a further distortion of large magnitude on the previously distorted flow. At present it is not possible to predict the change in the distortion pattern as it comes under the influence of the blade row, and it is necessary to measure the upstream conditions during an actual distortion experiment. However, the ultimate purpose of this program is to provide the designer with the necessary tools to predict compressor stability due to inlet distortion without recourse to test. Hence the designer should have at his disposal an *a priori* method to specify a distortion pattern, predict its behavior as it approaches the blade row, and predict blade row response to this distortion. Furthermore, this should be a fully coupled system which accounts for the mutual interactions of blade row response to the distortion and blade row influence on the distortion. Our current efforts are being directed toward exploring this objective and are described briefly below.

CONCLUSIONS AND BRIEF REVIEW OF FUTURE WORK

During the first year's work reported on herein it has been shown that an unsteady model based on unsteady aerodynamic data from an isolated airfoil could lead to a reasonable representation of the circumferential pressure distribution of a rotor in a distorted flow. It is seen that in general the unsteady prediction is in better agreement with experiment than the quasi-steady prediction, but that there are regions where both theories are in significant disagreement with the data. Although this model has yielded encouraging results, it is recognized that it depends strongly on a number of intermediate transformations and assumptions. Furthermore, we have concluded that it is difficult to improve or refine the results using physically rational techniques within the framework of the existing theory. Hence, we have undertaken to reformulate the problem in more fundamental terms involving the direct use of compressor and blade row parameters, including loss and turning characteristics. This procedure is described briefly below.

A simple unsteady model based on cascade loss and turning correlations has been derived to predict the pressure rise across a rotor operating in a distorted inflow. This nonlinear model is obtained from a consideration of the equations governing the passage of a two-dimensional incompressible flow between two blades of a compressor, and includes provision for unsteadiness by means of time variations in both passage kinetic energy and blade row loss. To date the application of this revised theory has shown significant improvement over the results obtained by our aerodynamic force procedure described above. In addition to its simplicity, it has the further advantage of being directly related to the blade row through the blade loss and turning characteristics, rather than the indirect scaling relationships of the previous aerodynamic model. Accordingly, this model is being adopted for all subsequent work being done on this contract.

An analysis is also being formulated to introduce the effects of the presence of the blade row on the upstream disturbance. As ultimately envisioned this represents a nonlinear, time-dependent analysis of the duct flow coupled with the nonlinear, time-dependent blade passage analysis which will permit us to solve our problem for large disturbances which can be steady or time dependent. This is a formidable problem and it is felt that its implementation can be justified only by demonstrating the tractability of its constituent parts, in simplified form. The first part consisting of the nonlinear blade passage loss analysis has already been implemented and appears to give excellent results. A simplified version of the corresponding nonlinear flow field analysis was recently attempted and is described below. A numerical procedure was devised to solve the time-dependent vorticity and stream function equations, subject to a downstream boundary condition involving the pressure change across a blade row. The problem was simplified by assuming the blades were stationary with respect to the upstream distortion (i.e., the cascade problem) and by eliminating time dependency in the blade passage analysis. Results obtained to date are very encouraging and appear to have physically realistic behavior.

Although the problem described in this section is simple in form (i.e., a solution of the lightly loaded cascade interaction at relatively low distortion levels), we feel it contains many of the key essential elements of the complete problem which should be solved in future work. First, it demonstrates the mutual interaction effects of the upstream distortion vorticity and the bound vorticity of the blade row. Second, although the parameters chosen for study represented modest perturbations, they were not "small" perturbations in the linear sense, and the solution represented a nonlinear process. Third, from an operational point of view, the numerical solution was stable, and we feel that any extension of this solution to the more complicated case of a moving blade row can be maintained stable. Finally, it was a time- and space-dependent solution, although it was used here to solve a quasi-steady problem. Hence, in the future it will be possible to extend this procedure further to fully time-dependent systems. This time-dependent nonlinear model will permit us to specify a distortion pattern at the inlet of a compressor, predict its behavior as it approaches the compressor stage, and predict compressor stage response to this distortion.

ACKNOWLEDGMENT

The author wishes to acknowledge the assistance of the Pratt & Whitney Division of United Aircraft Corporation in making the experimental compressor data available for this study, and in particular the work of Mr. Jay Jeffes of that Division who provided invaluable help in assembling, interpreting, and clarifying these data. Near the end of the work covered in the present report the author was joined by Dr. John Adamczyk who assisted in completing the analysis and who has become actively involved in deriving an improved analytical model which is currently under development.

REFERENCES

1. Langston, C. E.: Distortion Tolerance - By Design Instead of by Accident. ASME Paper No. 69-GT-115, March 1969.
2. Reid, C.: The Response of Axial Flow Compressors to Intake Flow Distortion. ASME Paper No. 69-GT-29, March 1969.
3. Carta, F. O.: Unsteady Normal Force on an Airfoil in a Periodically Stalled Inlet Flow. AIAA Journal of Aircraft, Vol. 4, No. 5, September-October 1967, pp. 416-421.
4. Cohen, H. and G. F. C. Rogers: Gas Turbine Theory. Longmans, London, 1950.
5. Sorensen, H. A.: Gas Turbines. The Ronald Press Company, New York, 1951.
6. Horlock, J. H.: Axial Flow Compressors. Butterworths Scientific Publications, London, 1958.
7. Johnson, I. A. and R. O. Bullock, editors: Aerodynamic Design of Axial Flow Compressors. NASA SP-36, 1965.
8. Arcidiacono, P. J., F. O. Carta, L. M. Casellini, and H. L. Elman: Investigation of Helicopter Control Loads Induced by Stall Flutter. USAAVLABS Technical Report 70-2, March 1970.
9. Ham, N. D.: Aerodynamic Loading on a Two-Dimensional Airfoil During Dynamic Stall. AIAA Journal, Vol. 6, No. 10, October 1968, pp. 1927-1934.

REFERENCES (Continued)

10. Isogai, K.: An Experimental Study on the Unsteady Behavior of a Short Bubble on an Airfoil During Dynamic Stall With Special Reference to the Mechanism of the Stall Overshoot Effects. MIT Aeroelastics and Structures Research Lab. Report ASRL TR 130-2, June 1970.

11. Carta, F. O.: Effect of Unsteady Pressure Gradient Reduction on Dynamic Stall Delay. AIAA Journal of Aircraft, Vol. 8, No. 10, October 1971, pp. 839-841.

12. Bellinger, E. D.: Analytical Investigation of the Effects of Blade Flexibility, Unsteady Aerodynamics, and Variable Inflow on Helicopter Rotor Stall Characteristics. NASA CR-1769, September 1971.

13. Kauffman, W. M. and M. Shinbrot: A Method for Differentiation of Experimental Data. Journal of the Aeronautical Sciences, Vol. 20, No. 6, June 1953, pp. 428-430.

LIST OF SYMBOLS

A	Annular area, ft^2, Eq. (42), or angular velocity parameter, Eq. (64)
b	Airfoil semichord, ft, Eq. (93)
B	Angular acceleration parameter, Eq. (65)
c	Airfoil chord, ft, Eq. (10)
C_D	Drag coefficient, Eq. (55)
C_{F_A}	Axial force coefficient, Eq. (10)
C_{F_Ω}	Tangential force coefficient, Eq. (10)
C_L	Lift coefficient, Eq. (55)
C_L^*	Normalized lift coefficient, = 1 at stall, Eq. (59)
D	Drag, lb, Eq. (55)
D_1, D_2	Drag differences, Eqs. (70), (71)
F_A	Axial force, lb, Eq. (7)
F_Ω	Tangential force, lb, Eq. (7)
g	Gravitational acceleration, = 32.16 ft/sec^2, Eq. (41)
H	Momentum, lb-sec, Eq. (17)
$\bar{K}$	Fully stalled lift multiplier, Eq. (76)
ℓ	Blade span, ft, Eq. (12)
L	Lift, lb, Eq. (55)
L_1, L_2	Lift differences, Eqs. (72), (73)
m	Fluid mass, lb-sec^2/ft, Eq. (12)

LIST OF SYMBOLS (Continued)

n	Number of blades or blade passages, Eq. (42)
N	Wheel speed, rpm, Eq. (45)
$\overline{N}$	Corrected wheel speed ratio, Eq. (45)
p	Static pressure, lb/ft^2 or in. H_2O, Eq. (1)
p_o	Total pressure, lb/ft^2 or in. H_2O, Eq. (1)
r	Radius, ft, Eq. (123)
t	Time, sec, Eq. (12)
T_R	Temperature ratio, Eq. (43)
U	Wheel speed, ft/sec, Eq. (4)
V	Relative velocity, ft/sec, Eq. (84)
V_A	Axial velocity, ft/sec, Eq. (3)
V_o	Absolute velocity, ft/sec, Eq. (2)
V_Ω	Tangential swirl velocity, ft/sec, Eq. (4)
W	Annular weight flow, lb/sec, Eq. (41)
α	Absolute velocity angle, Eq. (37), or angle of attack, Eq. (6), deg or rad
α_{CH}	Chord angle, deg or rad, Eq. (6)
α_y	Yaw angle, deg or rad, Eq. (3)
β	Relative velocity angle, deg or rad, Eq. (5)
δ	Total pressure ratio, Eq. (44)

LIST OF SYMBOLS (Continued)

δ_D	Drag increment, Eq. (69)
δ_L	Lift increment, Eq. (63)
ϵ	Tolerance limit, Eq. (101)
θ	Circumferential position, deg or rad, Eq. (1)
ρ	Air density, $lb\text{-}sec^2/ft^4$, Eq. (1)
σ	Stall angle ratio, Eq. (57)
τ	Tangential blade gap, ft, Eq. (12)
ϕ	Flow coefficient, $(lb/sec)/ft^2$, Eq. (39)
ψ	Static pressure coefficient, Eq. (35)
ω	Angular velocity, rad/sec, Eq. (123)
Ω	Rotor angular velocity, rad/sec, Eq. (67)

Subscripts

1	Station 1, at rotor inlet plane
2	Station 2, at rotor exit plane
3	Station 3, at stator exit plane
A	Axial or airfoil
Des	Design condition
FS	Full stall
H	Momentum
NS	No stall

LIST OF SYMBOLS (Continued)

O	Minimum loss or minimum drag
P	Potential flow
ref	Atmospheric reference
R	Rotor blade
S	Stall or stator
SS	Steady state
U	Unsteady
Ω	Tangential

Superscripts

$(\dot{\ })$	First time derivative, d/dt
$(\ddot{\ })$	Second time derivative, d^2/dt^2
$(\ )'$	First circumferential derivative, $d/d\theta$
$(\ )''$	Second circumferential derivative, $d^2/d\theta^2$

APPENDIX I

DERIVATION OF THE QUASI-STEADY FLUID DYNAMICS THROUGH A BLADE ROW

The flow through a blade row has been the subject of analysis in a number of basic textbooks (e.g., Refs. 4, 5, 6). The derivation contained herein is simply for the convenience of the reader and will serve to establish a consistent set of notation for use in this report.

Consider the compressor blade row shown in Fig. 3. In the work that follows, each equation will be derived for a quasi-steady fluid flow through the stage, and will then be simplified according to the assumptions governing the present analysis.

First consider the continuity of the flow through the rotor. The incremental mass entering any blade passage of area $\tau\ell_1$ per unit time is

$$\frac{\Delta m_1}{\Delta t} = \rho_1 \tau \ell_1 \frac{\Delta x_1}{\Delta t} = \rho_1 \tau \ell_1 V_{A_1} \tag{12}$$

and this must be equal to the mass leaving the passage at the exit plane,

$$\frac{\Delta m_2}{\Delta t} = \rho_2 \tau \ell_2 \frac{\Delta x_2}{\Delta t} = \rho_2 \tau \ell_2 V_{A_2} \tag{13}$$

where x is measured in the axial direction and where V_A is the axial velocity. If the passage height is constant, then $\ell_1 = \ell_2$, and upon setting these expressions equal we have

$$\rho_1 V_{A_1} = \rho_2 V_{A_2} \tag{14}$$

If the further assumption of incompressible flow with negligible temperature rise through the blade row is made, then Eq. (14) reduces simply to

$$\rho_1 = \rho_2 = \rho \tag{15}$$

$$V_{A_1} = V_{A_2} = V_A \tag{16}$$

Note that although V_A is constant axially it can vary circumferentially.

Now consider the axial force on the blade row, which is the sum of the force due to the change in axial momentum across the blade row and the axial pressure force on the blade row. First, the axial momentum into the blade row is

$$H_{A_1} = \Delta m_1 V_{A_1} = \rho_1 \tau \ell_1 \Delta x_1 V_{A_1} \tag{17}$$

and out of the blade row is

$$H_{A_2} = \Delta m_2 V_{A_2} = \rho_2 \tau \ell_2 \Delta x_2 V_{A_2} \tag{18}$$

so the axial force due to momentum change is

$$F_{A_H} = \frac{\Delta H_A}{\Delta t} = \rho_1 \tau \ell_1 \frac{\Delta x_1}{\Delta t} V_{A_1} - \rho_2 \tau \ell_2 \frac{\Delta x_2}{\Delta t} V_{A_2} = \tau \ell \left(\rho_1 V_{A_1}^2 - \rho_2 V_{A_2}^2 \right) \qquad (19)$$

for constant passage height. There will also be an axial force due to the axial pressure gradient acting across each blade passage, or, for constant passage height,

$$F_{A_p} = \tau \ell (p_2 - p_1) \qquad (20)$$

The total axial force is obtained from the sum of Eqs. (19) and (20),

$$F_A = \tau \ell (p_2 - p_1 + \rho_1 V_{A_1}^2 - \rho_2 V_{A_2}^2) \qquad (21)$$

With the simplifications of Eqs. (15) and (16) this reduces to

$$F_A = \tau \ell (p_2 - p_1) \qquad (22)$$

Finally, the tangential force on the blade row will be derived. The tangential momentum into the blade row is given by the product of the incremental mass and the inlet swirl velocity in the relative frame of reference,

$$H_{\Omega_1} = \Delta m_1 V_{\Omega_1} = \rho_1 \tau \ell_1 \Delta x_1 V_{\Omega_1} \qquad (23)$$

and the tangential momentum out of the blade row is

$$H_{\Omega_2} = \Delta m_2 V_{\Omega_2} = \rho_2 \tau \ell_2 \Delta x_2 V_{\Omega_2} \qquad (24)$$

Hence the tangential force due to momentum is

$$F_{\Omega} = \frac{\Delta H_{\Omega}}{\Delta t} = \rho_1 \tau \ell_1 \frac{\Delta x_1}{\Delta t} V_{\Omega_1} - \rho_2 \tau \ell_2 \frac{\Delta x_2}{\Delta t} V_{\Omega_2} = \tau \ell \left(\rho_1 V_{A_1} V_{\Omega_1} - \rho_2 V_{A_2} V_{\Omega_2} \right) \qquad (25)$$

for constant passage height.

In the simplified analysis of this study the tangential pressure gradient will be zero, as explained below. If a control volume is chosen which contains exactly one blade and one blade passage, then in this simple, quasi-steady fluid dynamic model the pressure distribution on one streamwise face of the volume will be identical to the pressure distribution on the other streamwise face. Hence, the tangential pressure gradient is zero and there is no pressure force in the tangential direction. Thus Eq. (25) represents the only tangential force acting on the system. Again using the simplifications of Eqs. (15) and (16), Eq. (25) reduces to

$$F_{\Omega} = \tau \ell \rho V_A (V_{\Omega_1} - V_{\Omega_2}) \qquad (26)$$

An immediate objective of this analysis is to provide the necessary equations to predict the exit static and total pressure distributions. The static pressure is immediately obtained from Eq. (22) as

$$p_2 = p_1 + \frac{F_A}{\tau \ell} \tag{27}$$

To obtain the total pressure, rewrite the steady form of Bernoulli's equation (Eq. (1)) at the rotor exit as

$$P_{02} = p_2 + \frac{1}{2} \rho_2 V_{02}^2 \tag{28}$$

In this equation p_2 is already known from Eq. (27), and from Eq. (15) ρ_2 will be replaced by the constant density ρ. This leaves V_{02} as the unknown quantity. From the exit velocity triangle in Fig. 4,

$$V_{02}^2 = V_{A_2}^2 + (U - V_{\Omega_2})^2 \tag{29}$$

and with $V_{A2} = V_A$ (from Eq. (16)), and V_{Ω_2} given by Eq. (26) as

$$V_{\Omega_2} = V_{\Omega_1} - \frac{F_\Omega}{\tau \ell \rho V_A} \tag{30}$$

Eq. (28) becomes

$$P_{02} = p_2 + \frac{1}{2} \rho \left[V_A^2 + \left(U - V_{\Omega_1} + \frac{F_\Omega}{\tau \ell \rho V_A} \right)^2 \right] \tag{31}$$

It will be convenient to deal with the various aerodynamic forces in coefficient form. Hence we define these coefficients in terms of the inlet relative dynamic pressure as

$$F_A = \frac{1}{2}\rho V_1^2 c \ell C_{F_A}$$

$$F_\Omega = \frac{1}{2}\rho V_1^2 c \ell C_{F_\Omega} \tag{32}$$

With these substitutions Eqs. (27) and (31) become

$$p_2 = p_1 + \frac{\rho V_1^2 C_{F_A}}{2\,\tau/c} \tag{33}$$

$$P_{02} = p_2 + \frac{1}{2}\rho\left[V_A^2 + \left(U - V_{\Omega_1} + \frac{V_1^2 C_{F_\Omega}}{2(\tau/c)V_A}\right)^2\right] \tag{34}$$

To complete the analysis of the flow through the stage, we now take the rotor exit variables obtained above and regard them as inlet variables for the stator. The analysis is simpler here because the nonmoving stator operates in a fixed reference frame. Hence the intermediate unsteady blade force analysis is not needed, and a simple set of expressions relating stator pressure rise to inlet flow is all that is necessary.

As shown in Fig. 33, the steady-state stator characteristics are given herein as the static pressure coefficient for the stator,

$$\psi_S = \frac{p_3 - p_2}{(p_2 + P_{ref})\overline{N}^2} \tag{35}$$

versus the stator inlet angle α_2. Hence, to solve for the stage exit static pressure,

$$p_3 = p_2 + (p_2 + P_{ref})\overline{N}^2 \psi_S \tag{36}$$

it is only necessary to know the rotor exit static pressure, p_2, and the stator inlet angle, α_2. The latter may be used to extract ψ_s data from Fig. 33 whereupon Eq. (36) is completely determined.

From the bottom portion of Fig. 4, α_2 is seen to be

$$\alpha_2 = \tan^{-1}\left(\frac{V_A}{U - V_{\Omega_2}}\right) \tag{37}$$

where V_A is used in place of V_{A_2} in accordance with Eq. (16). When Eq. (30) is substituted for V_{Ω_2} and Eq. (32) is used, the formula for α_2 becomes

$$\alpha_2 = \tan^{-1}\left(\frac{V_A}{U - V_{\Omega_1} + \frac{V_1^2 C_{F_\Omega}}{2(\tau/c)V_A}}\right) \tag{38}$$

All of the parameters in Eq. (38) have been previously defined and are either rotor inlet quantities or easily calculated rotor blade quantities.

APPENDIX II

CONVERSION OF STEADY-STATE COMPRESSOR CHARACTERISTICS TO ROTOR BLADE LIFT AND DRAG

To relate the steady-state lift and drag of a rotor blade to the compressor performance characteristics it is convenient to begin with the definitions of the flow coefficient,

$$\phi = \frac{W\sqrt{T_R}}{\delta A \bar{N}} \tag{39}$$

and the rotor static pressure coefficient,

$$\psi_R = \frac{p_2 - p_1}{(p_1 + P_{ref})\bar{N}^2} \tag{40}$$

Here the annular weight flow, W, is given by

$$W = n\tau \ell \rho g V_A \tag{41}$$

and the annular area, A, by

$$A = n\tau \ell \tag{42}$$

The standard definitions of temperature ratio and total pressure ratio (Ref. 7) are used here,

$$T_R = \frac{T_{TOT_1}}{518.7} \qquad (43)$$

$$\delta = \frac{P_{01} + P_{ref}}{2116} \qquad (44)$$

where T_{TOT_1} is inlet total temperature and 518.7 is standard temperature, both in °R, and where P_{01} is relative inlet total pressure, P_{ref} is local atmospheric total pressure, and 2116 is standard atmospheric pressure, all in lb/ft^2. The corrected wheel speed ratio, $\overline{N}$ is given by

$$\overline{N} = \frac{N/\sqrt{T_R}}{(N/\sqrt{T_R})_{DES}} \qquad (45)$$

where N is actual wheel speed and the subscript Des denotes the design condition. In the static pressure coefficient equation p_2-p_1 is the static pressure rise through the rotor, p_1 is the relative inlet static pressure, and P_{ref} and $\overline{N}$ have already been defined above. Note that in these equations the temperature ratio is denoted by T_R rather than by θ to avoid confusion with the circumferential position around the compressor.

In the experimental work performed at UARL for the Pratt & Whitney Division of United Aircraft Corporation, which was described briefly above, the inlet total temperature ratio was approximately one. Hence, upon substituting Eqs. (41), (42), (44), and the numerical values $T_R \cong 1$, $g = 32.16$,

Eq. (39) becomes

$$\phi = \frac{68{,}051\,\rho V_A}{(P_{01} + P_{ref})\,\overline{N}} \tag{46}$$

which has the units of weight flow per unit area, (lb/sec)/ft^2. The measured compressor characteristics for the first rotor (and first stator) of the UARL three-stage test compressor is shown in Fig. 7. These and other measured steady-state quantities for the first rotor are listed in Table I.

To compute the steady-state forces acting on the rotor blades, solve Eq. (40) for p_2-p_1 and substitute this into Eq. (8) to obtain

$$C_{F_A} = \frac{(p_1 + P_{ref})\,\overline{N}^2 \psi_R\,\tau/c}{\frac{1}{2}\rho V_1^2} \tag{47}$$

which is the axial force coefficient. For a given geometry we know τ/c, for an atmospheric inlet we know ρ, and from Table I we know $\overline{N}$ and ψ_R. The remaining quantities are easily obtained in terms of the given characteristics. From Eq. (1), for the absolute frame of reference, write

$$\frac{p_1 + P_{ref}}{\frac{1}{2}\rho V_1^2} = \frac{P_{01} + P_{ref}}{\frac{1}{2}\rho V_1^2} - \left(\frac{V_{01}}{V_1}\right)^2 \tag{48}$$

and from the inlet velocity triangle of Fig. 4,

$$\sin\beta_1 = \frac{V_A}{V_1} \tag{49}$$

so Eq. (48) becomes

$$\frac{p_1 + P_{ref}}{\frac{1}{2}\rho V_1^2} = \left[\frac{P_{01} + P_{ref}}{\frac{1}{2}\rho V_A^2} - \left(\frac{V_{01}}{V_A}\right)^2\right] \sin^2\beta_1 \tag{50}$$

and Eq. (47) can be rewritten in terms of known or given steady-state quantities,

$$C_{F_A} = \frac{\tau}{c}\left[\frac{P_{01} + P_{ref}}{\frac{1}{2}\rho V_A^2} - \left(\frac{V_{01}}{V_A}\right)^2\right] \overline{N}^2 \psi_R \sin^2\beta_1 \tag{51}$$

The steady-state tangential force coefficient is most easily obtained from a combination of Eqs. (26) and (32),

$$C_{F_\Omega} = 2\,\frac{\tau}{c}\,\frac{V_A}{V_1}\left(\frac{V_{\Omega 1}}{V_1} - \frac{V_{\Omega 2}}{V_1}\right) \tag{52}$$

From the inlet and exit velocity triangles of Fig. 4,

$$\begin{aligned} \cos\alpha_1 &= \frac{U - V_{\Omega 1}}{V_{01}} \\ \cos\alpha_2 &= \frac{U - V_{\Omega 2}}{V_{02}} \end{aligned} \tag{53}$$

and when Eqs. (49) and (53) are substituted into Eq. (52) the result is

$$C_{F_\Omega} = \frac{2\tau/c}{V_A}\left(V_{02}\cos\alpha_2 - V_{01}\cos\alpha_1\right)\sin^2\beta_1 \tag{54}$$

from which the tangential force coefficient can be calculated in terms of known or given steady-state quantities.

Finally, if we define the lift and drag coefficients in terms of inlet quantities,

$$C_L = \frac{L}{\frac{1}{2}\rho V_1^2 c \ell}$$

$$C_D = \frac{D}{\frac{1}{2}\rho V_1^2 c \ell} \tag{55}$$

then use of Eqs. (10) and the inverted form of Eqs. (7) yield

$$C_L = C_{F_\Omega} \sin \beta_1 + C_{F_A} \cos \beta_1$$

$$C_D = C_{F_\Omega} \cos \beta_1 - C_{F_A} \sin \beta_1 \tag{56}$$

Use of the tabulated steady-state rotor parameters in Eqs. (51), (54), and (56) yields the rotor lift and drag variation with inlet angle, β_1. These are plotted in Fig. 40 versus the more convenient rotor blade angle of attack, α_R, obtained from Eq. (6). Also in this figure a subscript R has been introduced into the C_L and C_D notation to denote rotor blade quantities. Because of the limited range of the data available the α_R range is restricted to values greater than 8 deg, and it was necessary to extrapolate the lift linearly towards $\alpha_R = 0$. Also, the calculated drag appears to go to zero near 8 deg, and it is impossible to extrapolate this characteristic to any lower angle of attack. It will be shown later that this behavior can be partially compensated for by our scaling procedure.

APPENDIX III

UNSTEADY LIFT SCALING PROCEDURES

Consider first the schematic plot in Fig. 41, with typical rotor blade lift and drag shown at the top and airfoil lift at the bottom. In contrast to the computed rotor blade drag behavior in Fig. 40, the schematic drag has been drawn to have a minimum value at some small angle of attack, α_{Ro}. In our application, this will be made to correspond to the conventional minimum loss point for cascade or rotor blades. The stall point, at α_{Rs}, is defined as the point at which the lift curve departs from linearity. The angle of attack range between α_{Ro} and α_{Rs} is the linear lift range. Based on this linear range we can define a stall angle ratio,

$$\sigma_R = \frac{\alpha_R - \alpha_{Ro}}{\alpha_{Rs} - \alpha_{Ro}} \tag{57}$$

in which α_R is the actual rotor angle of attack. If the rotor blade is stalled then $\alpha_R > \alpha_{Rs}$ and $\sigma > 1$, and if the rotor blade is unstalled then $\alpha_R < \alpha_{Rs}$ and $\sigma < 1$.

The airfoil data used in the present study had a symmetric NACA 0012 section, hence the minimum drag occurs at zero angle of attack and the stall angle ratio for the airfoil is simply given by

$$\sigma_A = \frac{\alpha_A}{\alpha_{AS}} \tag{58}$$

Over the linear range of each curve (i.e., for $\sigma \leq 1$) the angle of attack at any point can be replaced by the corresponding lift coefficient, so we can write

$$\sigma_R = \frac{C_{L_R} - C_{L_{RO}}}{C_{L_{RS}} - C_{L_{RO}}} = C_{L_R}^{*} \qquad (\sigma_R \leq 1) \tag{59}$$

$$\sigma_A = \frac{C_{L_A}}{C_{L_{AS}}} = C_{L_A}^{*} \qquad (\sigma_A \leq 1) \tag{60}$$

where $C_{L_R}^{*}$ and $C_{L_A}^{*}$ are the rotor and airfoil lift ratios, respectively, which equal unity at the stall point. To cause the two lift curves in Fig. 41 to match over the linear range, set

$$\sigma_R = \sigma_A = \sigma \tag{61}$$

or

$$C_{L_R}^{*} = \frac{C_{L_R} - C_{L_{RO}}}{C_{L_{RS}} - C_{L_{RO}}} = \frac{C_{L_A}}{C_{L_{AS}}} = C_{L_A}^{*} \tag{62}$$

A comparison between $C_{L_R}^{*}$ and $C_{L_A}^{*}$ is shown in the upper half of Fig. 42 where both normalized lift curves are plotted versus σ. From Fig. 40 the numerical values for the rotor blade are: $\alpha_{Rs} = 12$ deg, $C_{L_{Rs}} = 0.432$; $\alpha_{Ro} = 3.29$ deg (from the minimum loss condition for this blade row), $C_{L_{Ro}} = 0.265$. The comparable data for the NACA 0012 isolated airfoil used here (Ref. 3) are $\alpha_{AS} = 10$ deg, $C_{L_{AS}} = 1.02$. The definition of the functions $C^*_{L_R}$ and $C^*_{L_A}$ in Eq. (62) forces agreement up to $\sigma = 1$, and it is seen in Fig. 42 that the two functions continue to agree up to $\sigma \cong 1.3$. Beyond this point the two curves diverge. To obtain congruence over the entire range of σ it is necessary to introduce a correction increment δ_L in the form

$$C_{L_R}^* = C_{L_A}^* + \delta_L \tag{63}$$

where δ_L is defined by Eq. (63) as the difference between $C^*_{L_R}$ and $C^*_{L_A}$, and is shown in the lower half of Fig. 42.

Consider next the procedure for determining the unsteady lift. Use has been made here of the extensive tabulation of unsteady lift obtained at the United Aircraft Research Laboratories (UARL) on an NACA 0012 airfoil section. These data are fully documented in Refs. 3 and 8, and the unsteady lift coefficient is tabulated in Ref. 8 as a function of the angular position, α_A, the angular velocity parameter,

$$A = \frac{b\dot{\alpha}_A}{V_1} \tag{64}$$

and the angular acceleration parameter,

$$B = \frac{b^2\ddot{\alpha}_A}{V_1^2} \tag{65}$$

The airfoil angle of attack, α_A, can be written in terms of the rotor blade angle of attack, α_R, by using Eqs. (57), (58), and (61),

$$\alpha_A(\theta) = \alpha_{AS} \ \sigma(\theta) = \frac{\alpha_{AS}\,(\alpha_R(\theta) - \alpha_{RO})}{\alpha_{RS} - \alpha_{RO}} \tag{66}$$

This is a function of circumferential position, θ, so the time derivatives become

$$\dot{\alpha}_A = \frac{d\alpha_A}{d\theta} \cdot \frac{d\theta}{dt} = \Omega\, \alpha_A'(\theta) \tag{67}$$

$$\ddot{\alpha}_A = \frac{d^2\alpha_A}{d\theta^2} \cdot \left(\frac{d\theta}{dt}\right)^2 = \Omega^2 \alpha_A''(\theta) \tag{68}$$

where $\Omega = d\theta/dt$ is the rotor angular velocity and the prime denotes differentiation with respect to θ. Once these derivatives are known the unsteady airfoil lift can be obtained from the tabulation of Ref. 8. A key assumption made at this point is that the unsteady rotor blade lift is incrementally related to steady rotor blade lift in the same manner that the unsteady and steady airfoil lift are related. In other words, we assume that Eq. (63) is also valid for unsteady lift response.

It is convenient at this point to provide a brief synopsis of the steps followed in calculating unsteady lift. A similar synopsis will be given in the next Appendix for unsteady drag, and a detailed summary of the computation procedure will be presented in Appendix V. First compute the circumferential inlet angle, $\beta_1(\theta)$, from Eq. (5), using the various inlet quantities and Bernoulli's equation (1). Next compute rotor blade angle of attack, α_R, from Eq. (6), and the stall angle ratio, σ, from Eq. (57). The airfoil angle of attack is given by Eq. (66), and after computing the derivatives in Eqs. (67) and (68), determine A and B from Eqs. (64) and (65). Next enter the tabulation in Ref. 8 and interpolate a value of C_{L_A} which is then normalized to $C^*_{L_A}$ by the right-hand portion of Eq. (60). Apply the incremental correction of Eq. (63) to obtain $C^*_{L_R}$ and then solve the right-hand portion of Eq. (59) for unsteady rotor lift coefficient, C_{L_R}. Insert this value together with the unsteady rotor blade drag coefficient (see Appendix IV) into Eq. (56) and invert to obtain the axial and tangential force coefficients, C_{F_A} and C_{F_Ω}. Finally, substitute these force coefficients into Eqs. (8) and (9) to compute the exit static and total pressures at each circumferential station, θ .

APPENDIX IV

UNSTEADY DRAG HYPOTHESIS AND SCALING PROCEDURES

The initial procedures leading to the determination of the steady-state rotor drag shown in Fig. 40 have already been discussed above. In this Appendix we will describe the subsequent steps necessary to relate steady-state airfoil and rotor blade drag coefficients, and further, to obtain unsteady drag from steady-state drag. The steady-state drag transformation procedure is similar to that used in transforming steady-state lift. However, in view of the complete lack of unsteady drag information it was necessary to construct a hypothetical unsteady drag model. These procedures are described below.

First consider the steady-state drag. No drag data, either steady or unsteady, were obtained during the test described in Ref. 8. Hence, steady data (unpublished) from other tests conducted at UARL on an NACA 0012 airfoil will be used. This has been reduced to a dependency on σ and is presented in the upper half of Fig. 43. Also shown for comparison is the steady rotor blade drag from Fig. 40, also plotted as a function of σ. As before, the two curves will be made congruent by computing an incremental correction, δ_D, defined by the equation

$$C_{D_R} = C_{D_A} + \delta_D \tag{69}$$

where δ_D is plotted in the lower half of Fig. 43.

A conceptual model will now be constructed to permit the determination of the unsteady drag. This model is based on two well-known facts; namely, that the drag rises rapidly when the flow over the airfoil separates, and that separation is delayed on an airfoil executing an unsteady motion (Refs. 9, 10, 11). The technique to be employed here was conceived at UARL and is described in Ref. 12. The basis of this technique is the departure of the instantaneous lift from some reference value of the lift.

For simplicity, consider first the steady-state behavior, as shown in the sketch in Fig. 44. In the lower half of this figure the solid line represents the steady drag coefficient, C_{DSS}. The broken line labeled C_{DNS} is the hypothetical extension of the "no-stall" drag; i.e., we presume that if no stall occurred the drag would continue at a low level, as extrapolated here. The broken line labeled $C_{nss} \sin\alpha$ represents the variation of the streamwise component of the normal force. At the point where $C_{nss} \sin\alpha$ first equals the steady-state drag we assume that the airfoil is fully stalled and we label the angle of attack accordingly as α_{FS}. In the upper half of this figure the solid line represents the steady-state lift variation with α, and the broken line labeled C_{L_P} represents the straight line extrapolation of the potential flow lift. Suppose we have complete lift information (i.e., the entire upper half of the figure) but our knowledge of the drag is limited to the no stall drag curve, C_{DNS}, the value of the drag at a fully stalled condition, C_{DFS}, and the angle of attack at full stall, α_{FS}. Furthermore, suppose we wish to compute the drag variation at any arbitrary angle of attack, α . The following hypothesis is proposed. Let D_1 be the unknown departure of the drag from the no stall drag, and let D_2 be the known difference between the drag at full stall and the no stall drag at α_{FS}, or

$$D_1 = C_{D_{SS}}(\alpha) - C_{D_{NS}}(\alpha) \tag{70}$$

$$D_2 = C_{D_{FS}} - C_{D_{NS}}(\alpha_{FS}) \tag{71}$$

Also let L_1 be the known departure of the lift from the potential lift at α , and let L_2 be the known departure of the lift from the potential lift at a fully stalled condition, or

$$L_1 = C_{L_P}(\alpha) - C_{L_{SS}}(\alpha) \tag{72}$$

$$L_2 = C_{L_P}(\alpha_{FS}) - C_{L_{FS}} \tag{73}$$

Our hypothesis is that the ratio of the two drag departures from no stall is equal to the ratio of the two lift departures from potential flow, or

$$\frac{D_1}{D_2} = \frac{L_1}{L_2} \tag{74}$$

When we substitute Eq. (70) for D_1 and solve for the unknown steady-state drag coefficient we obtain

$$C_{D_{SS}}(\alpha) = C_{D_{NS}}(\alpha) + \frac{L_1(\alpha)}{L_2} D_2 \tag{75}$$

This hypothesis was tested in Ref. 12 and the results, reproduced from Fig. 8 of this reference, are shown in Fig. 45. It is seen that the agreement between predicted and actual C_D is excellent.

This ability of the hypothetical drag model to predict steady-state drag was the basis for the unsteady drag hypothesis which follows. Here we assume that we have complete steady-state information for both lift and drag, and further, that we are given an unsteady lift hysteresis loop. For illustrative purposes we shall use an unsteady lift hysteresis loop adapted from Ref. 3. This is shown as the solid curve denoted by C_L in the upper half of Fig. 46. The arrows indicate the direction of increasing time. The dashed line is the steady lift, $C_{L_{SS}}$, the dash-dot line is the potential flow lift curve extension, C_{L_P}, and the dotted line represents a lower limit to the lift characteristic of a fully stalled condition, $C_{L_{FS}}$. This lower limit should be the lower envelope (or the greatest lower bound) of all possible lift hysteresis loops. Although it cannot be determined precisely, experience has shown that this bound usually occurs at approximately 50 percent of the steady lift at any angle of attack. Hence we will define

$$C_{L_{FS}} = \overline{K}\, C_{L_{SS}} \tag{76}$$

where $\overline{K} = 0.5$ in the present report. The corresponding drag curves are found in the lower half of the figure. The dashed curve is the steady drag, $C_{D_{SS}}$, the dash-dot curve is the extrapolated no-stall drag, $C_{D_{NS}}$, and the dotted curve is the equivalent drag of a fully stalled airfoil, $C_{L_{SS}} \sin\alpha$. The solid curve for the unsteady drag is not known a priori and its determination is the object in the present analysis.

The unsteady drag hypothesis to be made here is analogous to the steady drag hypothesis in that the unknown drag deviation from a given datum will be assumed to be proportional to the known lift deviation from a comparable datum. To establish this hypothesis we assume that (1) if the lift followed the potential flow C_{L_P} curve there would be little or no separation and we would expect that the drag would follow the no stall $C_{D_{NS}}$ curve, and (2) if the lift followed the fully stalled $C_{L_{FS}}$ curve this would constitute a fully separated condition and the drag would follow its fully stalled counterpart, $C_{L_{SS}} \sin\alpha$. Thus, if the unsteady lift C_{L_u} is between the steady and the potential flow lift, we assume the unsteady drag to be located proportionately below $C_{D_{SS}}$ and between $C_{D_{SS}}$ and $C_{D_{NS}}$, or

$$C_{D_U} = C_{D_{SS}} - \left(\frac{C_{LU} - C_{L_{SS}}}{C_{L_P} - C_{L_{SS}}}\right)(C_{D_{SS}} - C_{D_{NS}}) \qquad (77)$$

$$C_{L_U} \geq C_{L_{SS}}$$

$$|C_{L_P} - C_{L_{SS}}| > \epsilon$$

where ϵ is some tolerance limit. Conversely, if the unsteady lift C_{L_U} is between the steady and the fully stalled lift, we assume the unsteady drag to be located proportionately above $C_{D_{SS}}$ and between $C_{D_{SS}}$ and $C_{L_{SS}} \sin \alpha$, or

$$C_{D_U} = C_{D_{SS}} + \left(\frac{C_{L_{SS}} - C_{LU}}{C_{L_{SS}} - C_{L_{FS}}}\right)(C_{L_{SS}} \sin \alpha - C_{D_{SS}}) \qquad (78)$$

$$C_{L_U} < C_{L_{SS}}$$

The tolerance restriction in Eq. (77) is necessary to avoid a singular behavior. If in fact C_{L_P} is nearly equal to $C_{L_{SS}}$, which occurs under unstalled conditions, we will usually have a very small value of the drag to begin with, so a reasonable replacement for Eq. (77) under such circumstances is

$$C_{D_U} = C_{D_{NS}} - C_{D_{NS}} \left(\frac{C_{LU} - C_{LP}}{C_{LP}}\right) \qquad (79)$$

$$C_{L_U} \geq C_{L_{SS}}$$

$$|C_{LP} - C_{L_{SS}}| \leq \epsilon$$

In the present analysis the tolerance was taken to be $\epsilon = 10^{-2}$.

These equations were used to calculate the unsteady drag coefficient shown by the solid curve in the lower half of Fig. 46. As before the arrows indicate the direction of increasing time. It can be seen that the hypothetical unsteady drag loop is physically reasonable. In regions of enhanced lift, where separation is delayed, C_{D_u} is smaller than the steady drag, and in regions of lift deterioration, where the flow is heavily separated, C_{D_u} is larger than the steady drag.

This procedure will now be summarized briefly. As part of the lift determination, σ is calculated at each circumferential position, θ. Use this value to enter Fig. 43 to obtain values of the steady airfoil drag, $C_{D_A} = C_{D_{SS}}$, and the drag increment, δ_D. From the computed unsteady airfoil lift and the steady-state airfoil characteristics (previously given) compute unsteady airfoil drag from Eqs. (77), (78), or (79), whichever is appropriate. Add δ_D to this value, as in Eq. (69), to obtain unsteady rotor blade drag, substitute this into Eq. (56) together with the unsteady lift coefficient obtained previously, invert Eq. (56), and proceed with the calculation, as described earlier.

APPENDIX V

CALCULATION PROCEDURES

The circumferential position, θ, is the primary independent variable in this computation, and each of the following steps is carried out at each given value of θ. In the calculations performed herein the input θ increments were chosen to produce a reasonable representation of the input variables by using a high density mesh in the neighborhood of the screen edges and a low density mesh away from the screen edges. The following summary indicates the procedures and the equations used to calculate the results obtained.

1. Given $P_{01}(\theta)$, $p_1(\theta)$, produce graphically a smoothed pressure difference variation $P_{01}(\theta) - p_1(\theta)$, introduce this, $P_{01}(\theta)$, and $\alpha_y(\theta)$ as input.

2. Compute

$$V_{01}(\theta) = \sqrt{\frac{2}{\rho}(P_{01}(\theta) - p_1(\theta))} \tag{80}$$

$$V_A(\theta) = V_{01}(\theta) \sin \alpha_y(\theta) \tag{81}$$

$$V_{\Omega_1}(\theta) = U + V_{01}(\theta) \cos \alpha_y(\theta) \tag{82}$$

$$\beta_1(\theta) = \tan^{-1}\left[V_A(\theta)/V_{\Omega_1}(\theta)\right] \tag{83}$$

$$V_1(\theta) = \sqrt{V_A^2(\theta) + V_{\Omega_1}^2(\theta)} \tag{84}$$

$$\alpha_R(\theta) = \beta_1^* - \beta_1(\theta) \tag{85}$$

where

$$\beta_1^* = 46.29 \text{ deg} \tag{86}$$

$$\sigma_R(\theta) = \frac{\alpha_R(\theta) - \alpha_{R_O}}{\alpha_{R_S} - \alpha_{R_O}} \tag{87}$$

where

$$\left.\begin{aligned} \alpha_{R_O} &= 3.29 \text{ deg} \\ \alpha_{R_S} &= 12 \text{ deg} \end{aligned}\right\} \tag{88}$$

$$\alpha_A(\theta) = \alpha_{A_S}\sigma(\theta) \tag{89}$$

where $$\alpha_{A_S} = 10 \text{ deg} \tag{90}$$

3. Use a numerical differentiation procedure (such as that described in Ref. 13) to compute

$$\alpha_A'(\theta) = d\alpha_A / d\theta \tag{91}$$

$$\alpha_A''(\theta) = d^2\alpha_A / d^2\theta \tag{92}$$

and from the given values of b and Ω, compute

$$A(\theta) = \frac{b\Omega\alpha_A'(\theta)}{V_1(\theta)} \tag{93}$$

$$B(\theta) = \frac{b^2\Omega^2\alpha_A''(\theta)}{V_1^2(\theta)} \tag{94}$$

4. At each value of θ use α_A, A, and B to enter the existing tabulation of unsteady lift and interpolate to obtain the local value of the unsteady airfoil lift, C_{L_u}, and compute the unsteady normalized lift from

$$C_{L_U}^*(\theta) = C_{L_U}(\theta) / 1.02 \tag{95}$$

(as in Eq. (62) for steady-state lift). At this same value of α_A, obtain the steady-state airfoil lift by interpolating at A = B = 0, and call it

$$C_{L_{SS}}(\theta) = C_{L_A}(\theta)_{(A=B=0)} \tag{96}$$

Also compute

$$C_{L_{FS}}(\theta) = \bar{K}\, C_{L_{SS}}(\theta) \tag{97}$$

where $\overline{K}$ will probably be $\overline{K} = 0.5$, and compute

$$C_{L_{SS}}(\theta)\sin\alpha_A(\theta) \tag{98}$$

5. Next we compute the airfoil drag coefficient. Enter Fig. 43 at the appropriate value of σ for each θ and read the airfoil steady-state drag, calling it

$$C_{D_{SS}}(\theta) = C_{D_A}(\theta) \tag{99}$$

Test C_{L_u} versus $C_{L_{SS}}$, and check the difference between C_{L_P} and $C_{L_{SS}}$. If

$$C_{L_U}(\theta) \geq C_{L_{SS}}(\theta) \tag{100}$$

and if

$$|C_{L_p}(\theta) - C_{L_{SS}}(\theta)| > \epsilon \tag{101}$$

(where ϵ is some tolerance, taken to be $\epsilon = 10^{-2}$ herein) then compute

$$C_{D_U}(\theta) = C_{D_{SS}}(\theta) - \left(\frac{C_{L_U}(\theta) - C_{L_{SS}}(\theta)}{C_{L_p}(\theta) - C_{L_{SS}}(\theta)}\right)(C_{D_{SS}}(\theta) - C_{D_{NS}}(\theta)) \tag{102}$$

Here and in the next equation for C_{D_u}, the no-stall drag coefficient, has been idealized as two straight line segments,

$$C_{D_{NS}} = \begin{cases} .0025\,\sigma + .008, & 0 \leq \sigma \leq .8 \\ .0055556(\sigma + 1), & .8 \leq \sigma \leq 2.6 \end{cases} \tag{103}$$

If

$$C_{L_U}(\theta) \geq C_{L_{SS}}(\theta) \tag{104}$$

and if

$$|C_{L_p}(\theta) - C_{L_{SS}}(\theta)| \leq \epsilon \tag{105}$$

then compute

$$C_{D_U}(\theta) = C_{D_{NS}}(\theta) - C_{D_{NS}}(\theta)\left(\frac{C_{L_U}(\theta) - C_{L_p}(\theta)}{C_{L_p}(\theta)}\right) \tag{106}$$

Finally, if

$$C_{L_U}(\theta) < C_{L_{SS}}(\theta) \tag{107}$$

then compute

$$C_{D_U}(\theta) = C_{D_{SS}}(\theta) + \left(\frac{C_{L_{SS}}(\theta) - C_{L_U}(\theta)}{C_{L_{SS}}(\theta) - C_{L_{FS}}(\theta)}\right)(C_{L_{SS}}(\theta)\sin\alpha_A(\theta) - C_{D_{SS}}(\theta)) \tag{108}$$

6. Now convert both the steady and the unsteady lift and drag coefficients on the airfoil to their counterparts on the rotor blade using the lift and drag increment functions plotted in Figs. 42 and 43, respectively. The unsteady coefficients become

$$C^*_{L_R}(\theta) = C^*_{L_U}(\theta) + \delta_L(\theta) \tag{109}$$

$$C_{D_R}(\theta) = C_{D_U}(\theta) + \delta_D(\theta) \tag{110}$$

and the steady-state coefficients become

$$C^*_{L_{RSS}}(\theta) = C^*_{L_{SS}}(\theta) + \delta_L(\theta) \tag{111}$$

$$C_{D_{RSS}}(\theta) = C_{D_{SS}}(\theta) + \delta_D(\theta) \tag{112}$$

The normalized lift in Eqs. (109) and (111) are converted to rotor lift by solving Eq. (62) for $C_{L_R}(\theta)$ and inserting the appropriate numerical values of the constants. In the present case, for both steady and unsteady lift, the formula is

$$C_{L_R}(\theta) = .167\,C^*_{L_R}(\theta) + .265 \tag{113}$$

7. Next compute the steady and the unsteady force coefficients. Use Eq. (7) written in coefficient form.

$$C_{F_A}(\theta) = C_{L_R}(\theta)\cos\beta_1(\theta) - C_{D_R}(\theta)\sin\beta_1(\theta) \tag{114}$$

$$C_{F_\Omega}(\theta) = C_{L_R}(\theta)\sin\beta_1(\theta) + C_{D_R}(\theta)\cos\beta_1(\theta) \tag{115}$$

8. Now compute the static and total pressure profiles at the rotor exit plane, using Eqs. (8) and (9),

$$p_2(\theta) = p_1(\theta) + \frac{\rho V_1^2(\theta)}{2\tau/c}\,C_{F_A}(\theta) \tag{116}$$

$$P_{02}(\theta) = p_2(\theta) + \frac{1}{2}\rho\left[V_A^2(\theta) + \left(U - V_{\Omega_1}(\theta) + \frac{V_1^2(\theta)C_{F_\Omega}(\theta)}{2(\tau/c)V_A(\theta)}\right)^2\right] \tag{117}$$

9. From Eq. (40) compute the static pressure coefficient,

$$\psi_R(\theta) = \frac{p_2(\theta) - p_1(\theta)}{(p_1(\theta) + P_{ref})\bar{N}^2} \tag{118}$$

and from Eq. (46) compute the flow coefficient

$$\phi(\theta) = \frac{68{,}051\,\rho V_A(\theta)}{(P_{01}(\theta) + P_{ref})\bar{N}} \tag{119}$$

where P_{ref} is the local atmospheric pressure in pounds/ft^2. The corrected wheel speed ratio is defined in Eq. (45) and was numerically given by

$$\bar{N} = 0.4495 \tag{120}$$

in this analysis.

10. To calculate stator exit quantities, first compute the stator inlet angle. From Eq. (38) write

$$\alpha_2 = \tan^{-1}\left\{\frac{V_A(\theta)}{U - V_{\Omega_1}(\theta) + \dfrac{V_1^2(\theta)\,C_{F_\Omega}(\theta)}{2(\tau/c)V_A(\theta)}}\right\} \tag{121}$$

The denominator in this equation was previously computed as part of Eq. (117). At each value of θ, enter Fig. 33 at the computed value of α_2 and obtain a value for ψ_S. Then use Eq. (11) to calculate the stage exit static pressure variation,

$$p_3(\theta) = p_2(\theta) + (p_2(\theta) + P_{ref})\bar{N}^2\,\psi_S(\theta) \tag{122}$$

APPENDIX VI

RADIAL EQUILIBRIUM CORRECTION

If there is no radial component of velocity, the fluid is in radial equilibrium and the equation governing the static pressure can be simplified to (cf. p. 8 of Ref. 6)

$$\frac{dp}{dr} = \rho \omega^2 r \tag{123}$$

where ω is the (constant) angular velocity of the fluid in the absolute frame of reference. When Eq. (123) is integrated between the mid-annulus (subscript M) and the wall (subscript W) the result is

$$p_W - p_M = \frac{1}{2} \rho \omega^2 (r_W^2 - r_M^2) \tag{124}$$

In Fig. 4 it is seen that the absolute tangential velocity at the exit plane is $V_A/\tan \alpha_2$, and at the mid-annulus this is related to ω by the formula

$$\left(\frac{V_A}{\tan \alpha_2} \right)_M = \omega r_M \tag{125}$$

Thus, the mid-annulus pressure from Eq. (124) is reduced from the wall value according to the equation

$$p_M = p_W - \frac{1}{2} \rho \left(\frac{V_A}{\tan \alpha_2} \right)_M \left[\left(\frac{r_W}{r_M} \right)^2 - 1 \right] \tag{126}$$

TABLE I

STEADY-STATE ROTOR CHARACTERISTICS

(Axial Flow Inlet, α_1 = 90 deg)

β_1	ϕ	ψ_R	α_2	V_A	V_{01}	V_{02}	P_{01} + P_{ref}	$\overline{N}$
deg	$\frac{lb/sec}{ft^2}$		deg	ft/sec	ft/sec	ft/sec	lb/ft^2	
27.2	12.8	0.0243	43.9	76.0	76.1	109.5	2110.93	0.4512
28.0	13.2	0.0266	45.6	78.3	78.4	109.4	2110.52	0.4503
28.9	13.7	0.0288	47.8	81.3	81.4	109.6	2110.26	0.4503
29.6	14.1	0.0305	49.5	83.8	83.9	109.9	2109.97	0.4503
30.4	14.55	0.0320	51.5	86.6	86.7	110.4	2109.72	0.4501
31.6	15.3	0.0338	54.5	90.9	91.0	111.3	2109.33	0.4503
33.5	16.4	0.0352	59.0	97.5	97.7	113.5	2108.86	0.4506
35.1	17.4	0.0355	63.0	103.4	103.6	115.9	2108.48	0.4504
36.2	18.1	0.0353	65.6	107.6	107.8	118.0	2108.19	0.4503
37.8	19.2	0.0347	69.6	114.2	114.4	121.6	2107.79	0.4501

FIG. 1

TYPICAL AXIAL VELOCITY DISTORTION

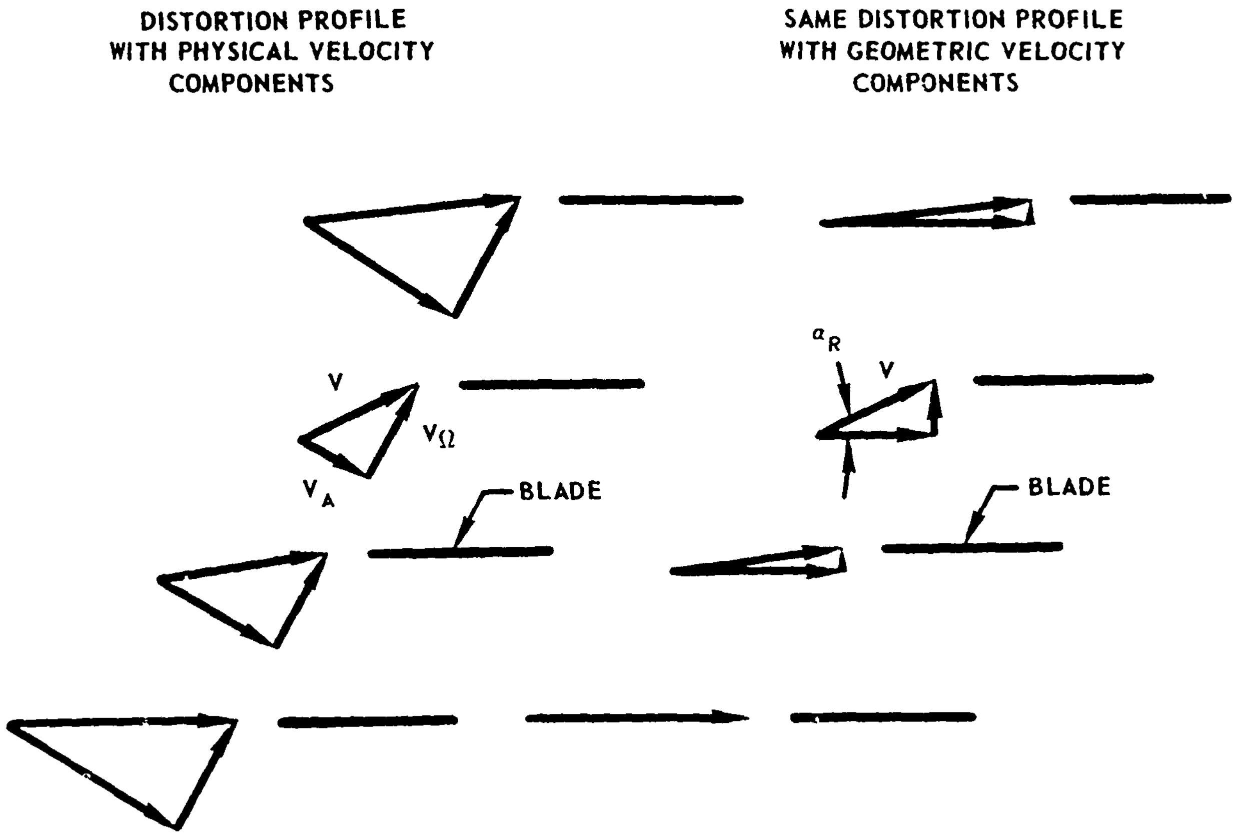
DISTORTION PROFILE
WITH PHYSICAL VELOCITY
COMPONENTS
SAME DISTORTION PROFILE
WITH GEOMETRIC VELOCITY
COMPONENTS
V
V_Ω
V_A
BLADE
α_R
V
BLADE

V_A AXIAL VELOCITY

V_Ω TANGENTIAL VELOCITY

V - RESULTANT VELOCITY

α_R -- ROTOR BLADE ANGLE OF ATTACK

FIG. 2

TYPICAL REDUCED COMPRESSOR SENSITIVITY TO MULTILOBE DISTORTION PATTERNS

(FROM REF. 1)

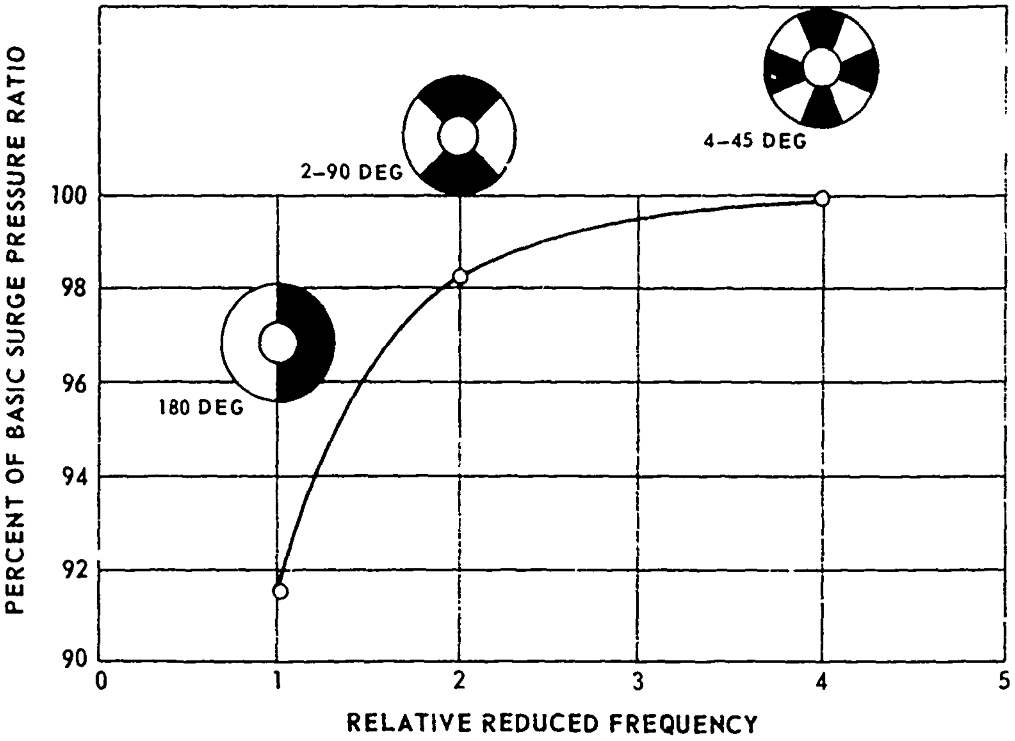

BLADE ROW GEOMETRY AND NOMENCLATURE

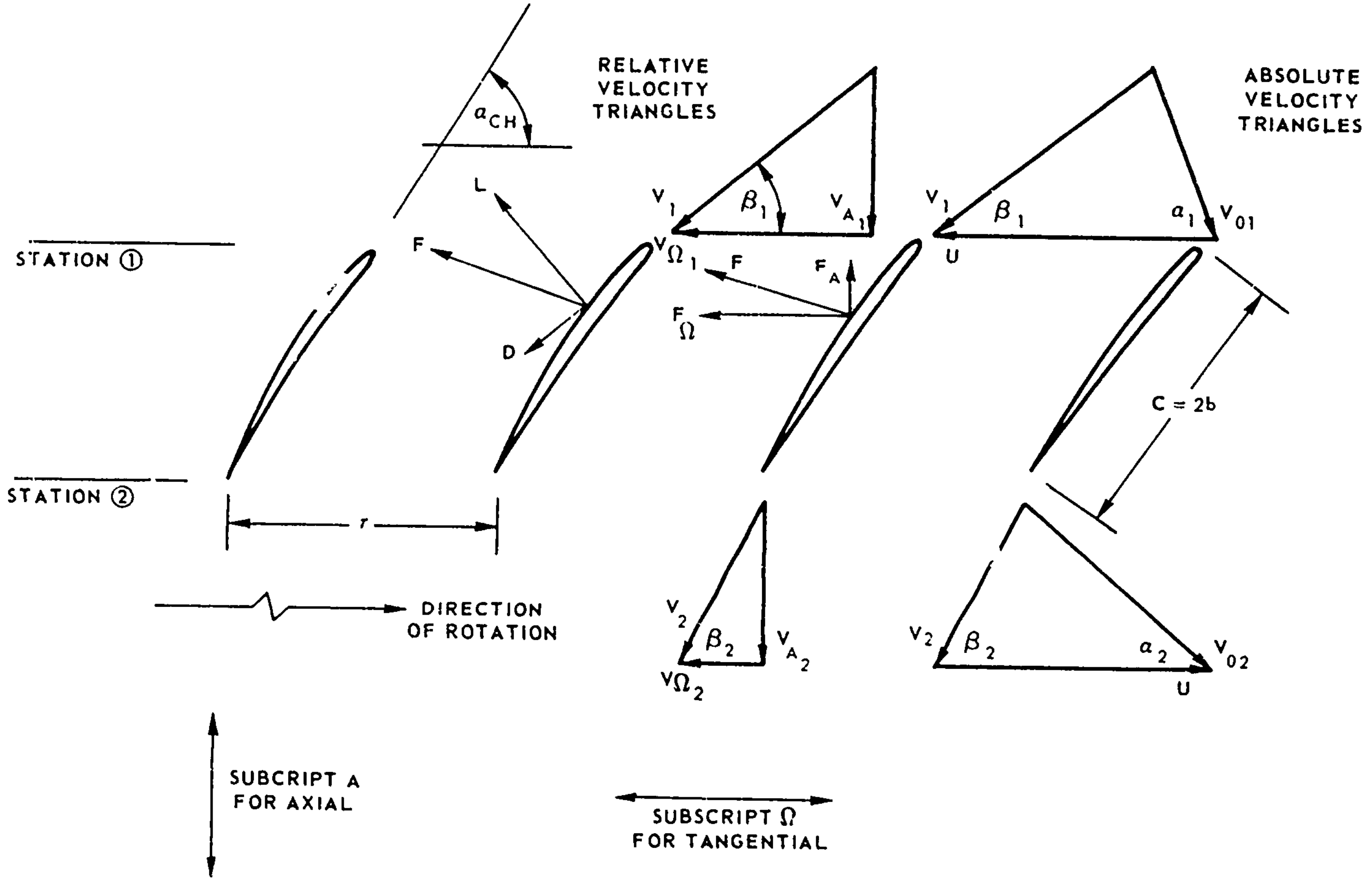
RELATIVE VELOCITY TRIANGLES
ABSOLUTE VELOCITY TRIANGLES
a_{CH}
L
F
D
STATION ①
STATION ②
r
V_1
β_1
V_{A_1}
$V\Omega_1$
F
F_A
F_Ω
V_1
β_1
a_1
V_{01}
U
C = 2b
DIRECTION OF ROTATION
V_2
β_2
V_{A_2}
$V\Omega_2$
V_2
β_2
a_2
V_{02}
U
SUBCRIPT A FOR AXIAL
SUBSCRIPT Ω FOR TANGENTIAL

FIG. 4

VELOCITY TRIANGLES

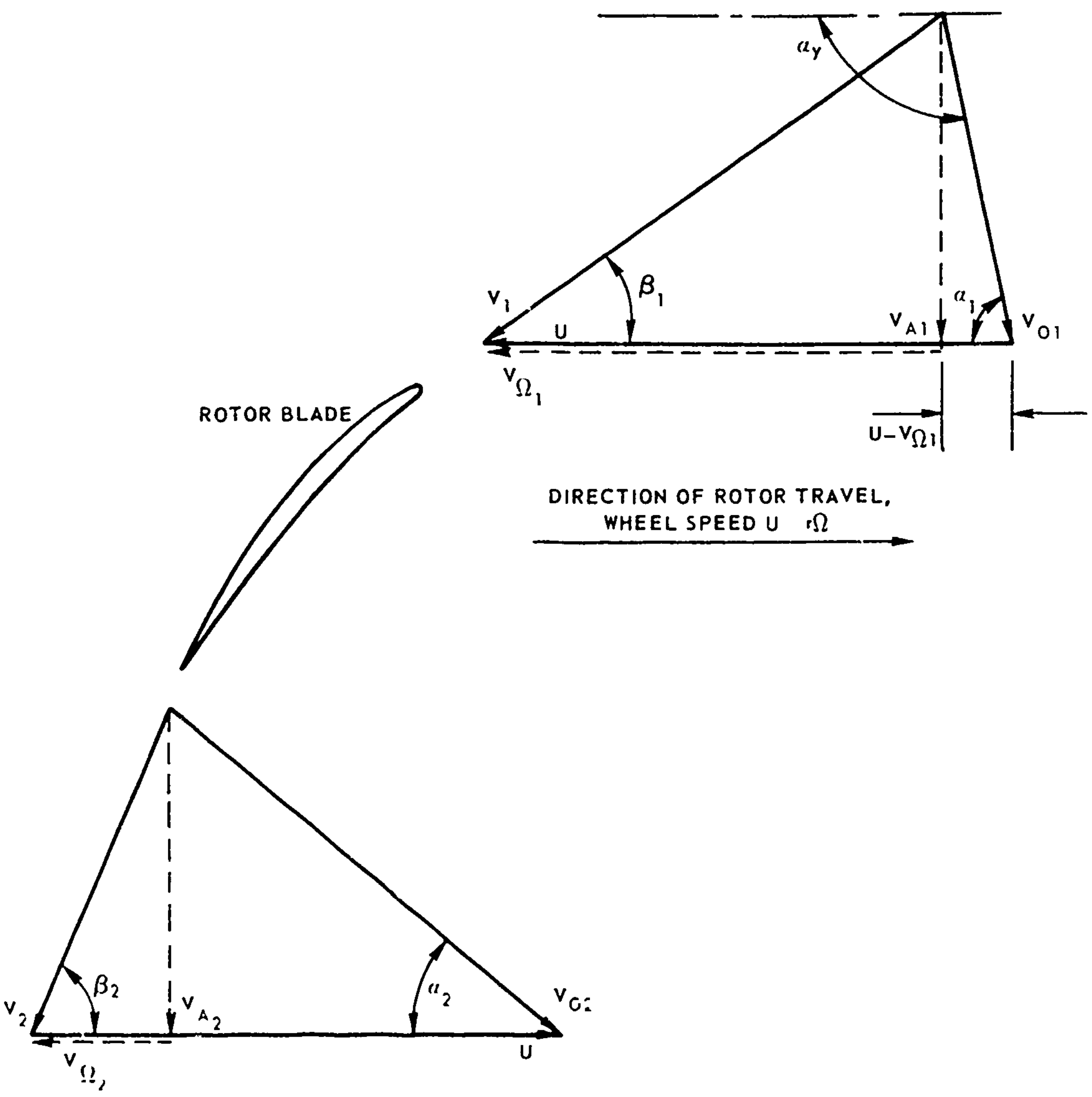

α_y
β_1
V_1
U
V_{A1}
α_1
V_{O1}
V_{Ω_1}
$U-V_{\Omega 1}$
ROTOR BLADE
DIRECTION OF ROTOR TRAVEL,
WHEEL SPEED U rΩ
β_2
V_2
V_{A_2}
α_2
V_{O2}
U
V_{Ω_2}

FIG. 5

ROTOR BLADE ANGLE OF ATTACK AND FORCE DIRECTIONS

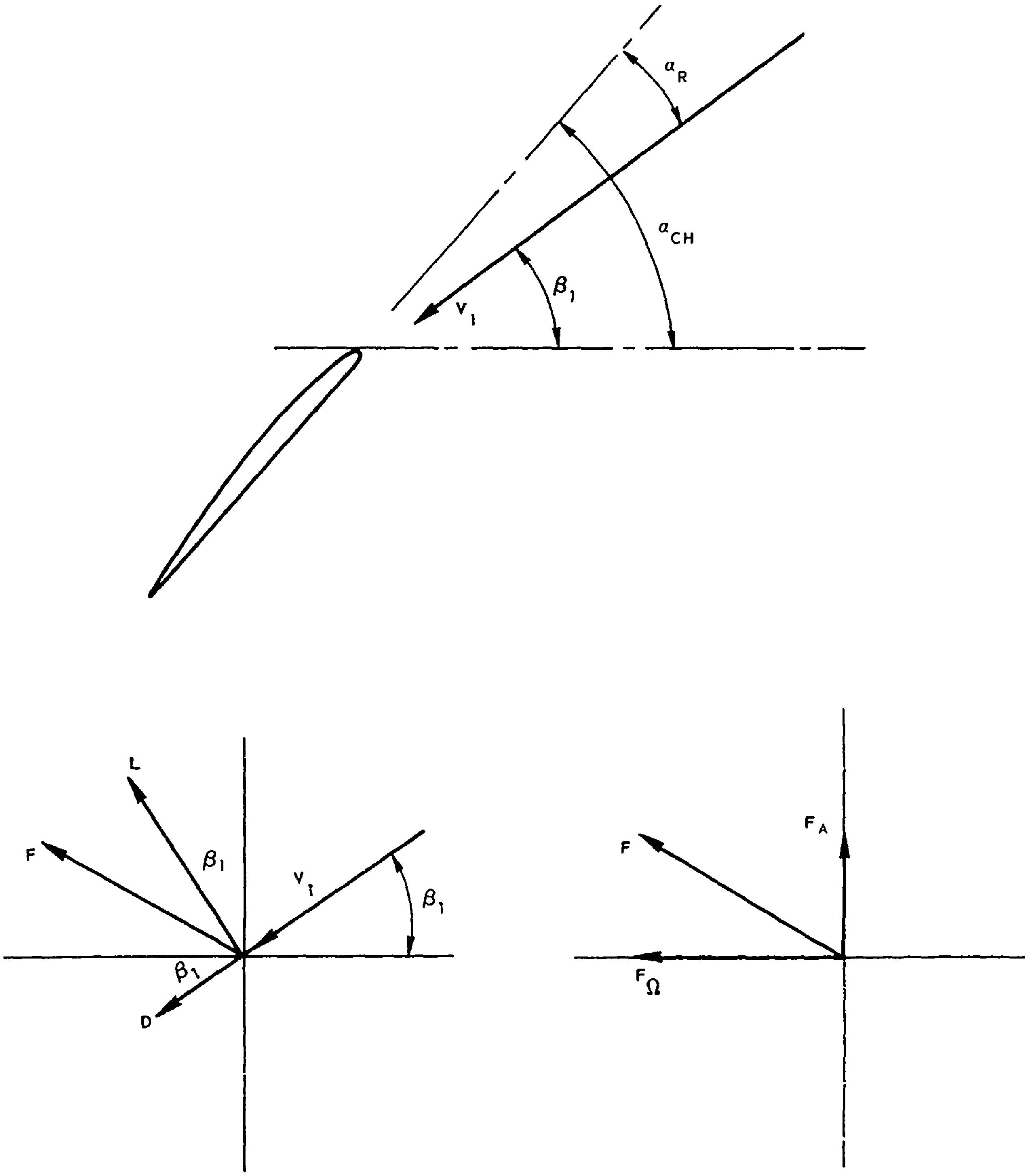

α_R
α_{CH}
β_1
V_1
L
F
β_1
V_1
β_1
β_1
D
F_A
F
F_Ω

FIG. 6

THREE-STAGE AXIAL-FLOW COMPRESSOR

STEADY STATE INSTRUMENTATION LOCATIONS

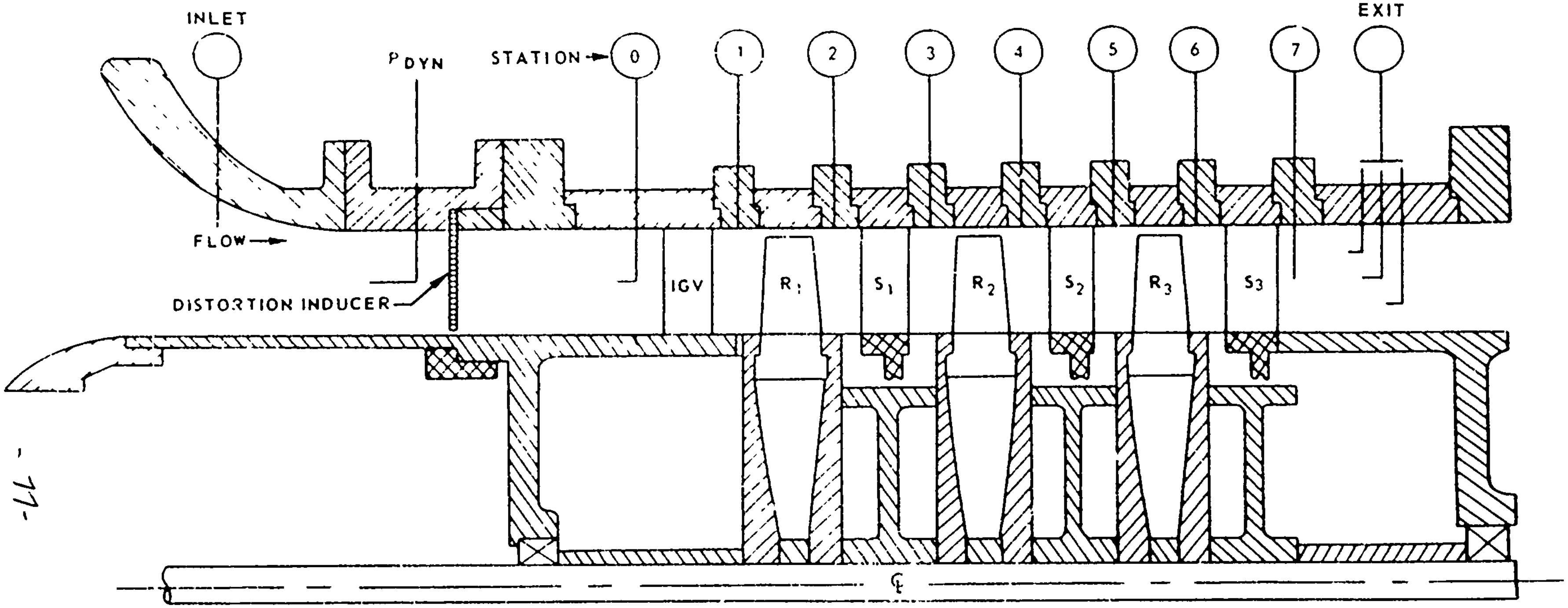
INLET
P_{DYN}
STATION
0
1
2
3
4
5
6
7
EXIT
FLOW
DISTORTION INDUCER
IGV
R_1
S_1
R_2
S_2
R_3
S_3
℄

PRESSURE MEASUREMENT LOCATIONS

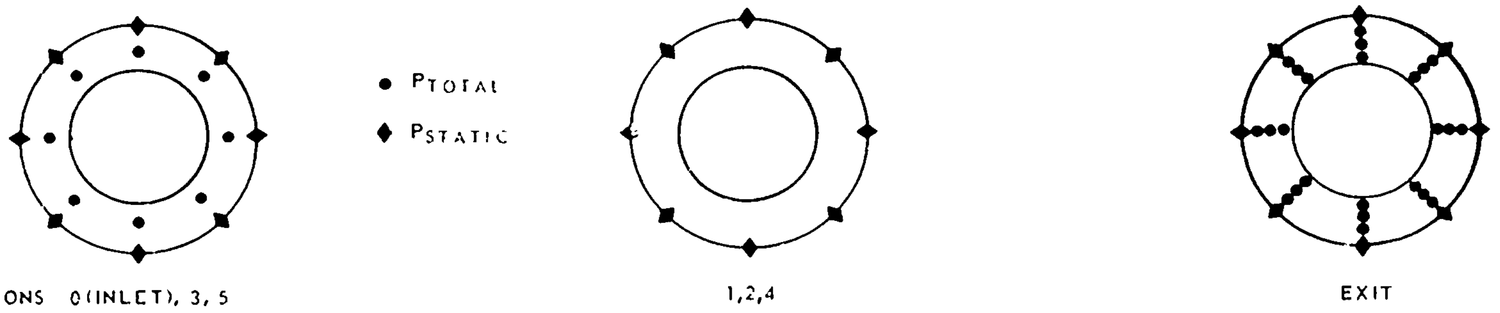
● P_{TOTAL}
◆ P_{STATIC}
STATIONS 0(INLET), 3, 5
1,2,4
EXIT

FIG. 7

FIRST STAGE STEADY-STATE CHARACTERISTICS FROM UARL THREE-STAGE COMPRESSOR

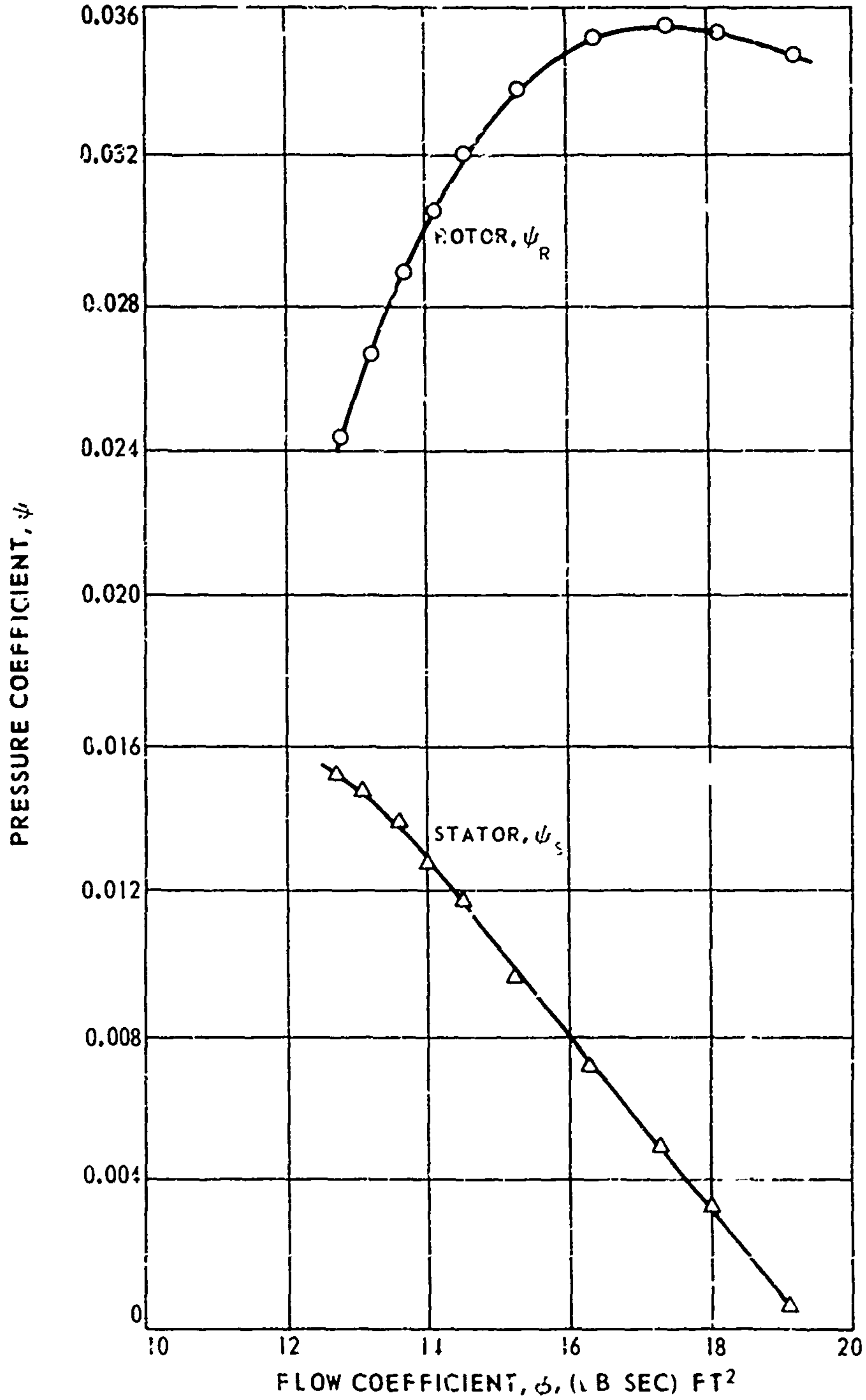

- 78

FIG. 8

MEASURED CIRCUMFERENTIAL TOTAL PRESSURE PROFILE AT MID-ANNULUS FOR 180 DEG DISTORTION EXTENT - PEAK PRESSURE CONDITION

P_{ref} - 404.33 IN. H_2O

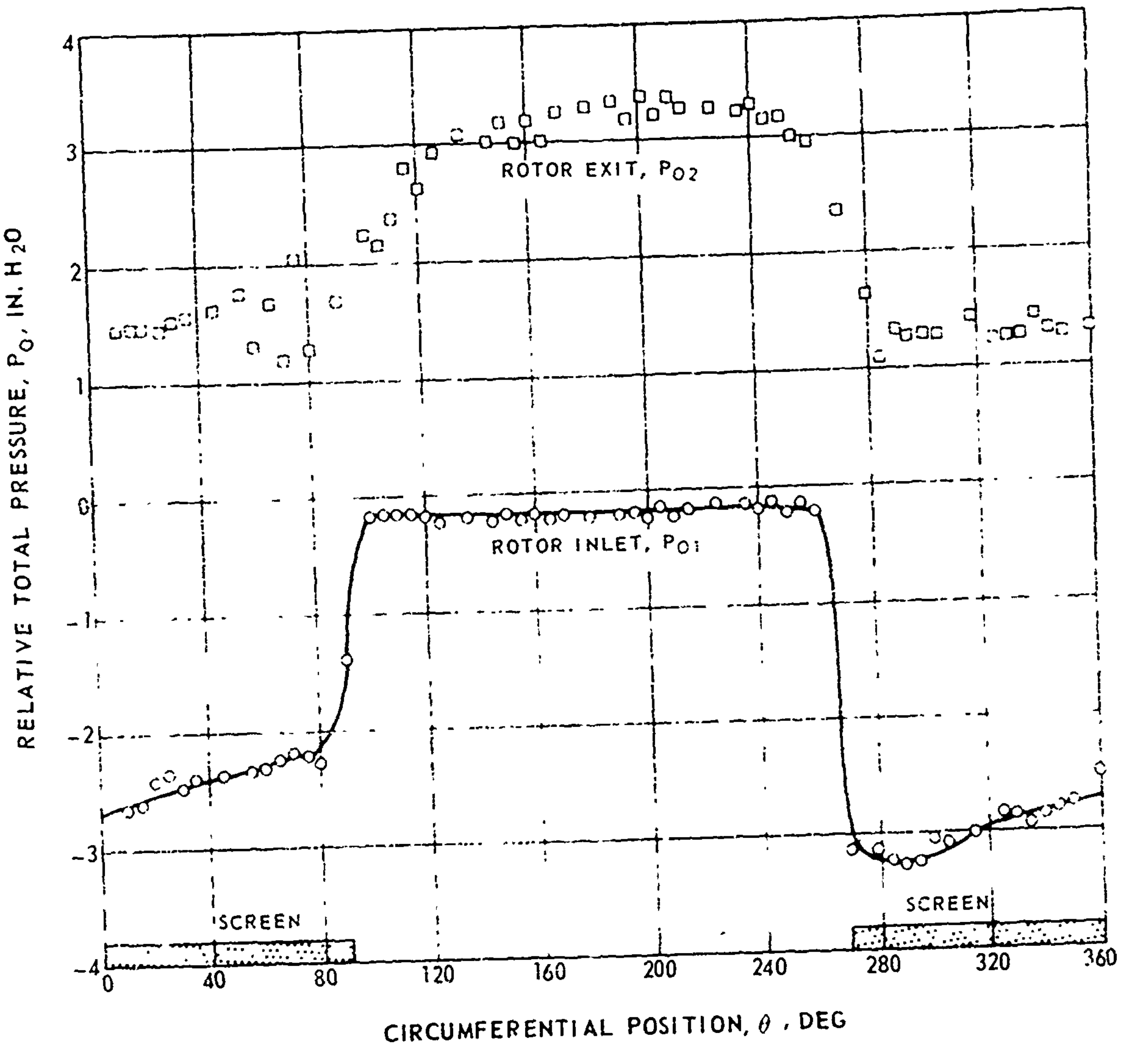

FIG. 9

MEASURED CIRCUMFERENTIAL STATIC PRESSURE PROFILE AT OUTER DIAMETER FOR 180 DEG DISTORTION EXTENT - PEAK PRESSURE CONDITION

P_{ref} = 404.33 IN. H_2O

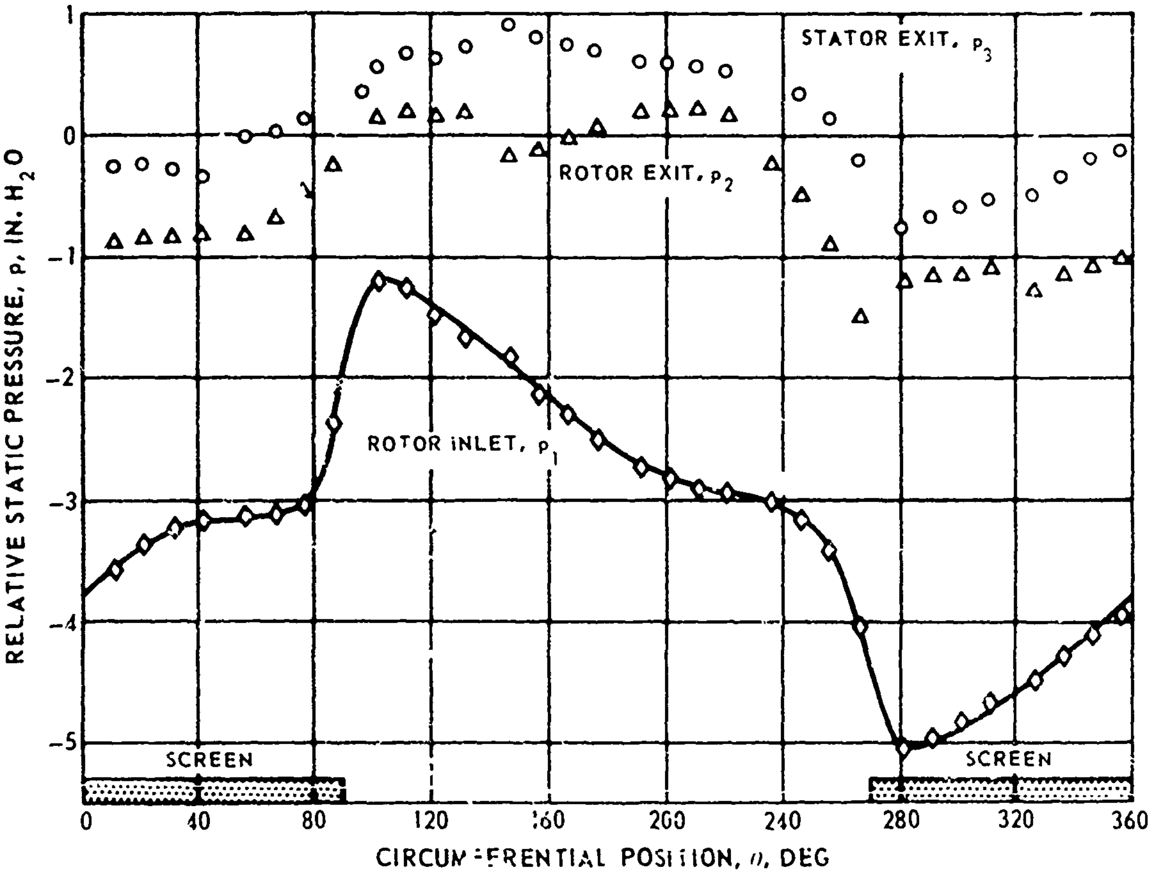

MEASURED CIRCUMFERENTIAL YAW ANGLE PROFILE AT MID-ANNULUS FOR
180 DEG DISTORTION EXTENT – PEAK PRESSURE CONDITION

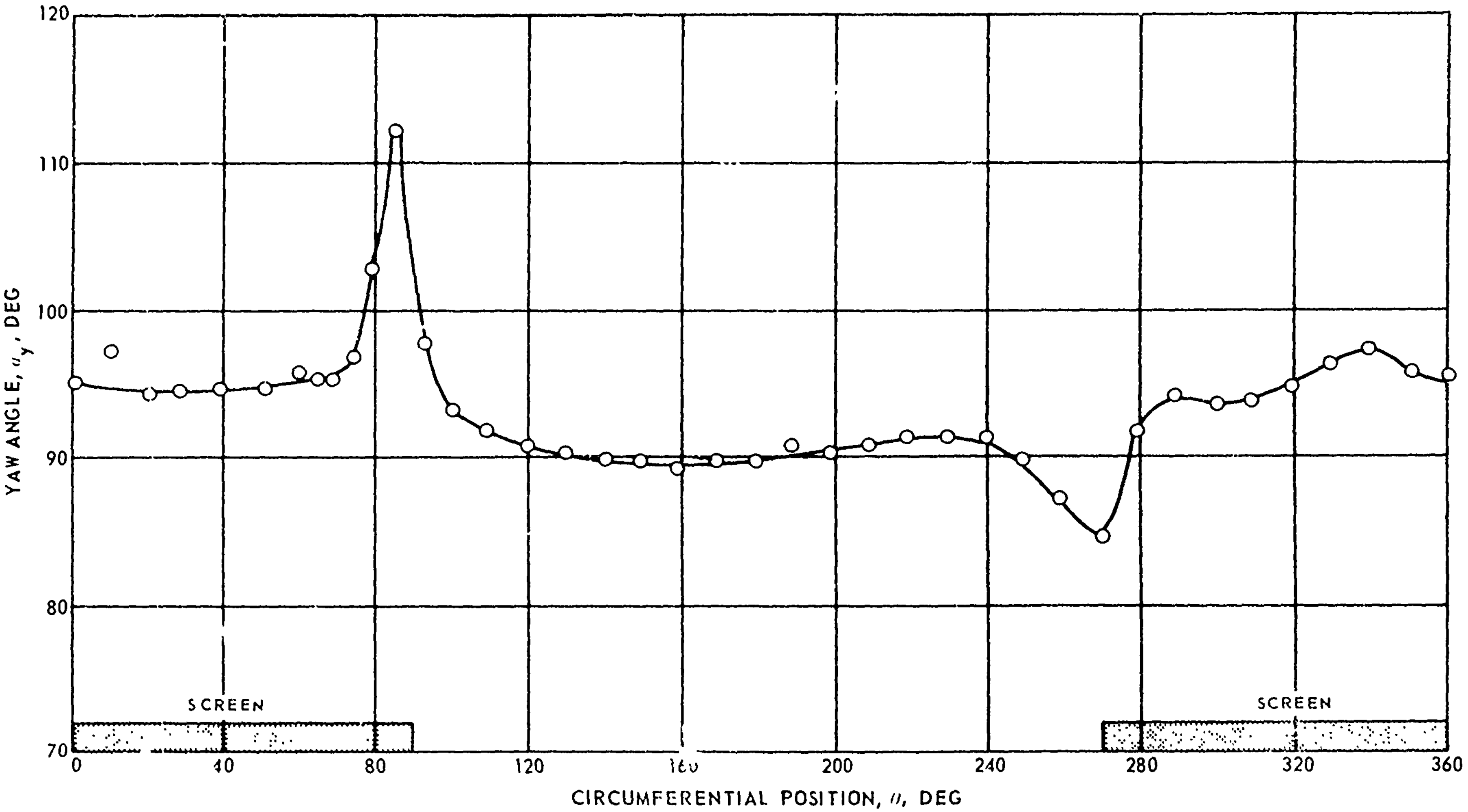

FIG. 10

CIRCUMFERENTIAL VARIATION IN STALL ANGLE PARAMETER FOR 180 DEG DISTORTION EXTENT – PEAK PRESSURE CONDITION

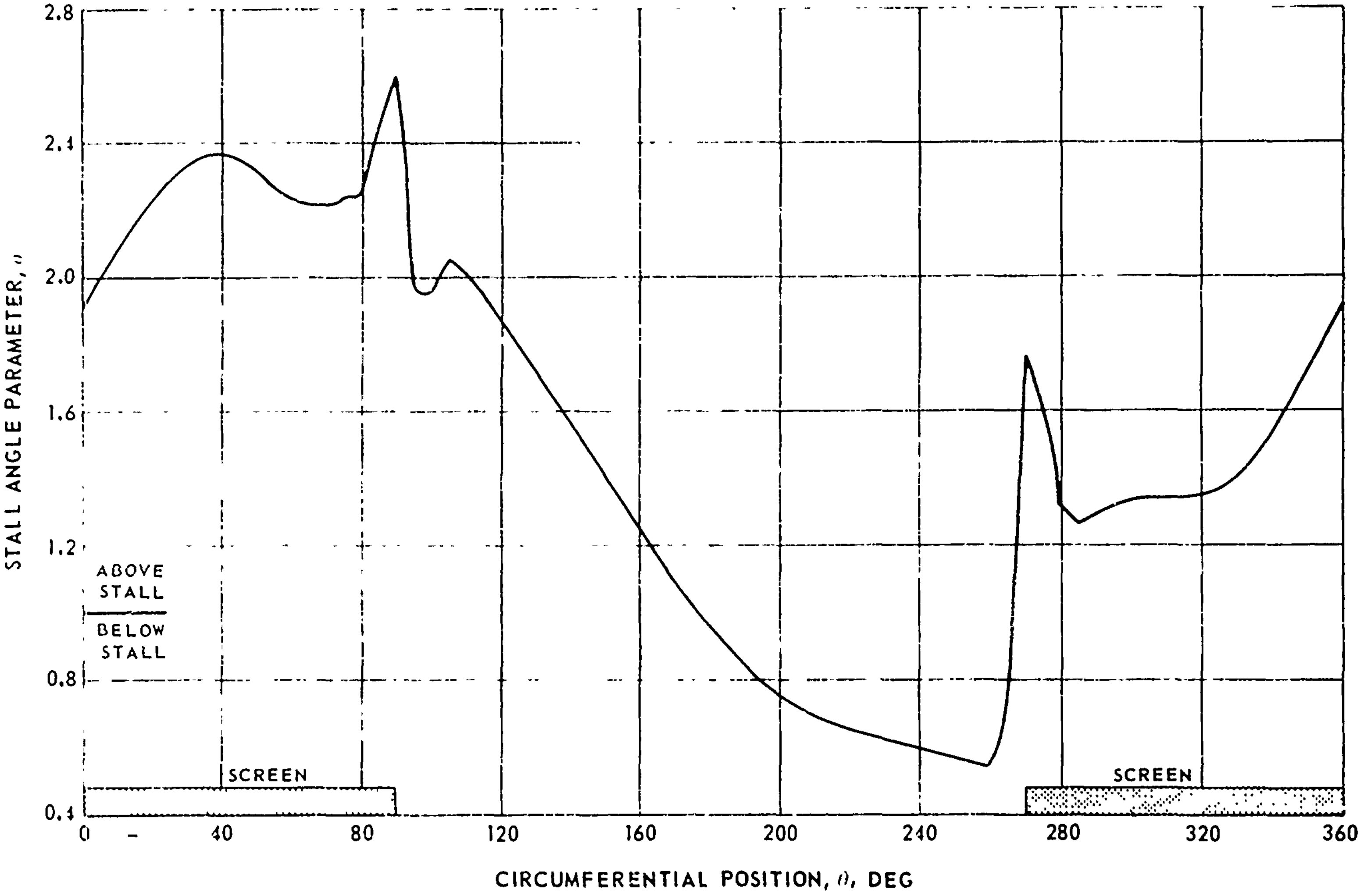

FIG. 11

FIG. 12

CIRCUMFERENTIAL VARIATION IN ROTOR BLADE LIFT COEFFICIENT FOR
180 DEG DISTORTION EXTENT - PEAK PRESSURE CONDITION

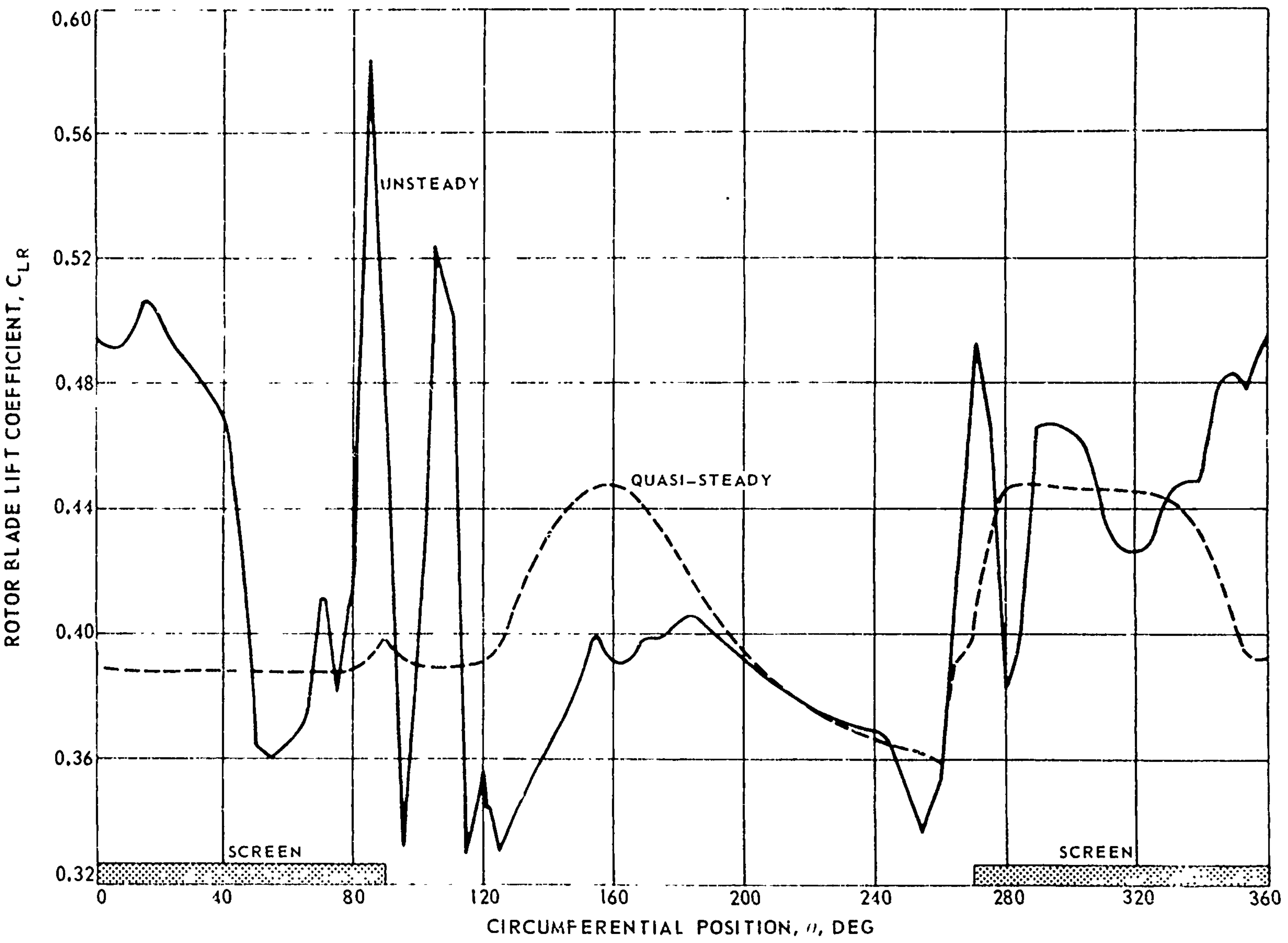

FIG. 13

CIRCUMFERENTIAL VARIATION IN ROTOR BLADE DRAG COEFFICIENT FOR
180 DEG DISTORTION EXTENT – PEAK PRESSURE CONDITION

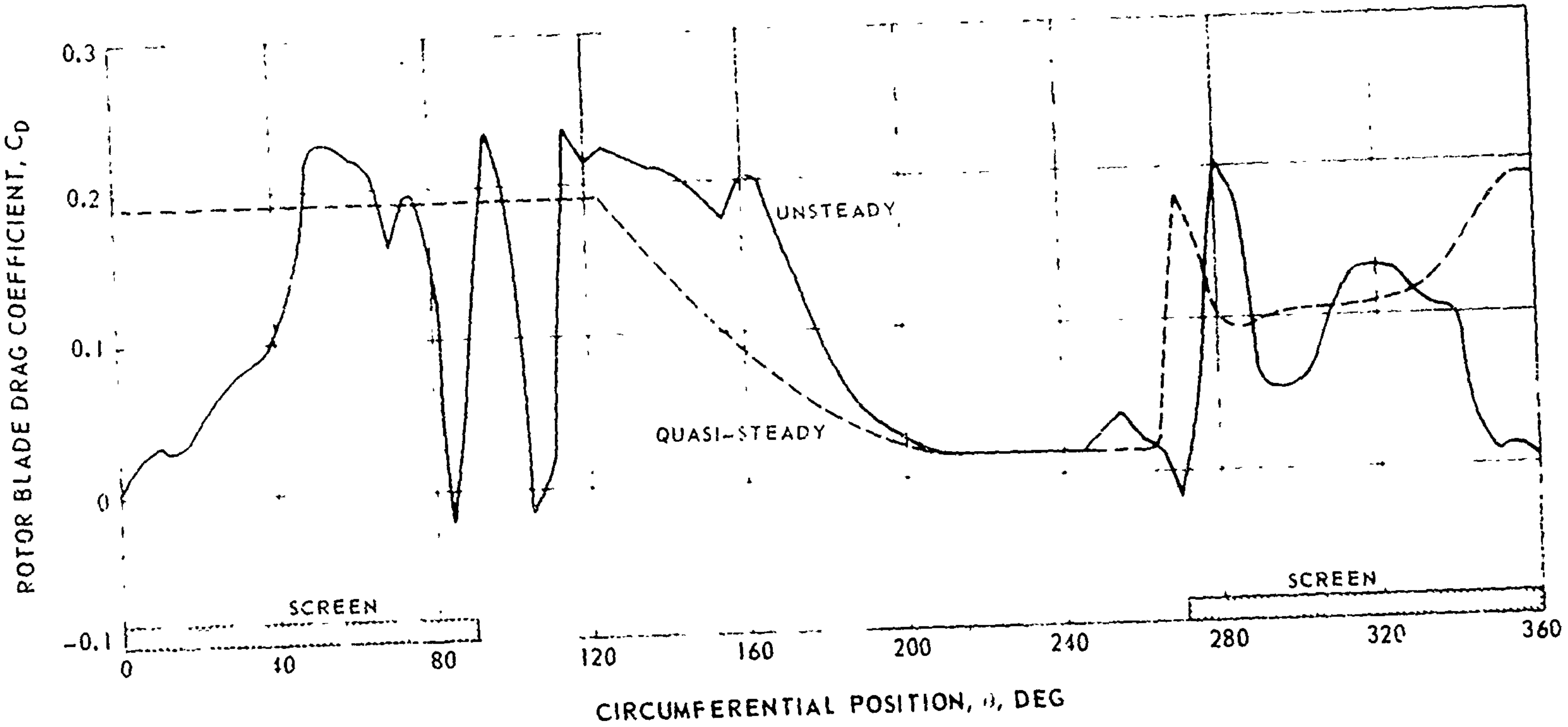

COMPARISON BETWEEN PREDICTED AND MEASURED MID-ANNULUS TOTAL PRESSURE AT ROTOR EXIT PLANE FOR 180 DEG DISTORTION EXTENT PEAK PRESSURE CONDITION

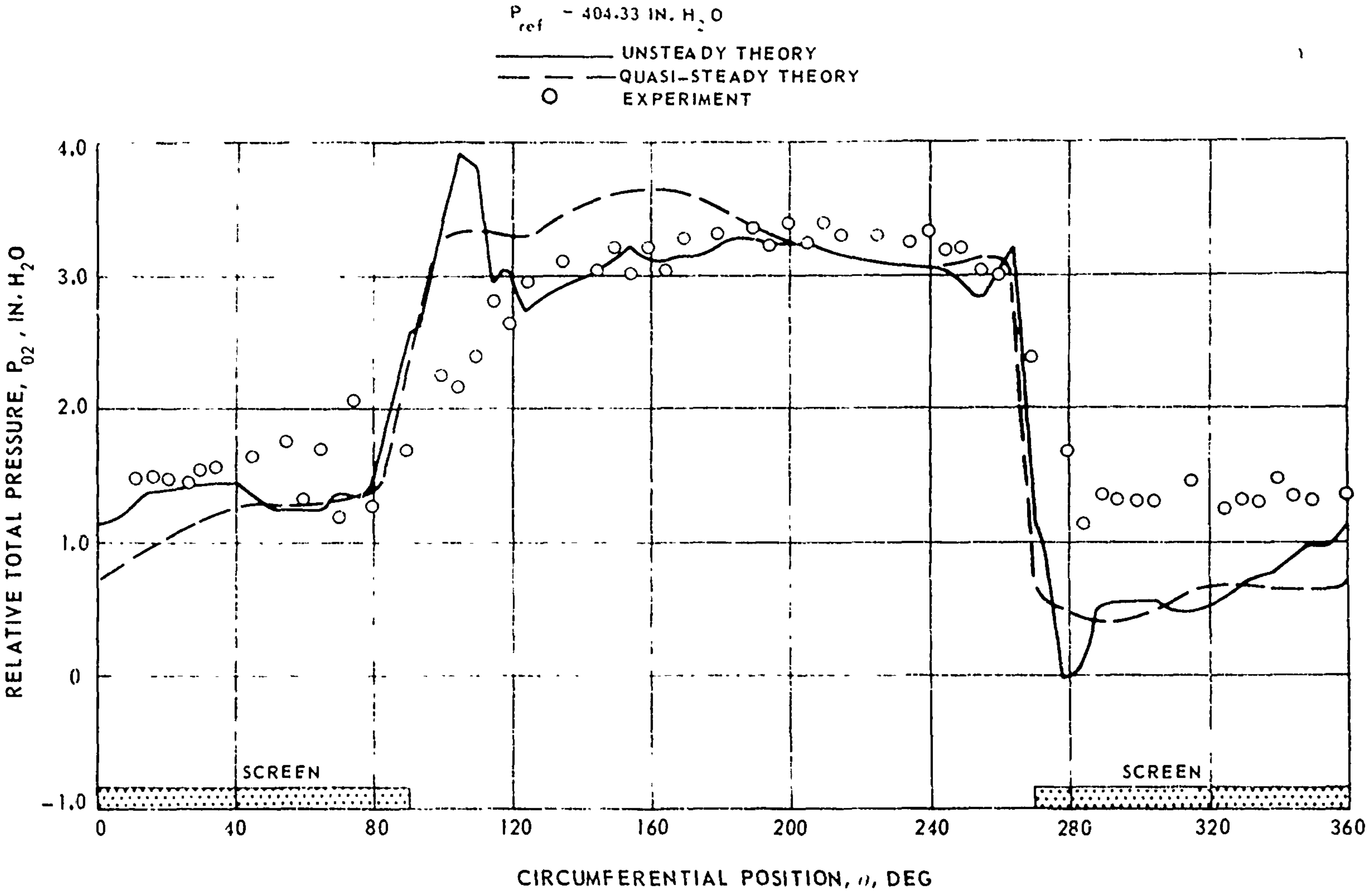

FIG. 14

COMPARISON BETWEEN PREDICTED AND MEASURED MID-ANNULUS STATIC PRESSURE AT ROTOR EXIT PLANE FOR 180 DEG DISTORTION EXTENT – PEAK PRESSURE CONDITION

P_{ref} – 404.33 IN. H_2O

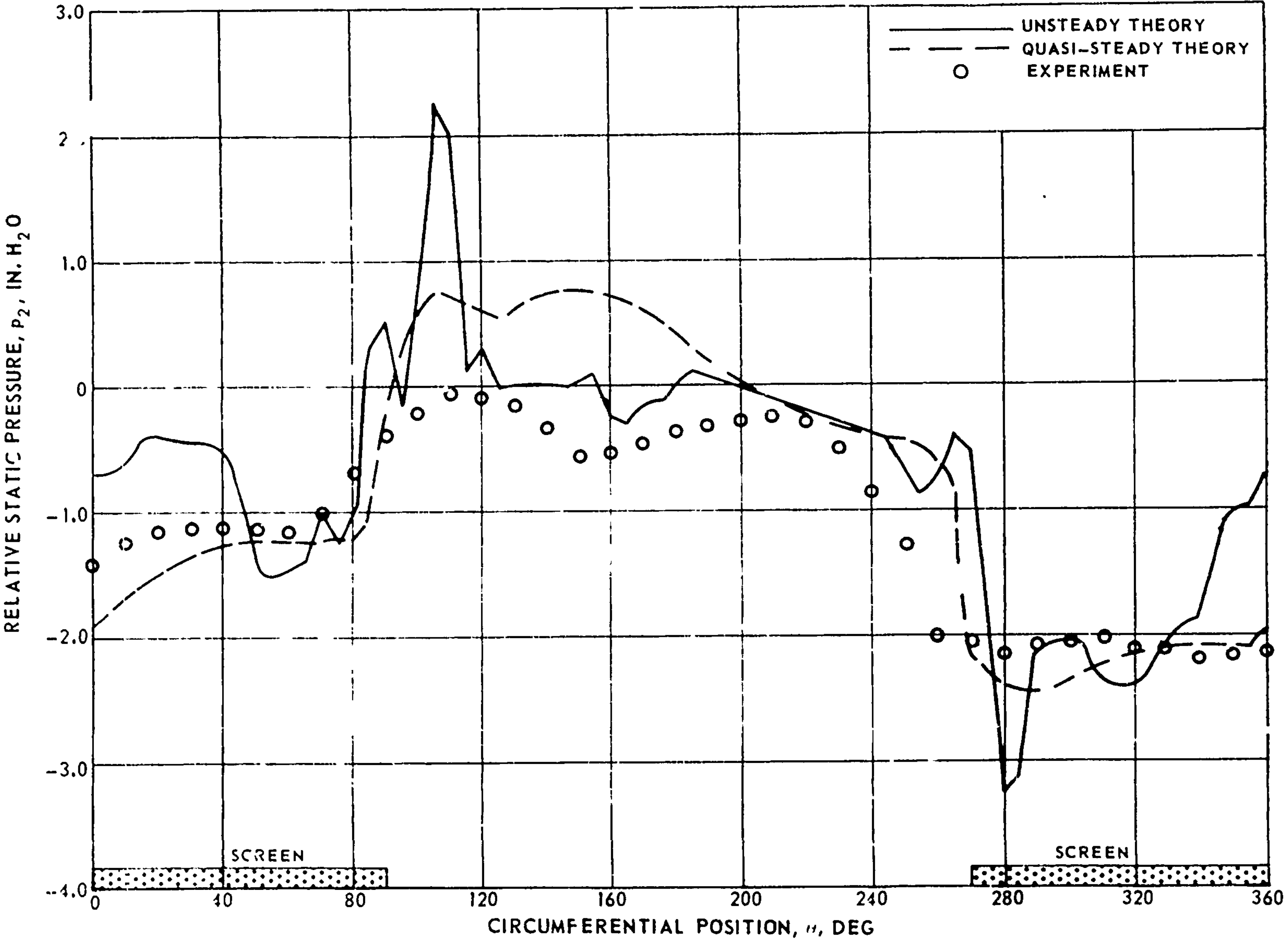

FIG. 15

COMPARISON BETWEEN PREDICTED AND MEASURED MID-ANNULUS STATIC PRESSURE COEFFICIENT AT ROTOR EXIT PLANE FOR 180 DEG DISTORTION EXTENT – PEAK PRESSURE CONDITION

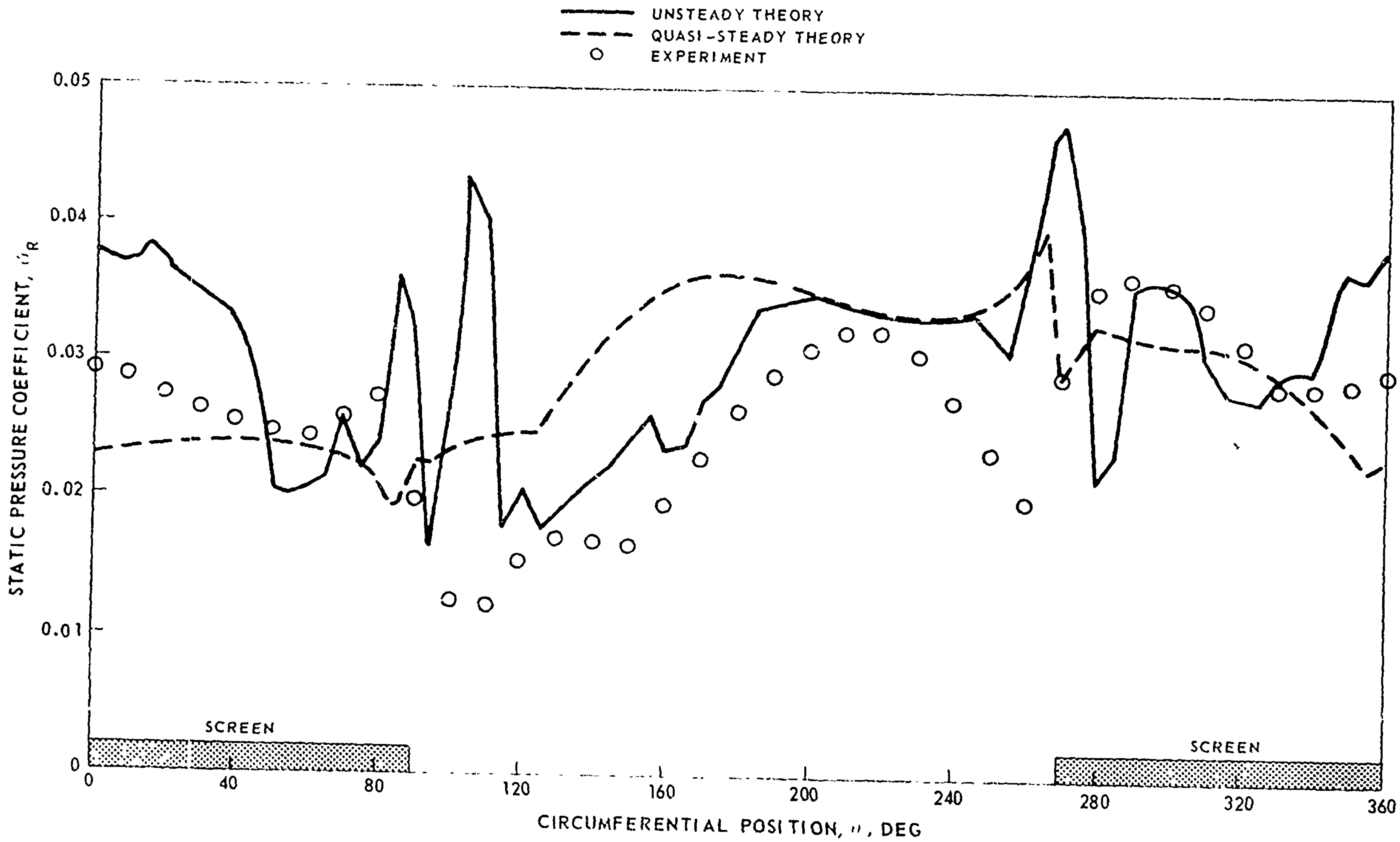

FIG. 16

MEASURED CIRCUMFERENTIAL TOTAL PRESSURE PROFILE AT MID-ANNULUS FOR 180 DEG DISTORTION EXTENT – MIDFLOW CONDITION

P_{ref} = 415.1 IN. H_2O

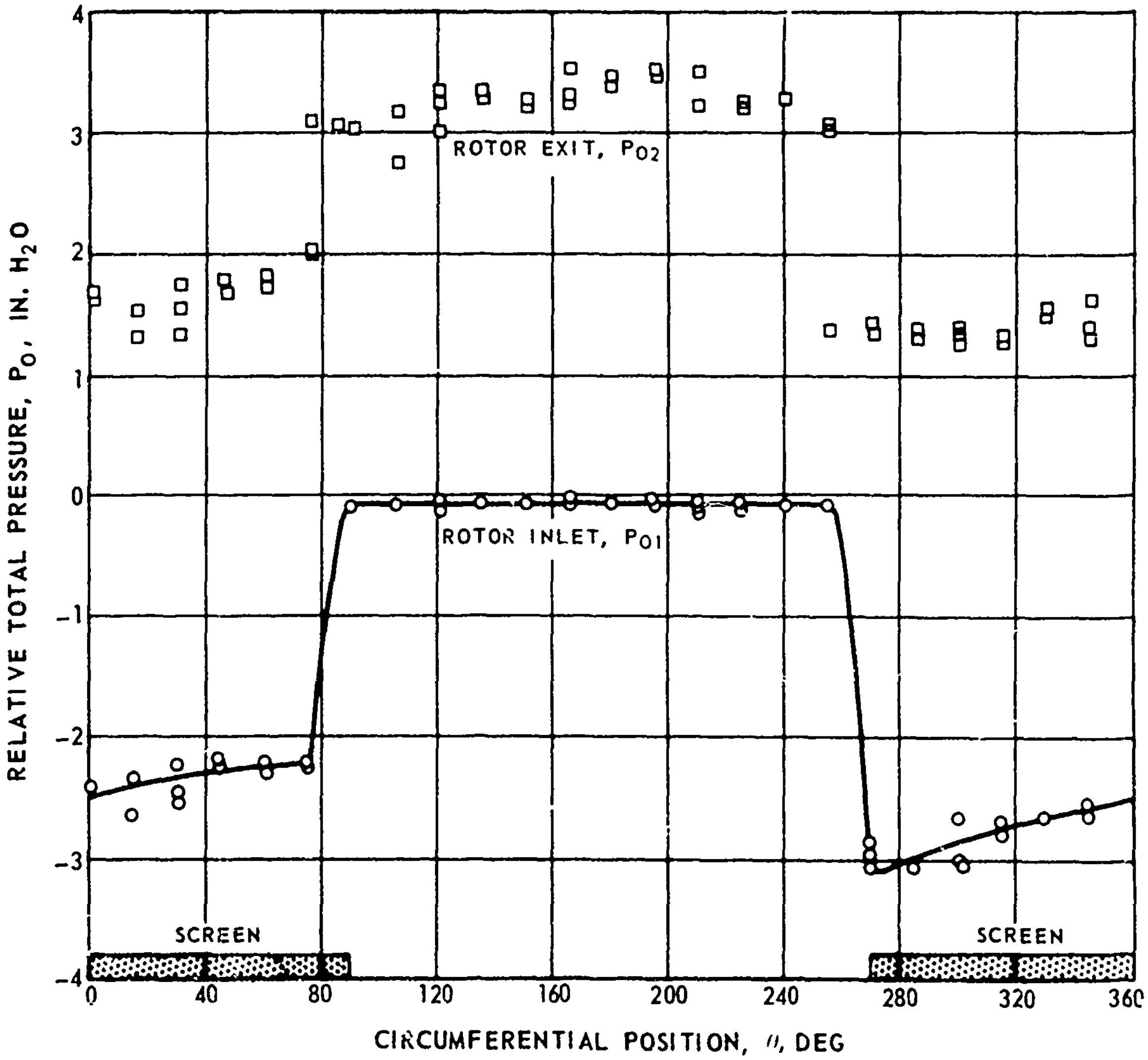

FIG. 18

MEASURED CIRCUMFERENTIAL STATIC PRESSURE PROFILE AT OUTER DIAMETER FOR 180 DEG DISTORTION EXTENT – MIDFLOW CONDITION

P_{ref} – 415.1 IN H_2O

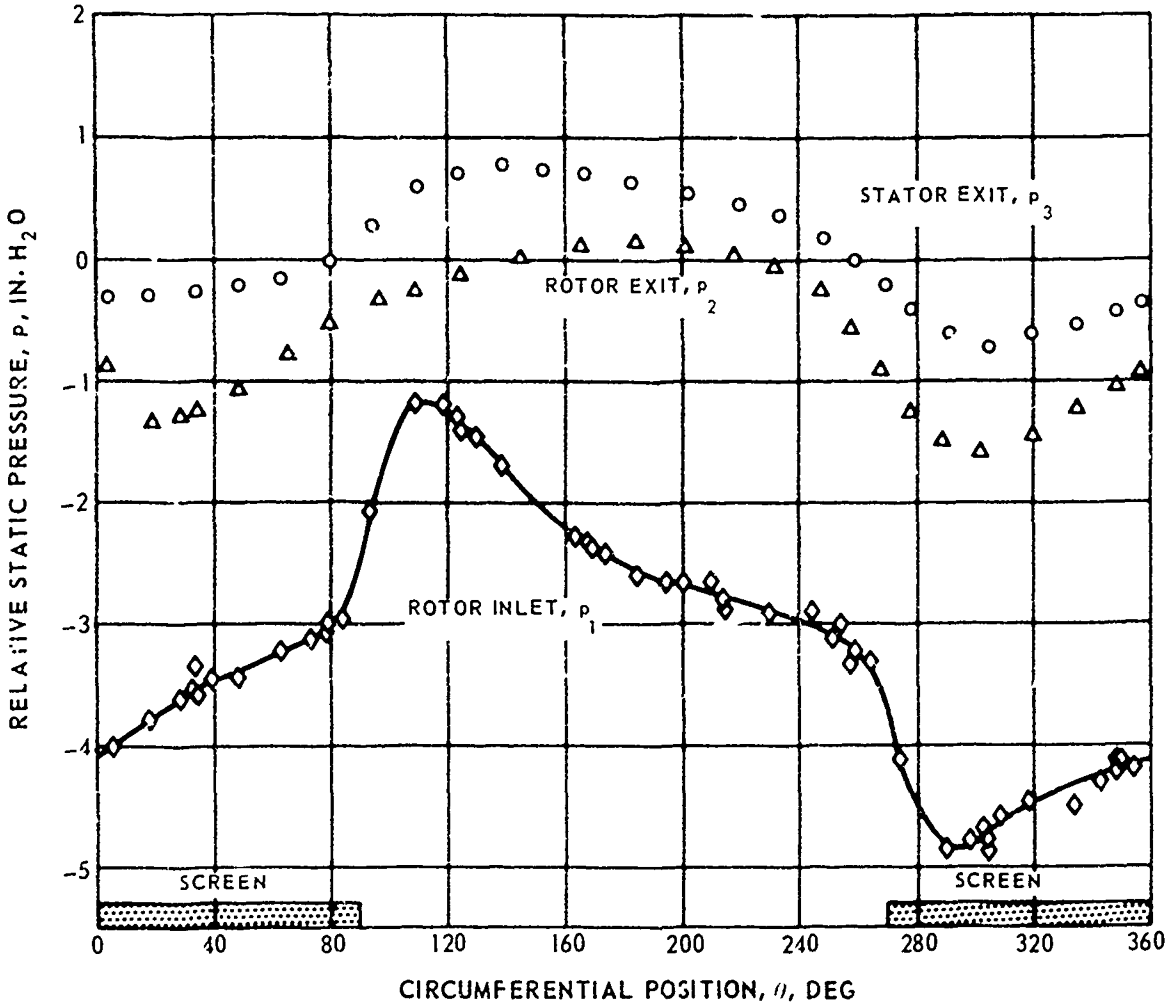

– 89

MEASURED CIRCUMFERENTIAL YAW ANGLE PROFILE AT MID-ANNULUS
FOR 180 DEG DISTORTION EXTENT – MIDFLOW CONDITION

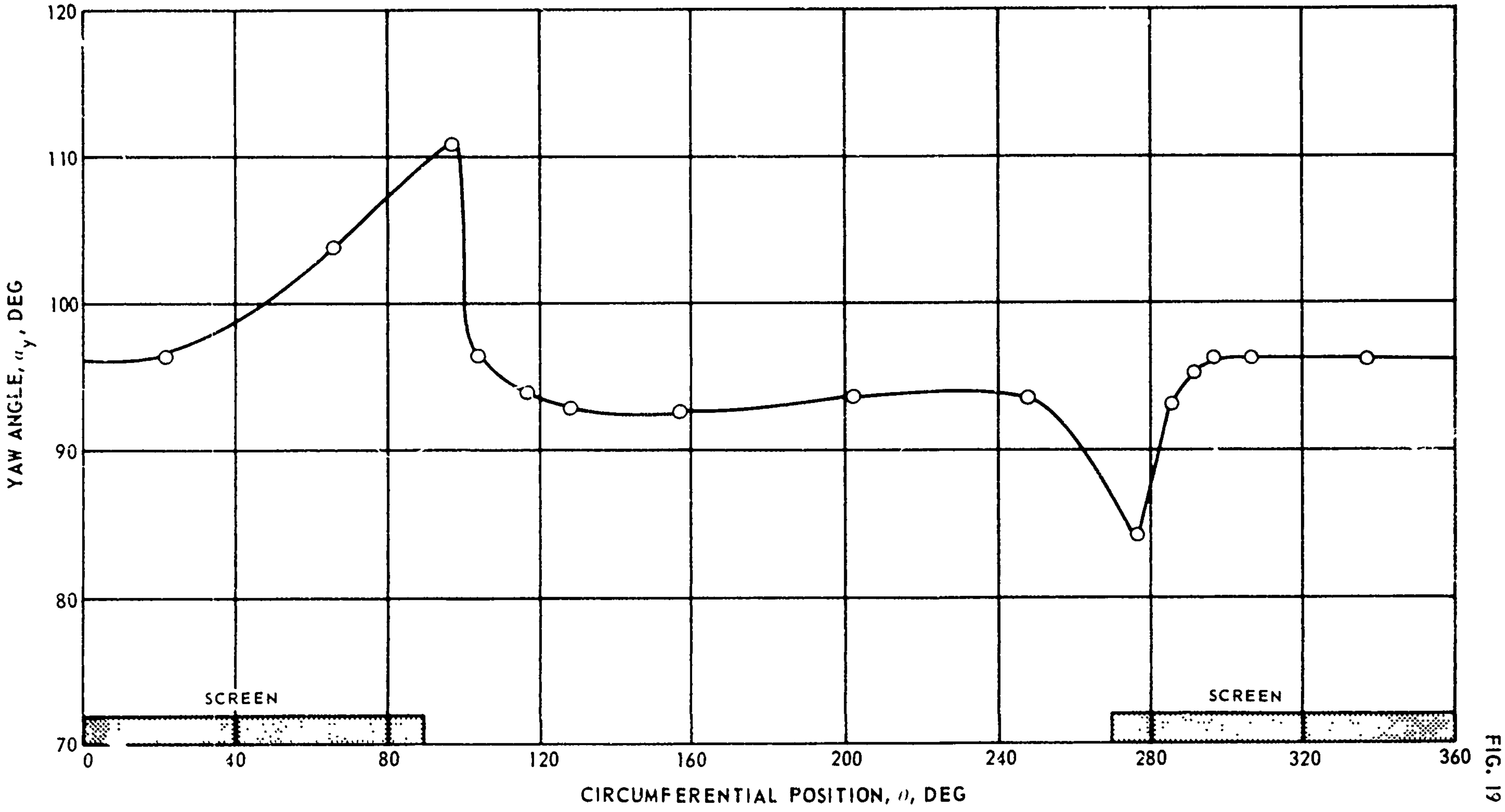

FIG. 19

COMPARISON BETWEEN PREDICTED AND MEASURED MID-ANNULUS STATIC PRESSURE COEFFICIENT AT ROTOR EXIT PLANE FOR 180 DEG DISTORTION EXTENT – MIDFLOW CONDITION

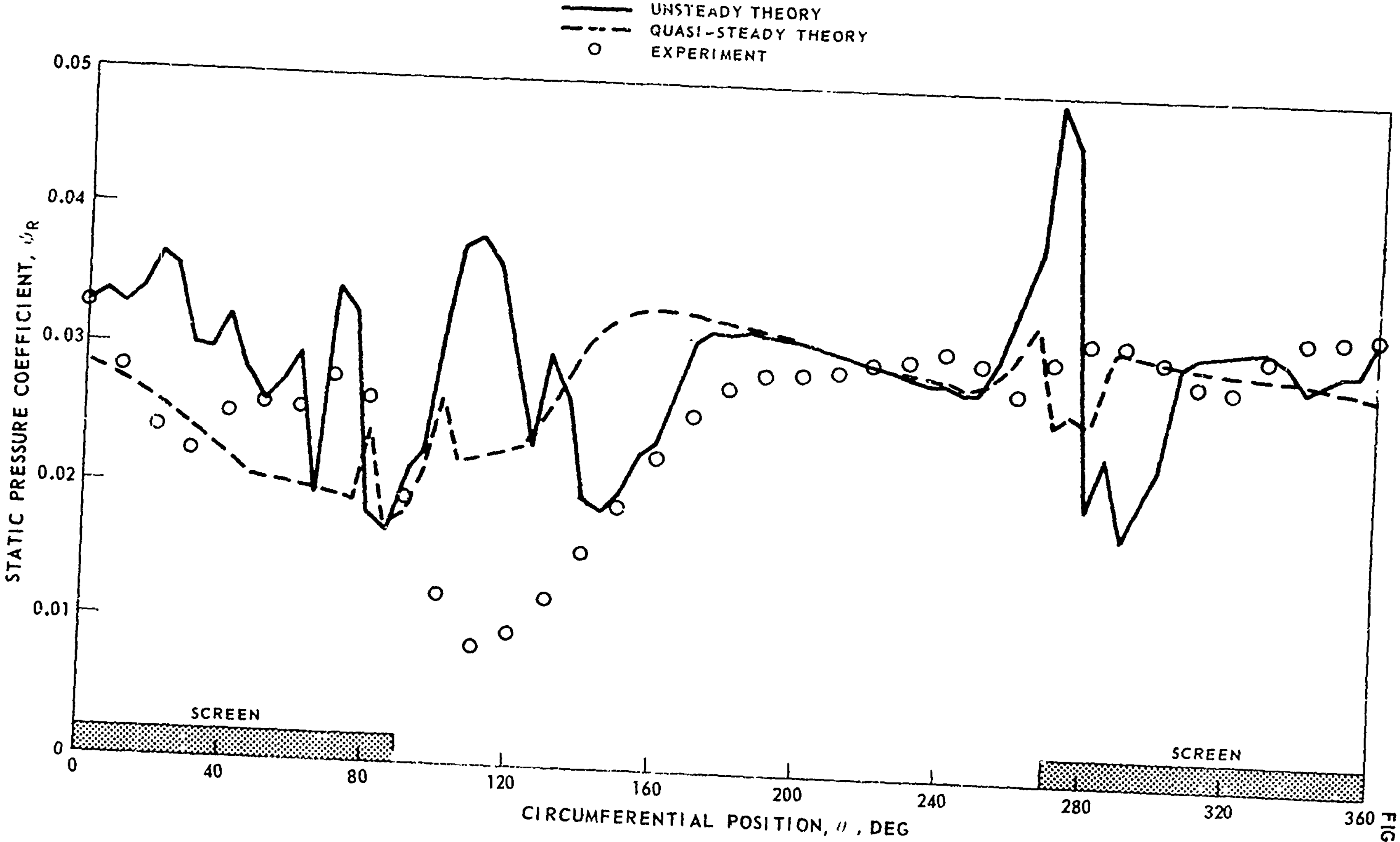

FIG. 20

MEASURED CIRCUMFERENTIAL TOTAL PRESSURE PROFILE AT MID-ANNULUS FOR 180 DEG DISTORTION EXTENT - NEAR SURGE

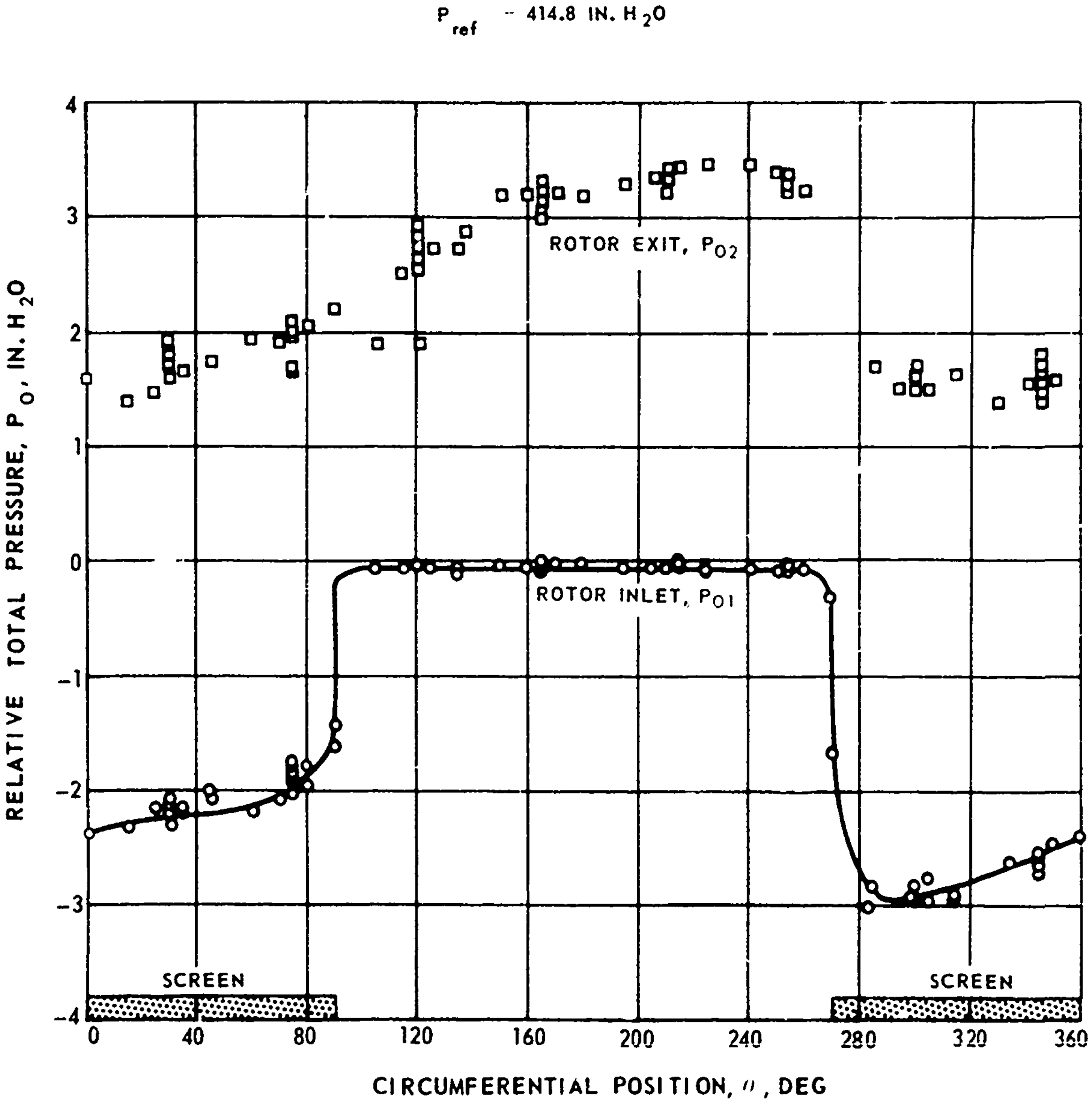

MEASURED CIRCUMFERENTIAL STATIC PRESSURE PROFILE AT OUTER DIAMETER FOR 180 DEG DISTORTION EXTENT – NEAR SURGE

$P_{ref} = 414.8$ IN. H_2O

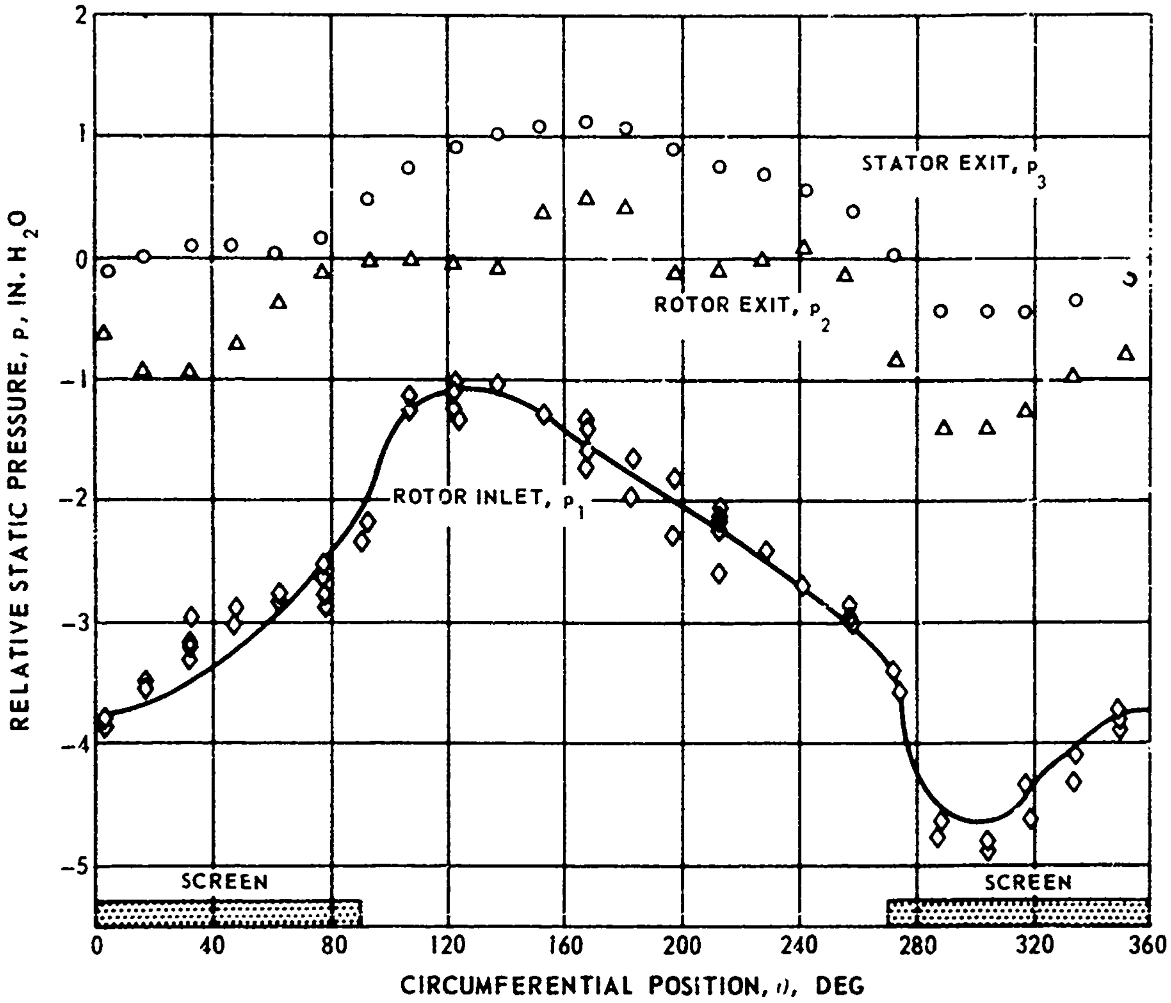

MEASURED CIRCUMFERENTIAL YAW ANGLE PROFILE AT MID-ANNULUS FOR 180 DEG DISTORTION EXTENT – NEAR SURGE

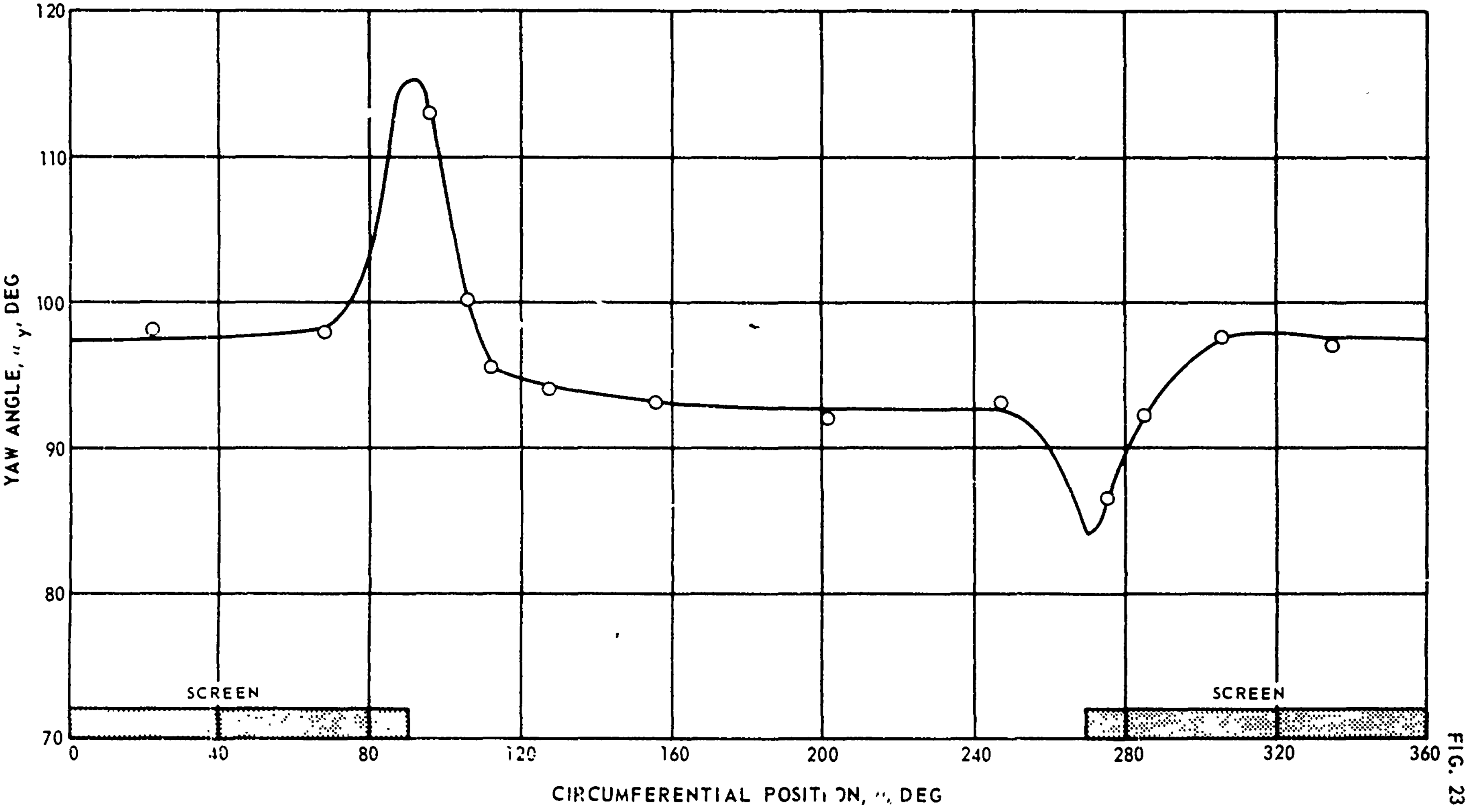

FIG. 23

COMPARISON BETWEEN PREDICTED AND MEASURED MID-ANNULUS STATIC PRESSURE COEFFICIENT AT ROTOR EXIT PLANE FOR 180 DEG DISTORTION EXTENT – NEAR SURGE

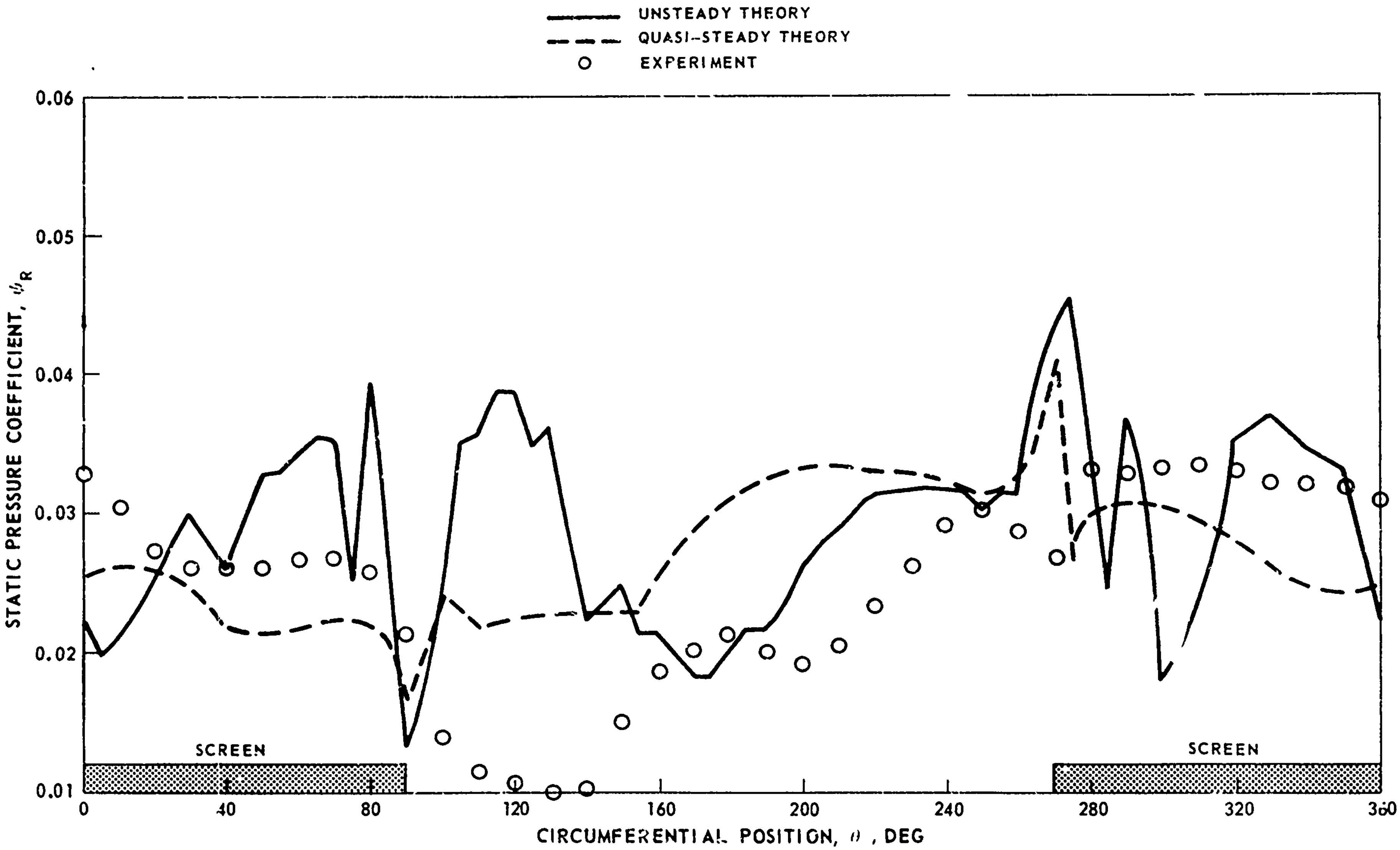

FIG. 24

FIG. 25

MEASURED CIRCUMFERENTIAL TOTAL PRESSURE PROFILE AT MID-ANNULUS FOR 135 DEG DISTORTION EXTENT – PEAK PRESSURE CONDITION

P_{ref} = 406.68 IN. H_2O

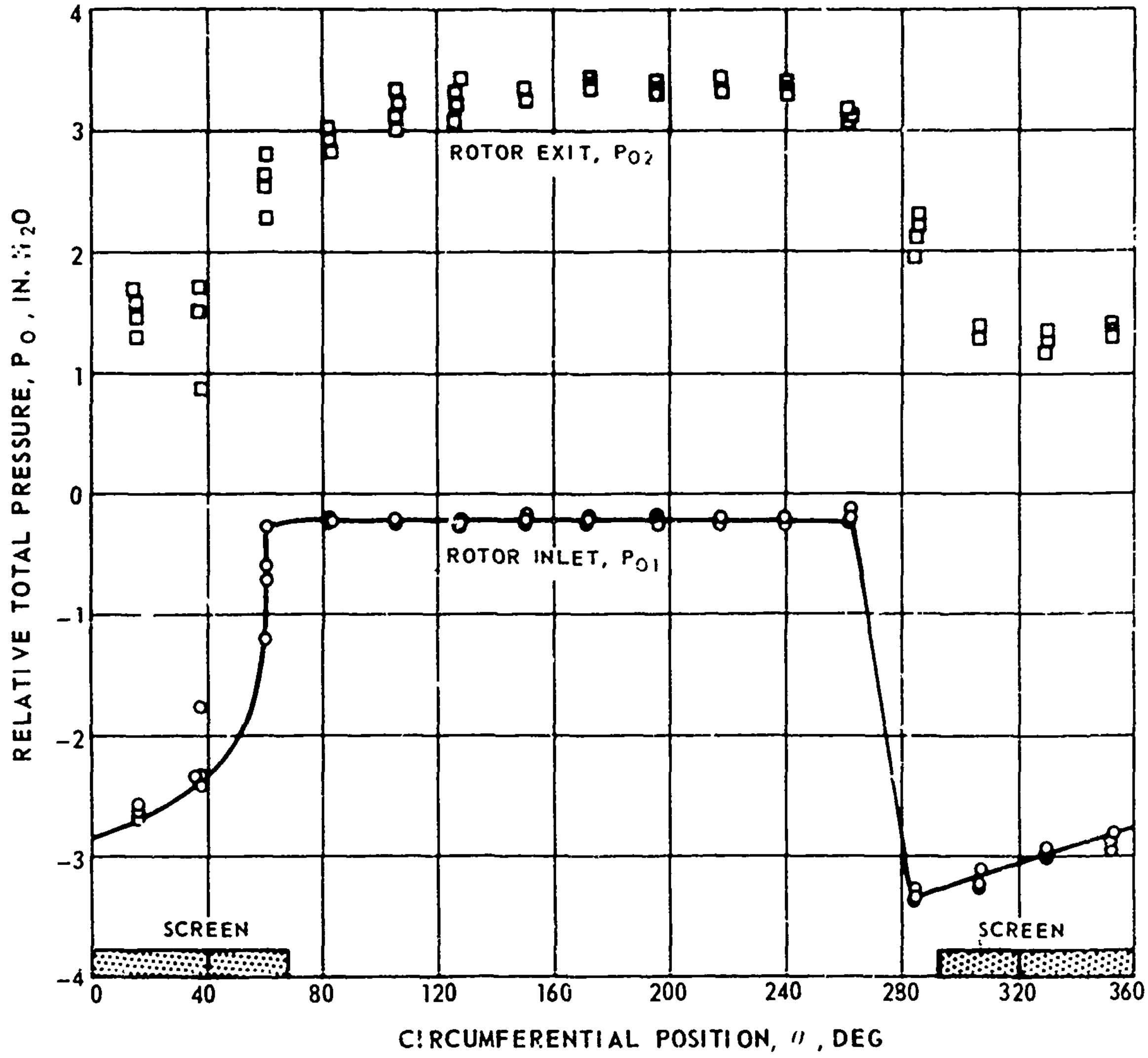

- 96 -

MEASURED CIRCUMFERENTIAL STATIC PRESSURE PROFILE AT OUTER DIAMETER FOR 135 DEG DISTORTION EXTENT – PEAK PRESSURE CONDITION

P_{ref} = 408.68 IN. H_2O

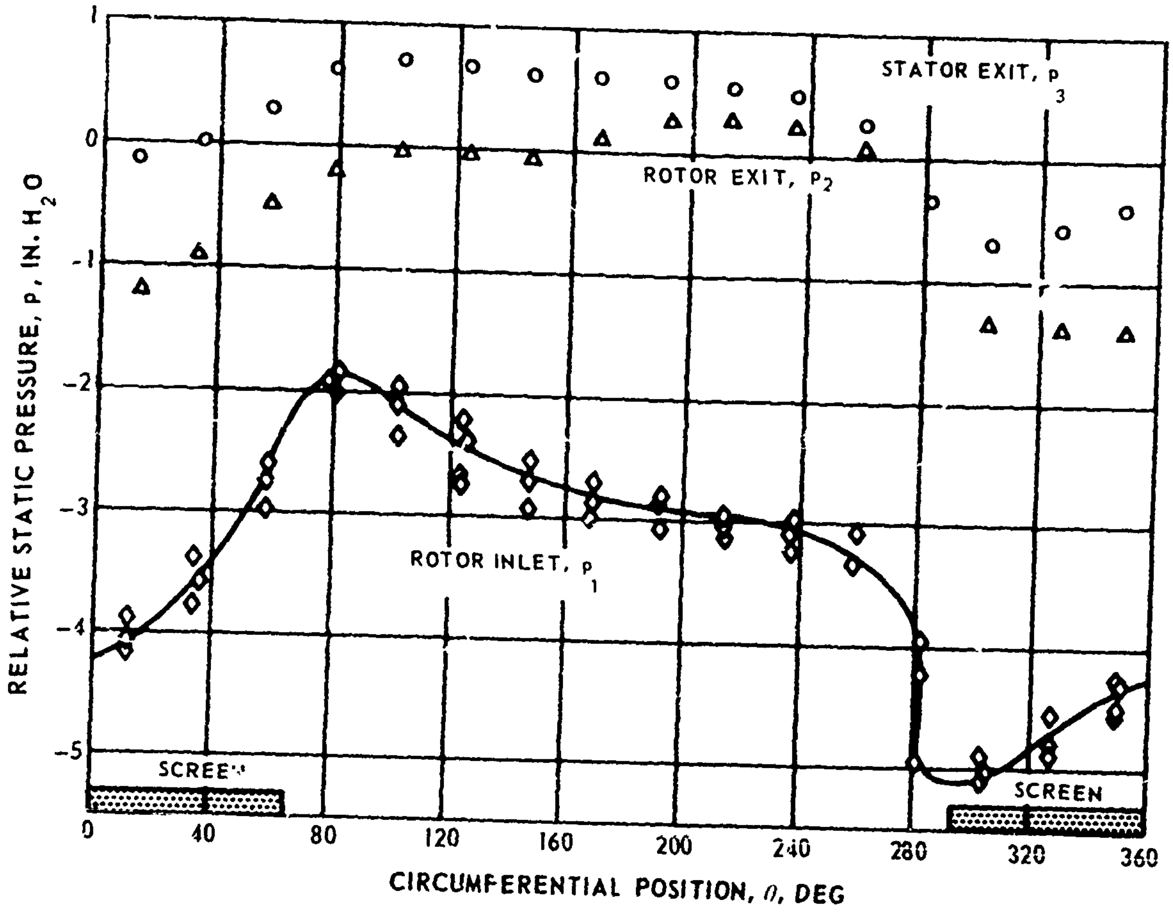

MEASURED CIRCUMFERENTIAL YAW ANGLE PROFILE AT MID-ANNULUS FOR 135 DEG DISTORTION EXTENT - PEAK PRESSURE CONDITION

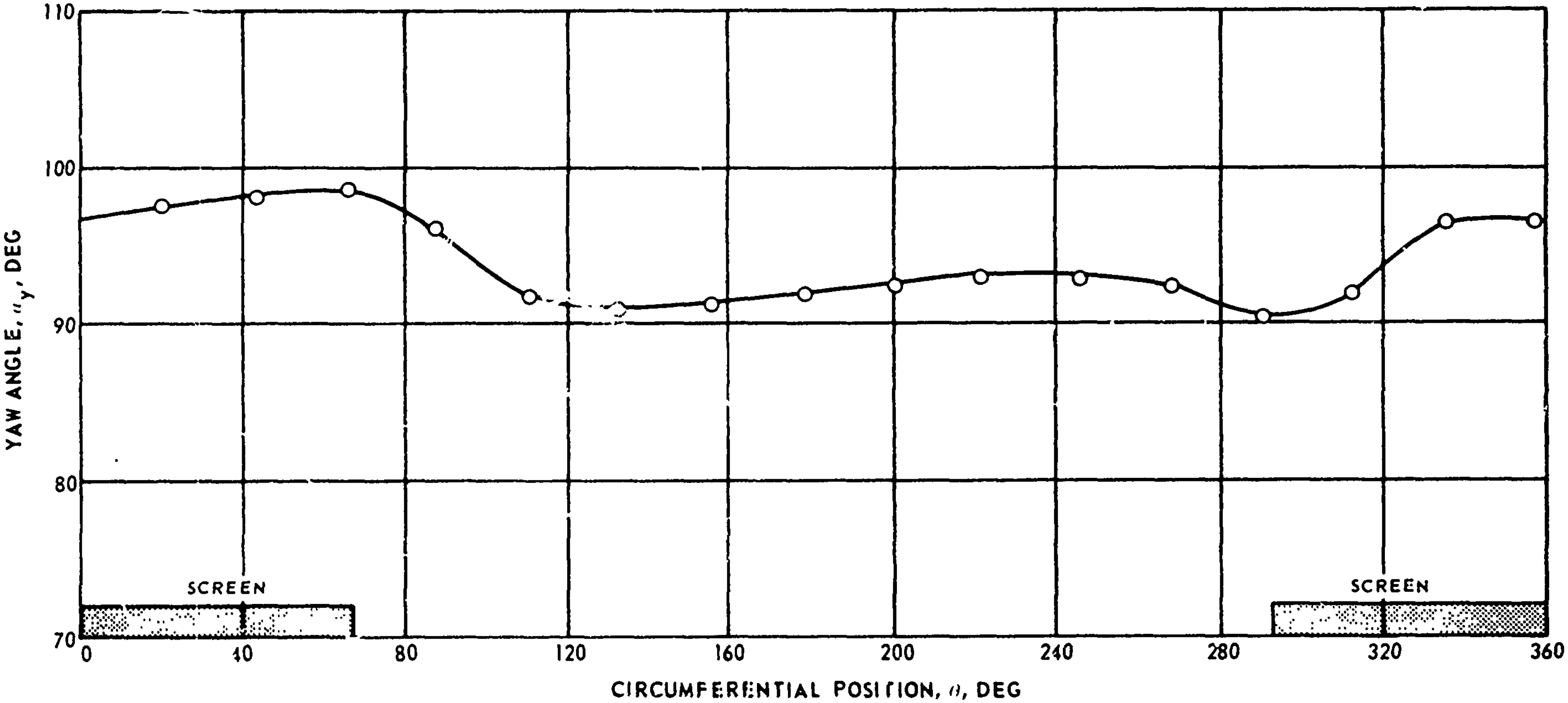

FIG. 27

FIG. 28

COMPARISON BETWEEN PREDICTED AND MEASURED MID-ANNULUS STATIC PRESSURE COEFFICIENT AT ROTOR EXIT PLANE FOR 135 DEG DISTORTION EXTENT – PEAK PRESSURE CONDITION

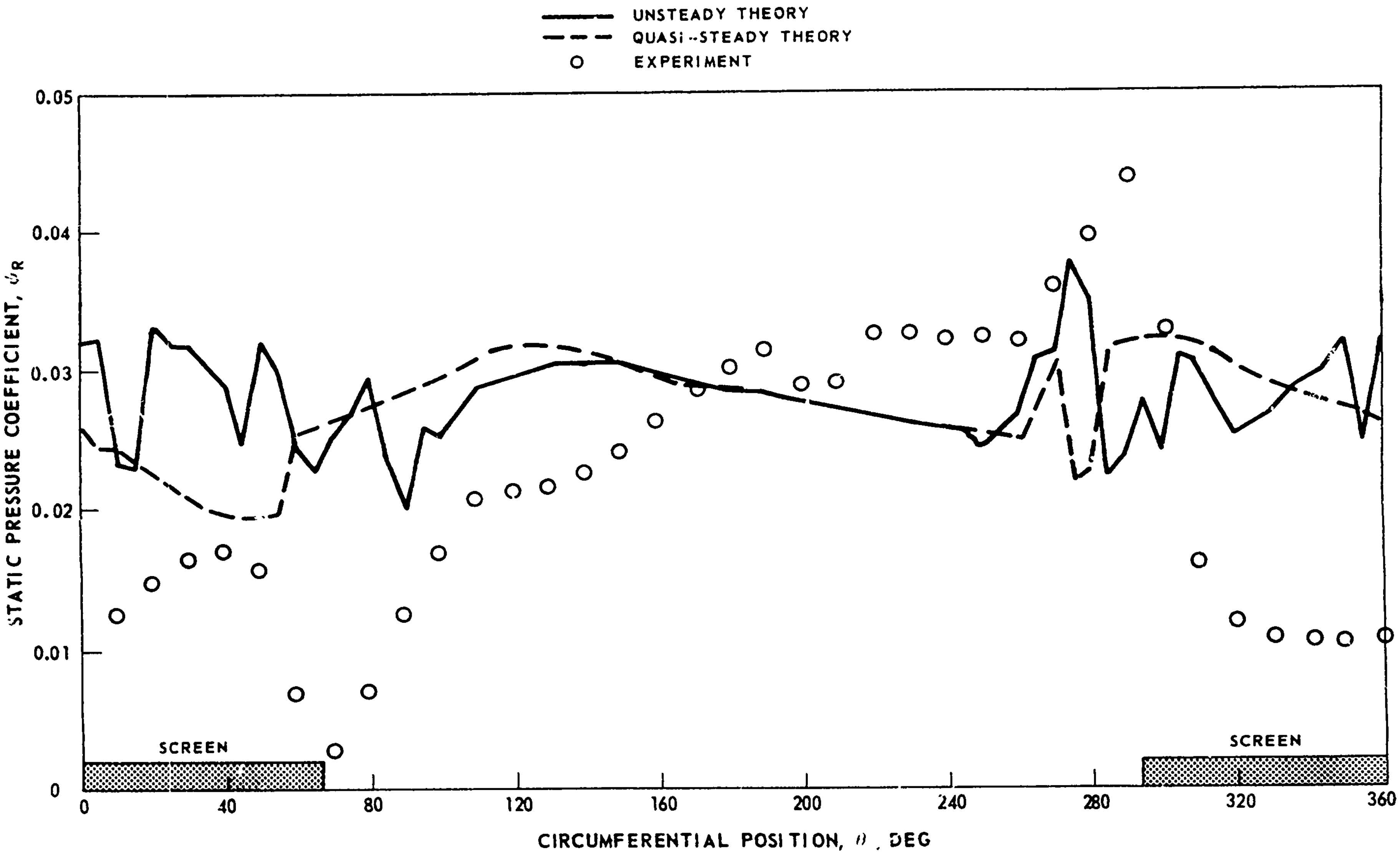

FIG. 29

MEASURED CIRCUMFERENTIAL TOTAL PRESSURE PROFILE AT MID-ANNULUS FOR 90 DEG DISTORTION EXTENT – NEAR SURGE

P_{ref} = 408.41 IN. H_2O

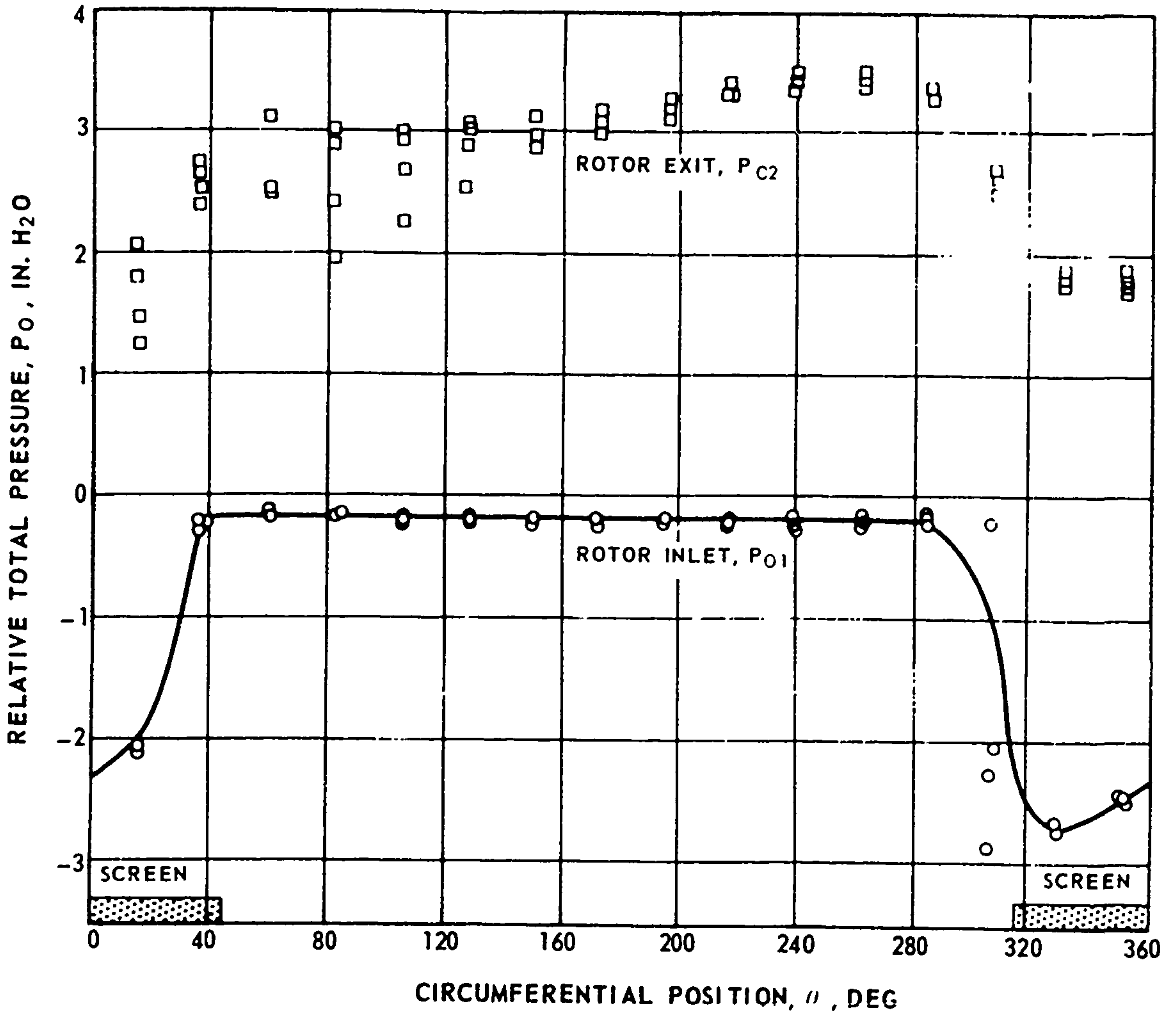

MEASURED CIRCUMFERENTIAL STATIC PRESSURE PROFILE AT OUTER DIAMETER FOR 90 DEG DISTORTION EXTENT – NEAR SURGE

P_{ref} = 408.41 IN. H_2O

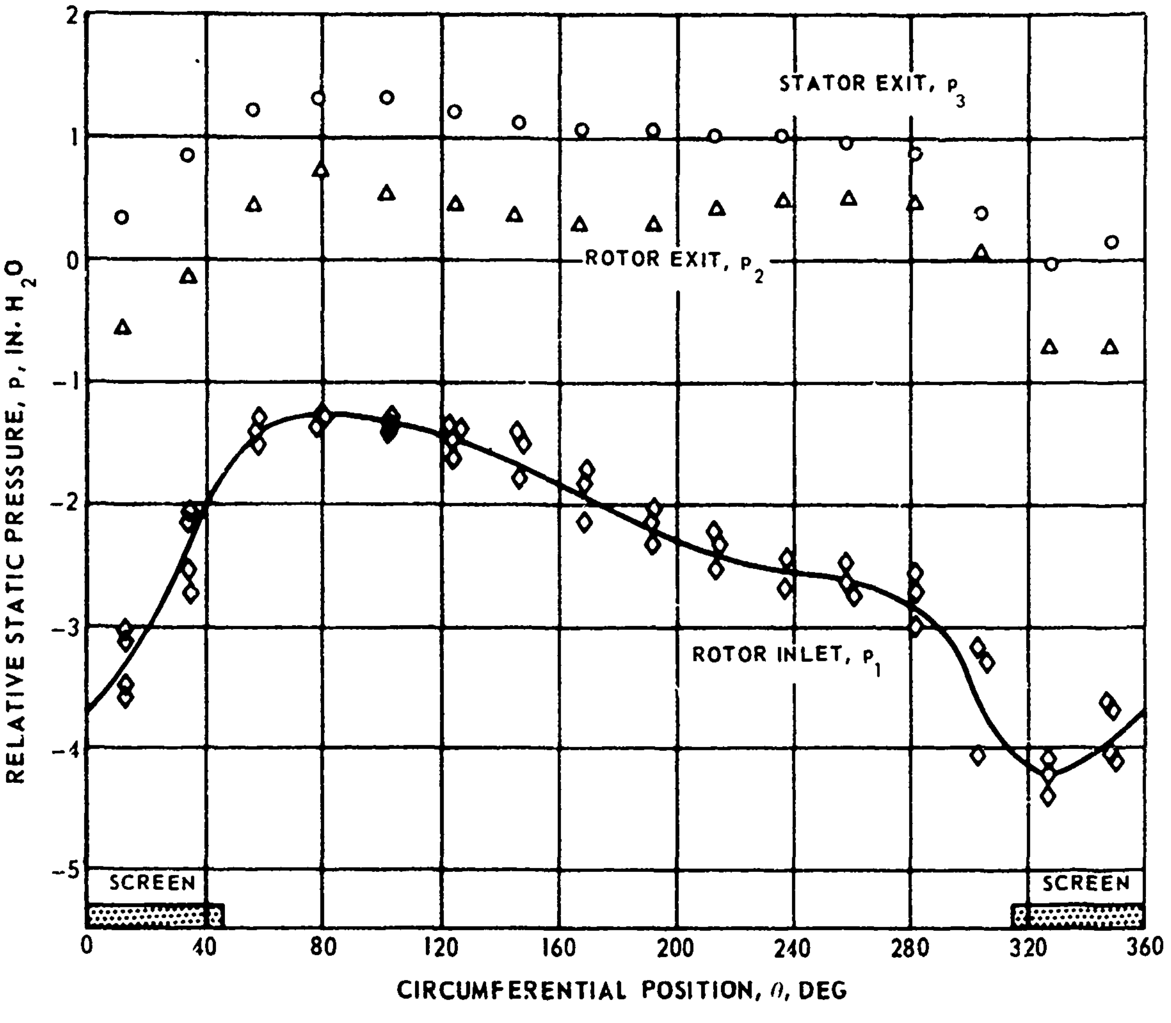

MEASURED CIRCUMFERENTIAL YAW ANGLE PROFILE AT MID-ANNULUS
FOR 90 DEG DISTORTION EXTENT - NEAR SURGE

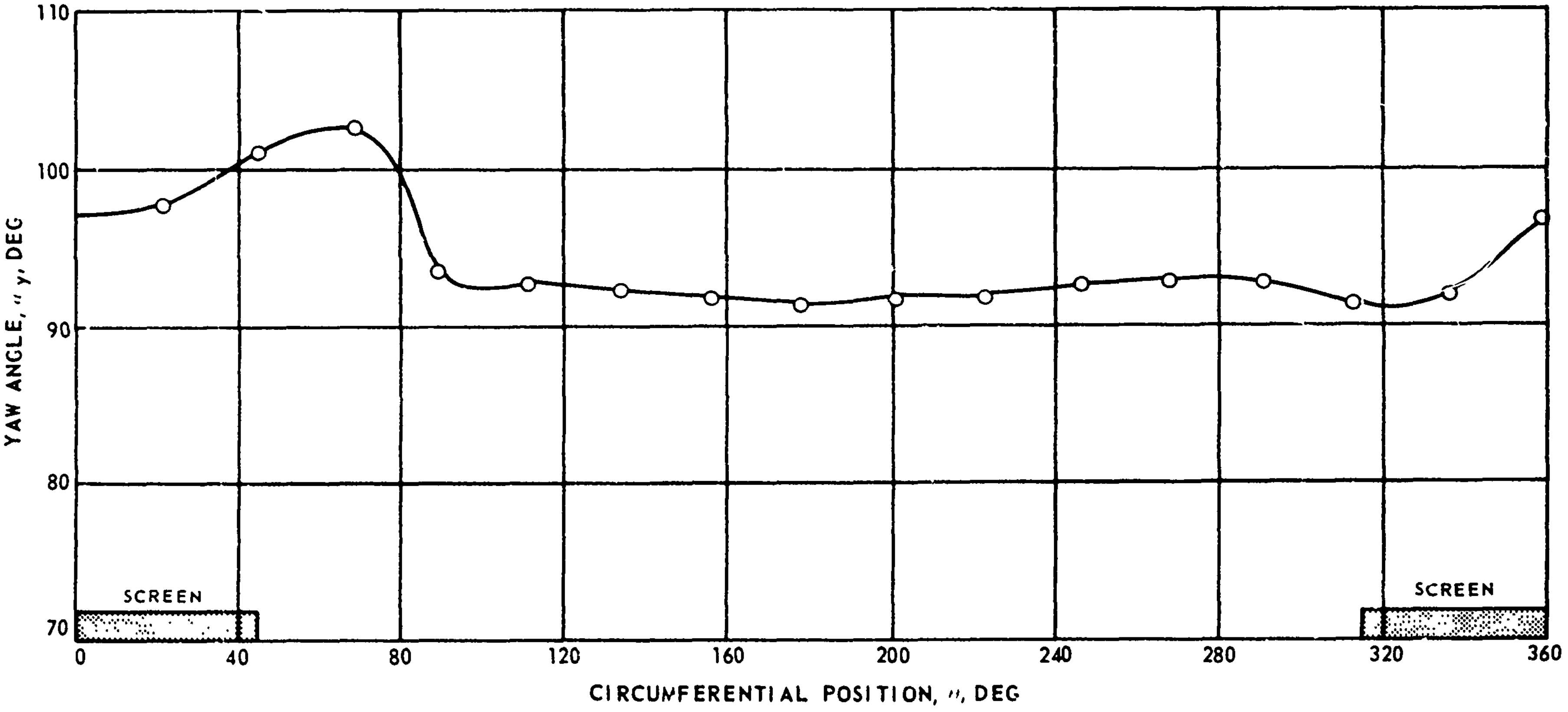

FIG. 31

COMPARISON BETWEEN PREDICTED AND MEASURED MID-ANNULUS STATIC PRESSURE COEFFICIENT AT ROTOR EXIT PLANE FOR 90 DEG DISTORTION EXTENT - NEAR SURGE

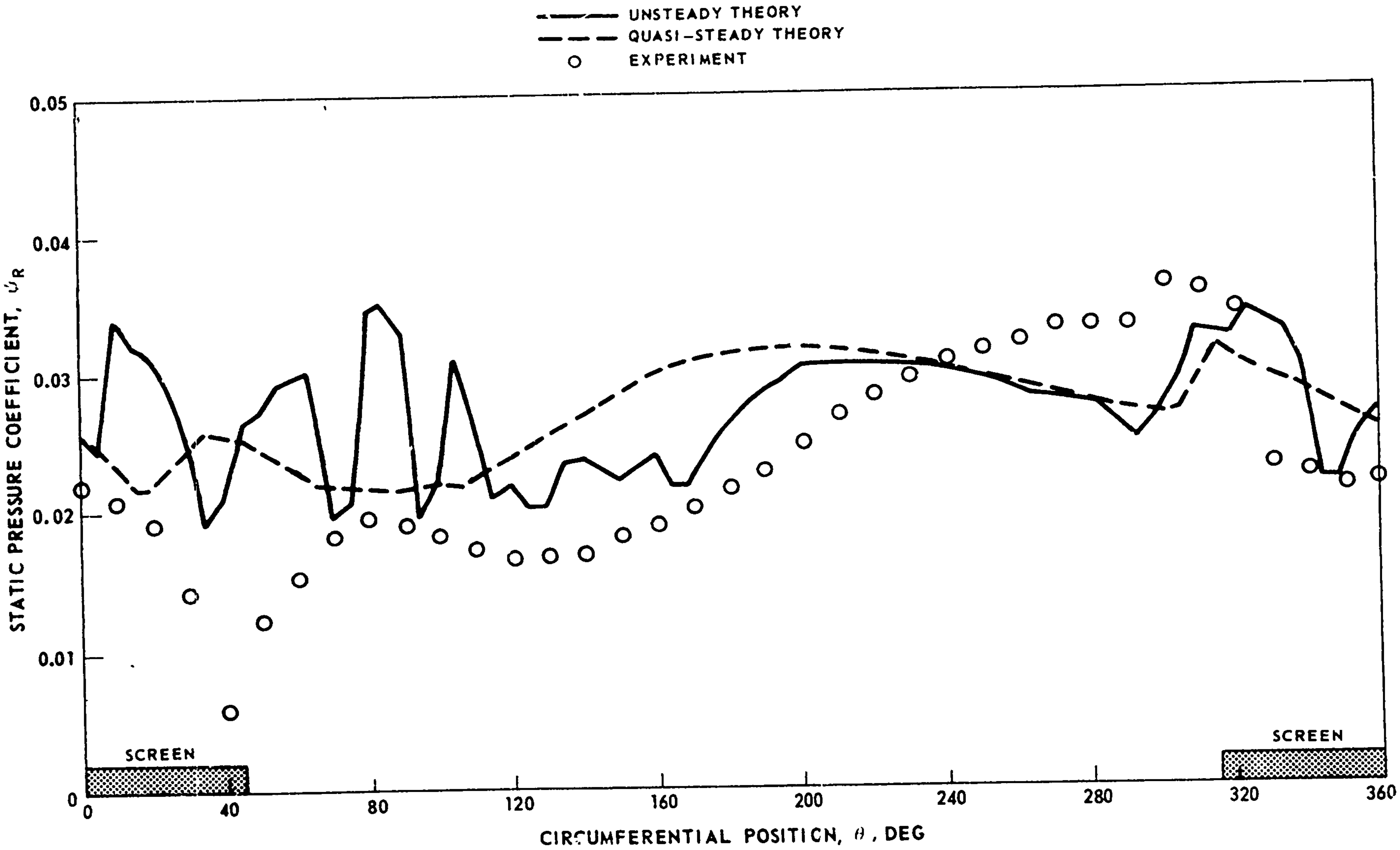

FIG. 32

FIG. 33

FIRST STAGE STATOR CHARACTERISTIC FROM UARL THREE-STAGE COMPRESSOR

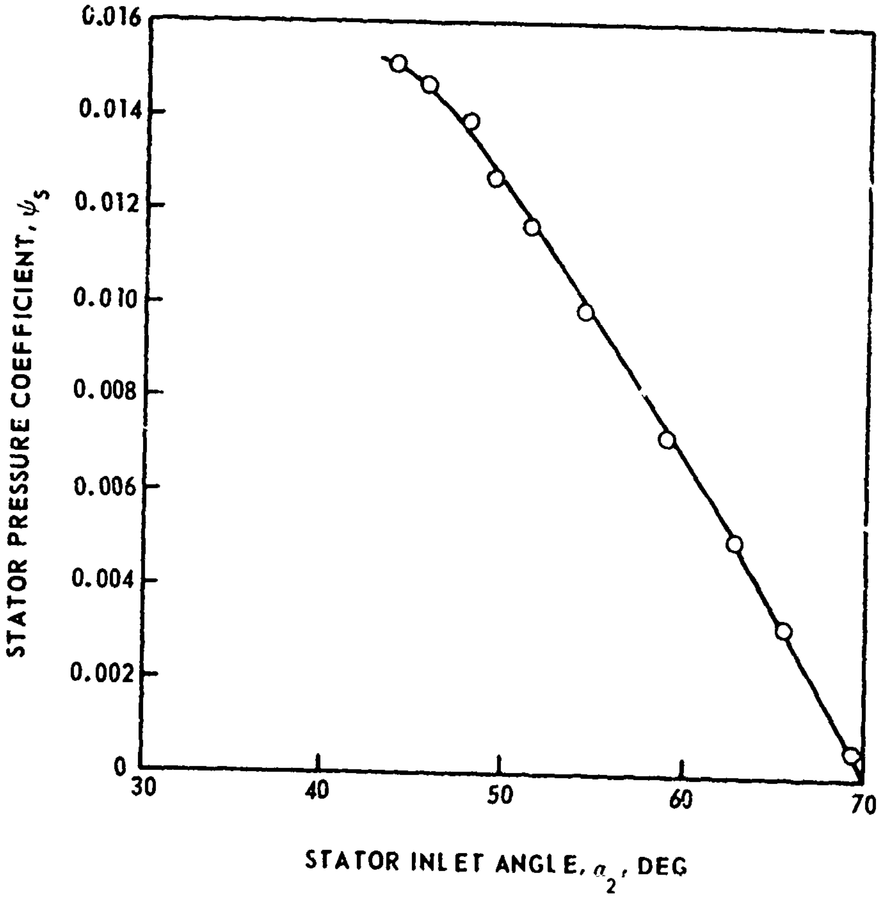

FIG. 34

COMPARISON BETWEEN PREDICTED AND MEASURED MID-ANNULUS STATIC PRESSURE AT STAGE EXIT PLANE FOR 180 DEG DISTORTION EXTENT – PEAK PRESSURE CONDITION

P_{ref} 404.33 IN.H_2O

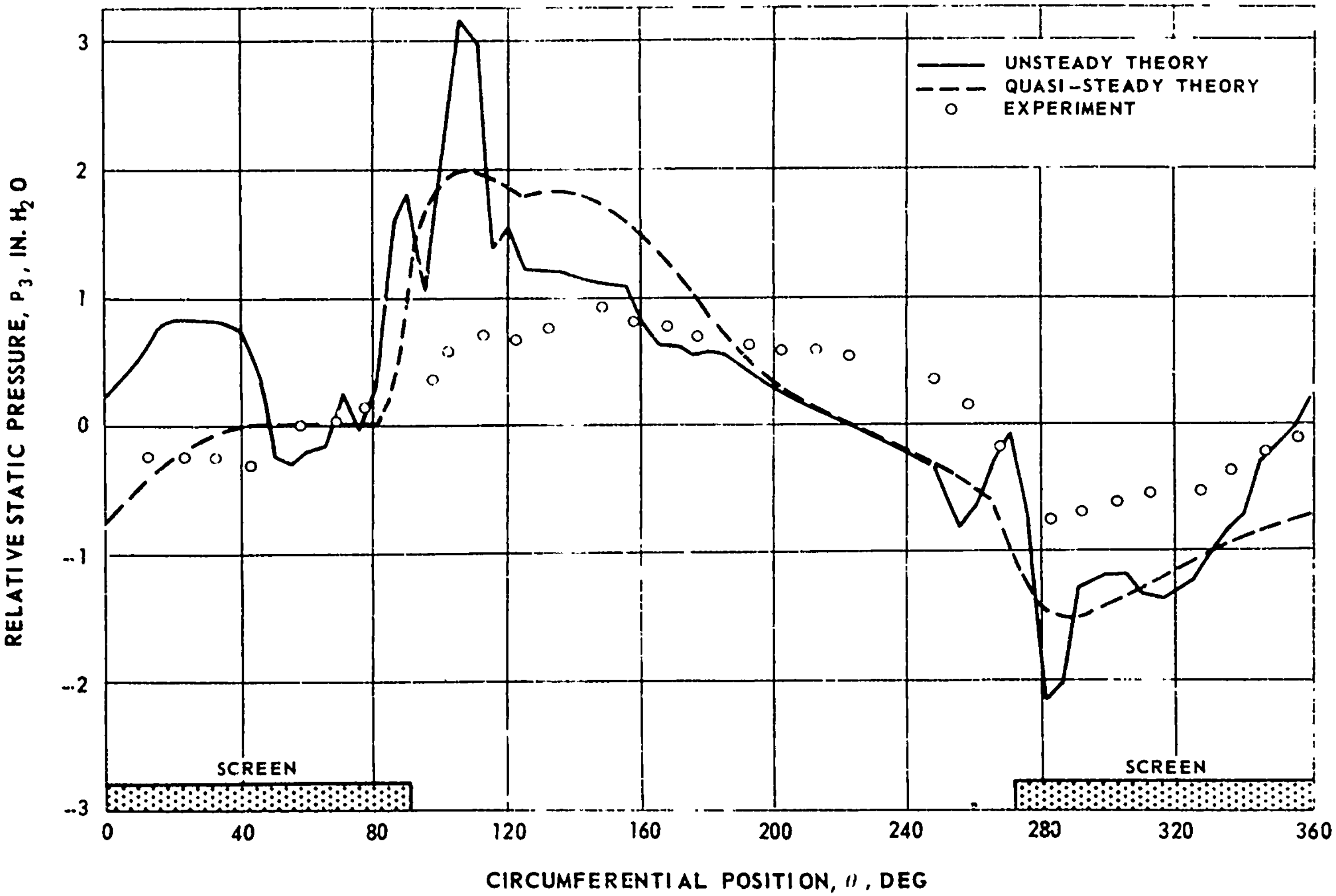

FIG. 35

COMPARISON BETWEEN PREDICTED AND MEASURED MID-ANNULUS STATIC PRESSURE AT STAGE EXIT PLANE FOR 180 DEG DISTORTION EXTENT – MIDFLOW CONDITION

P_{ref} – 415.1 IN.H_2O

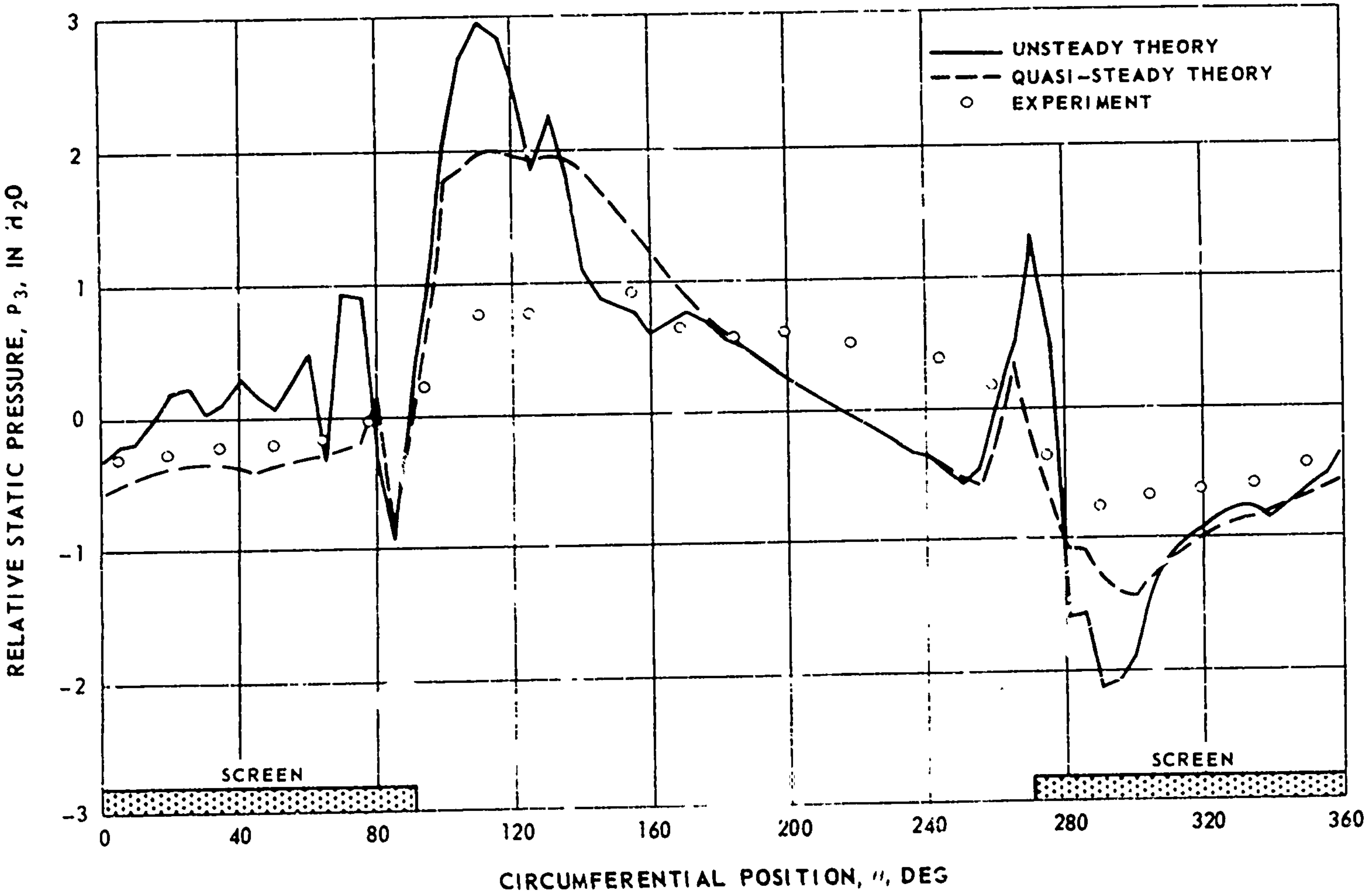

FIG. 36

COMPARISON BETWEEN PREDICTED AND MEASURED MID-ANNULUS STATIC PRESSURE AT STAGE EXIT PLANE FOR 180 DEG DISTORTION EXTENT – PEAK PRESSURE CONDITION

P_{ref} 418.8 IN. H_2O

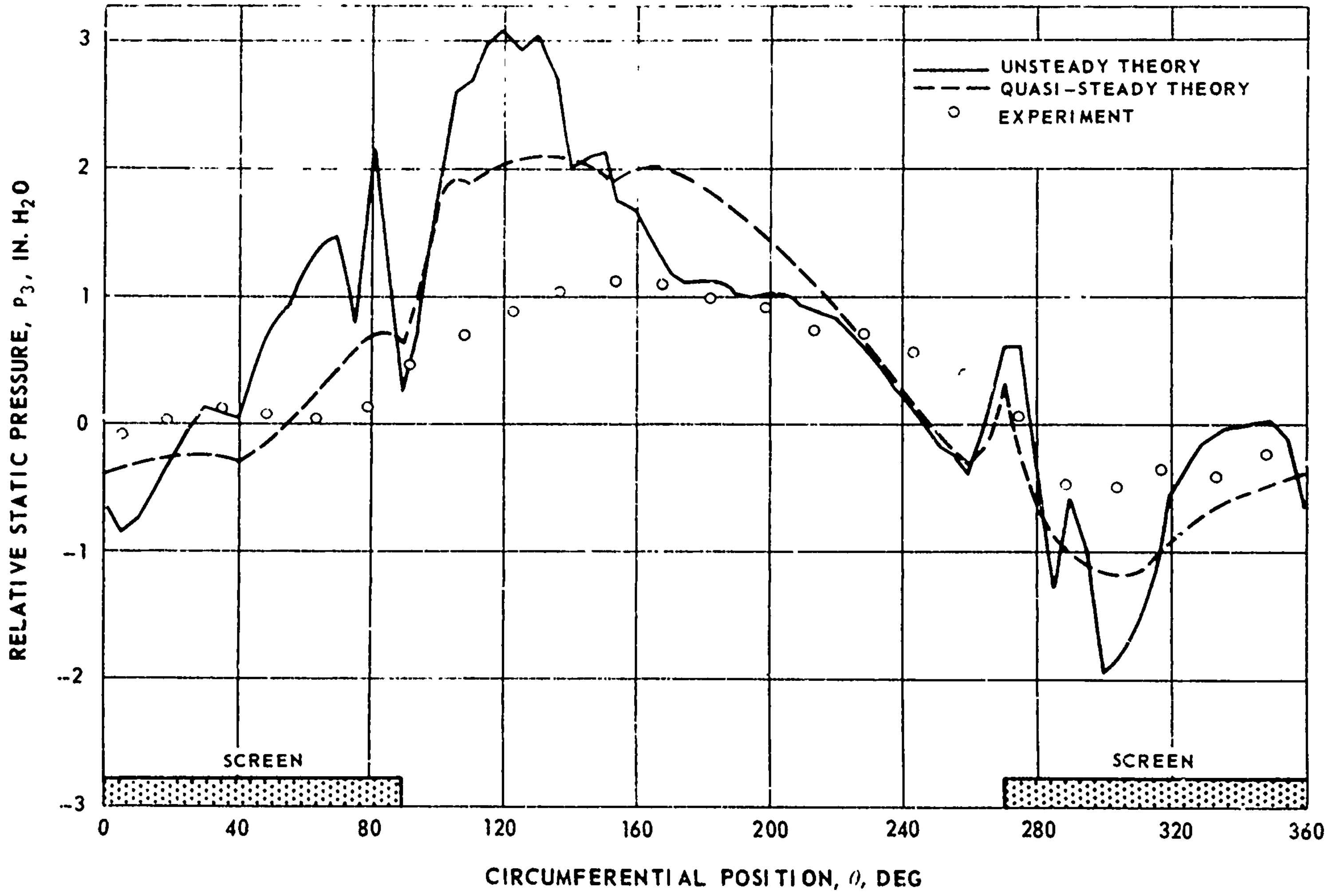

COMPARISON BETWEEN PREDICTED AND MEASURED MID-ANNULUS STATIC PRESSURE AT STAGE EXIT PLANE FOR 135 DEG DISTORTION EXTENT – PEAK PRESSURE CONDITION

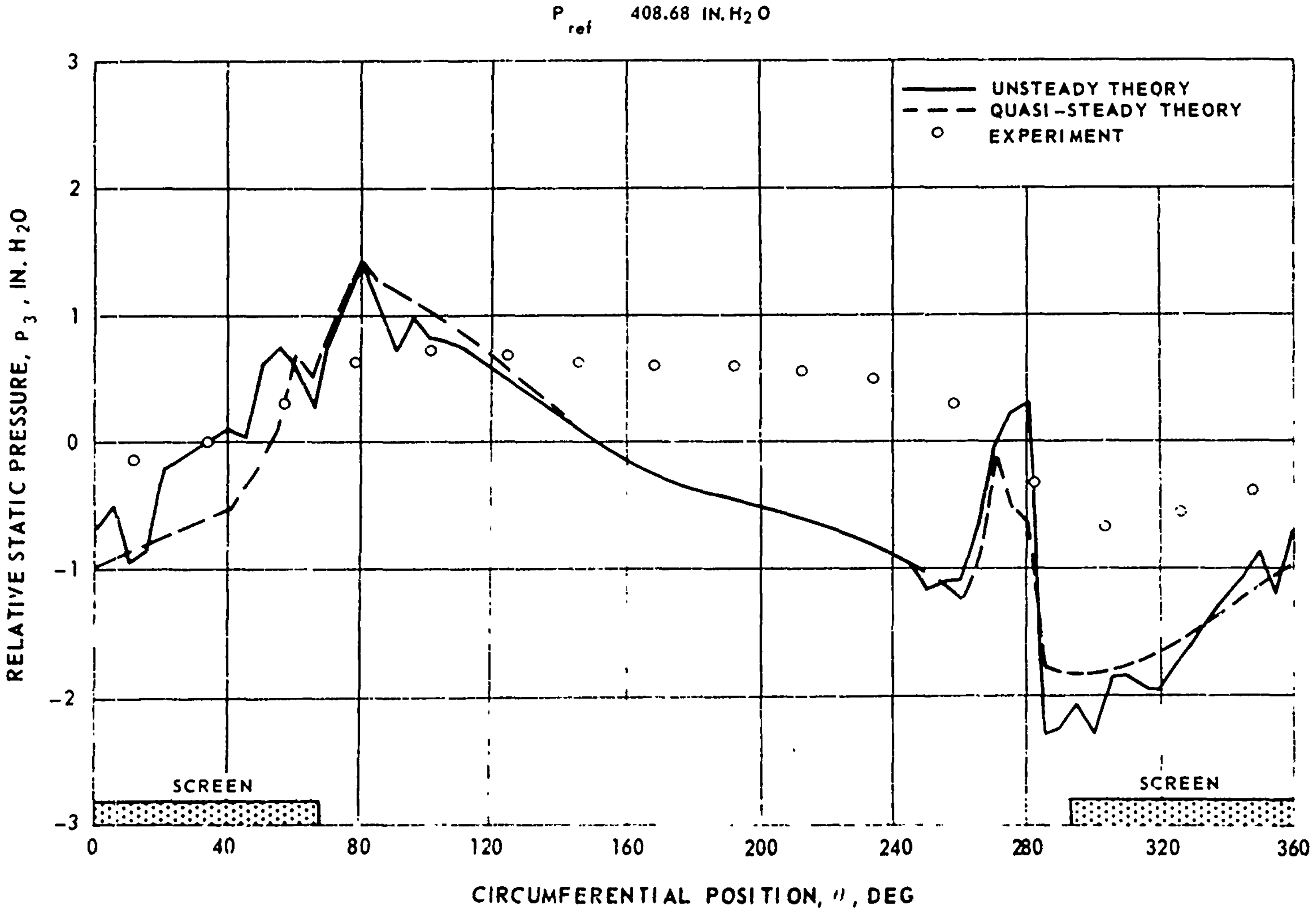

FIG. 37

FIG. 38

COMPARISON BETWEEN PREDICTED AND MEASURED MID-ANNULUS STATIC PRESSURE AT STAGE EXIT PLANE FOR 90 DEG DISTORTION EXTENT – NEAR SURGE

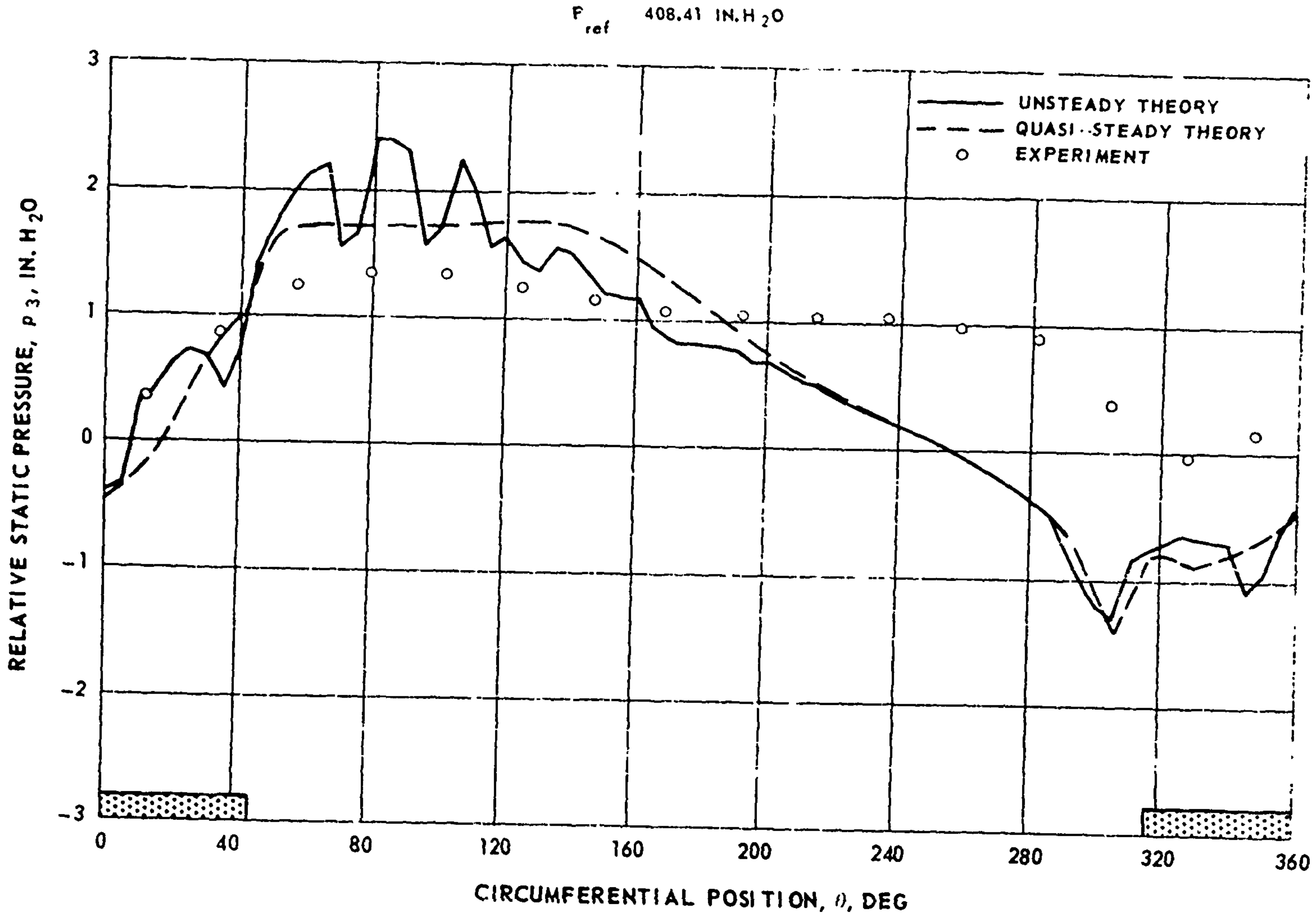

FIG. 39

INFLUENCE OF ROTOR ON UPSTREAM DISTORTION

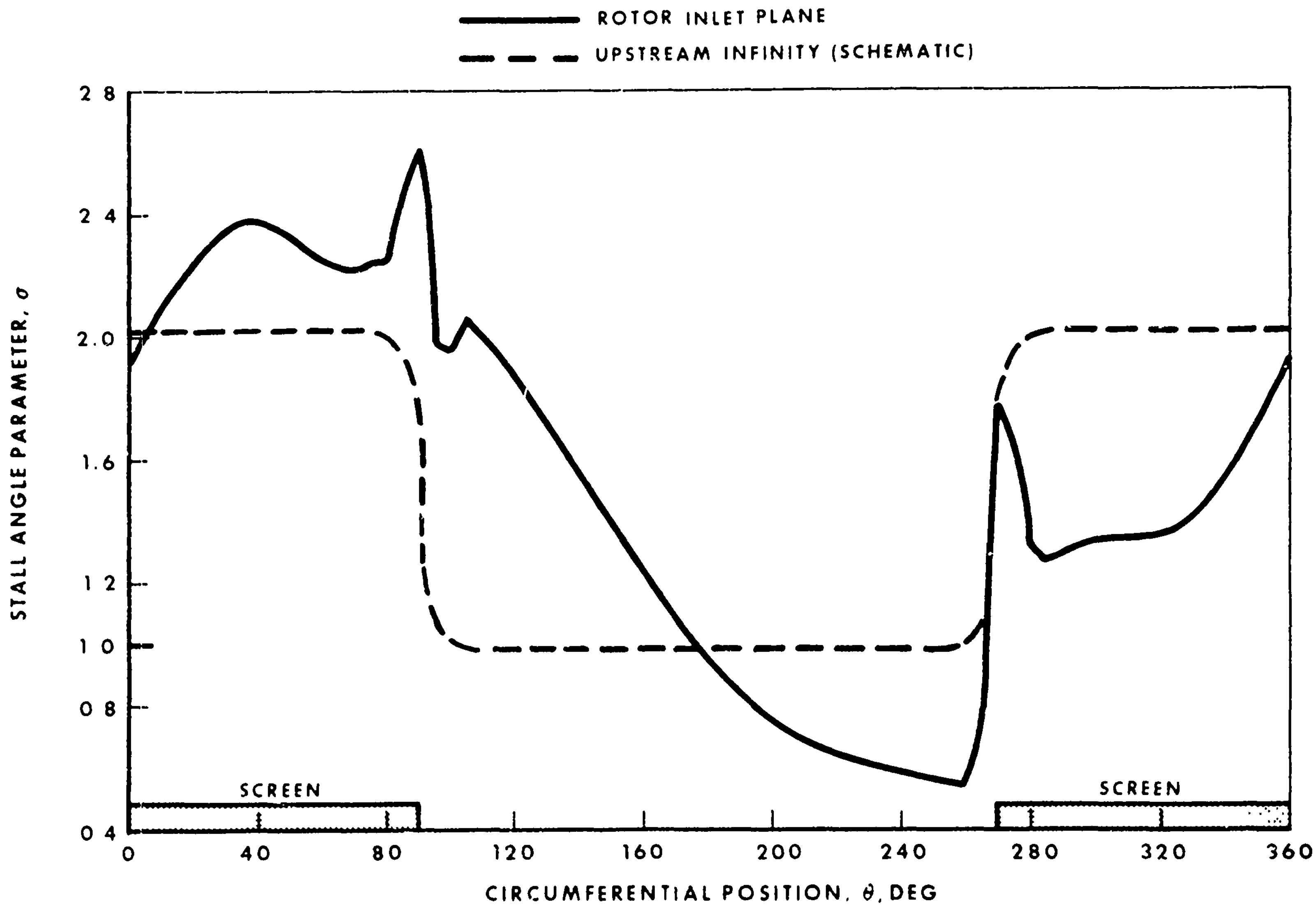

THIS
PAGE
IS
MISSING
IN
ORIGINAL
DOCUMENT

STEADY STATE LIFT AND DRAG COEFFICIENT ON ROTOR BLADE

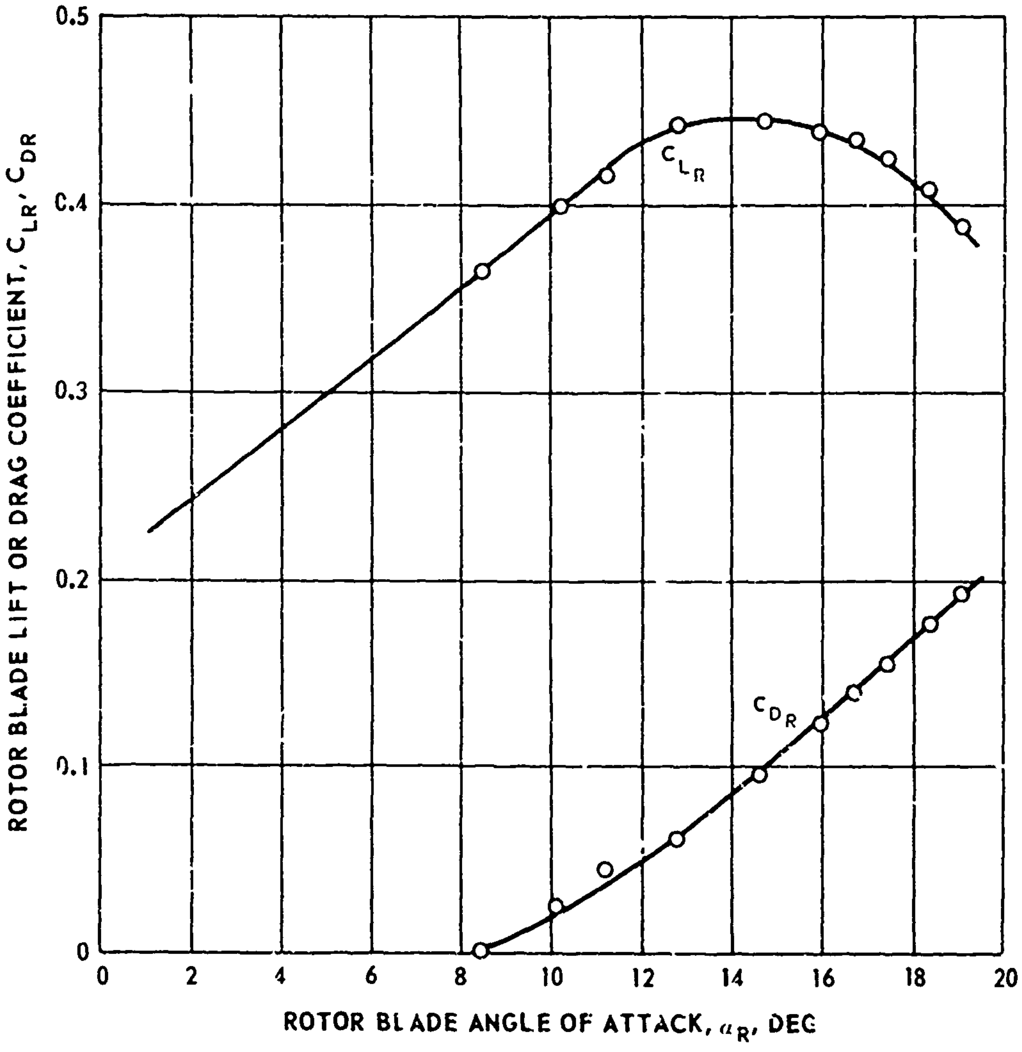

FIG. 41

ROTOR BLADE AND AIRFOIL LIFT - SCHEMATIC

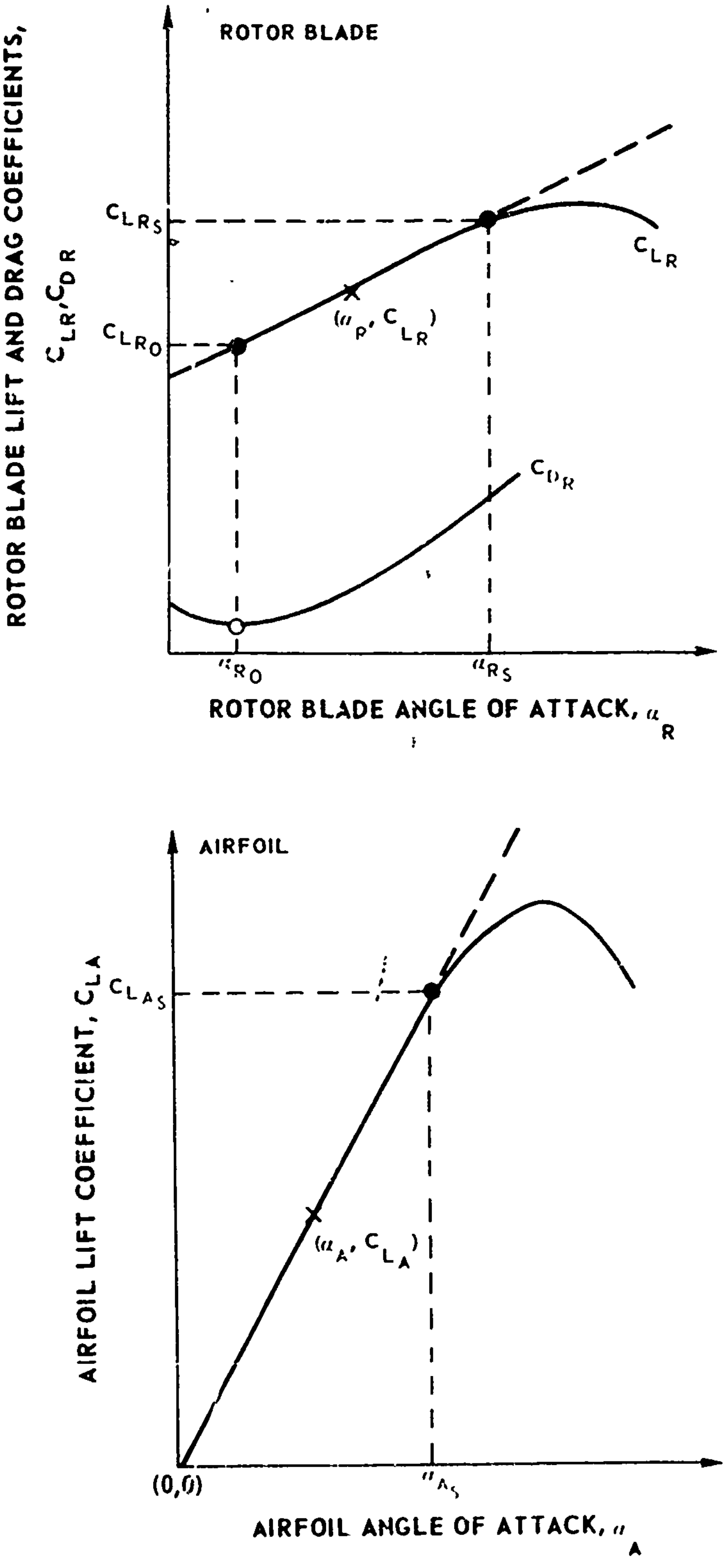

COMPARISON BETWEEN NORMALIZED ROTOR BLADE AND ISOLATED AIRFOIL LIFT COEFFICIENTS

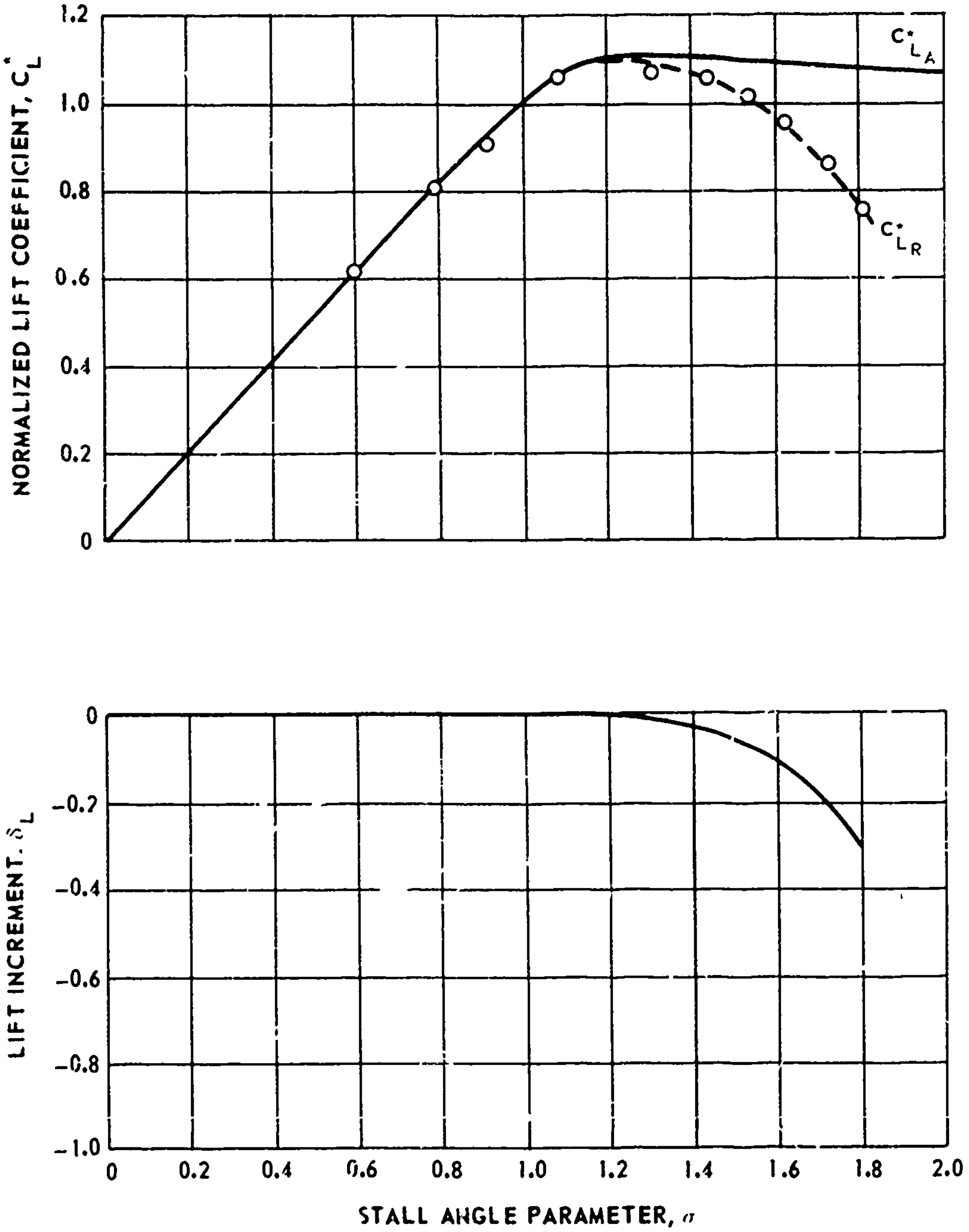

-115

COMPARISON BETWEEN ROTOR BLADE AND ISOLATED AIRFOIL DRAG COEFFICIENTS

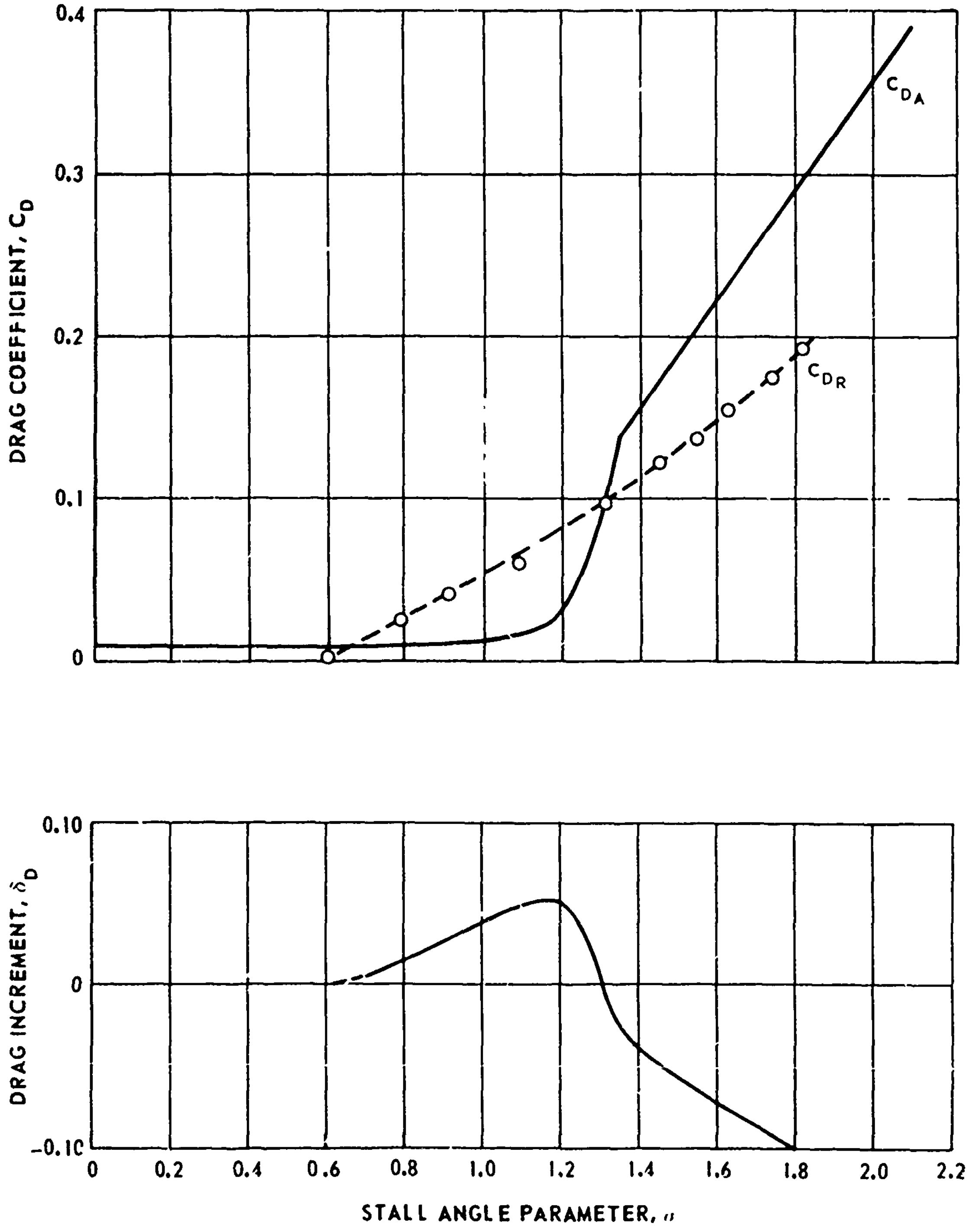

FIG. 44

HYPOTHETICAL MODEL TO OBTAIN STEADY STATE DRAG FROM LIFT

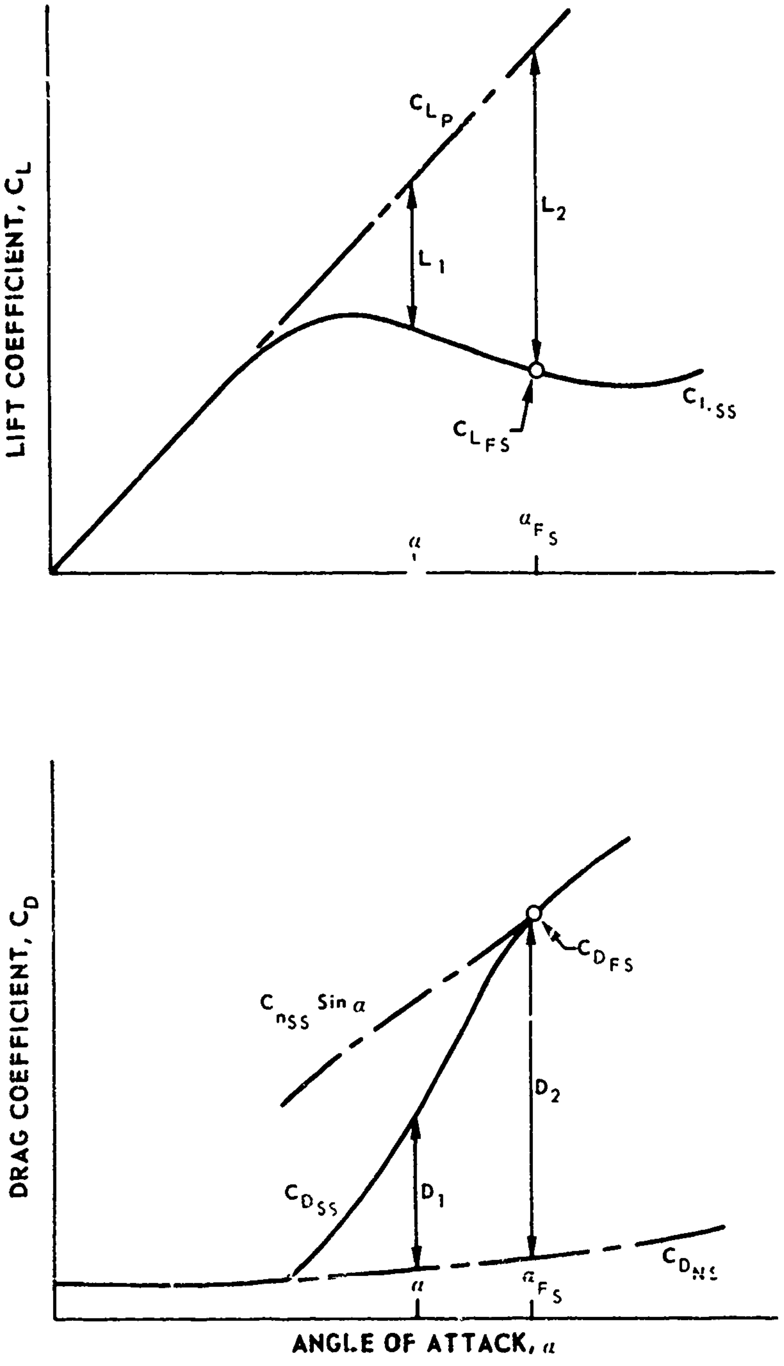

COMPARISON OF MEASURED AND COMPUTED STEADY-STATE DRAG

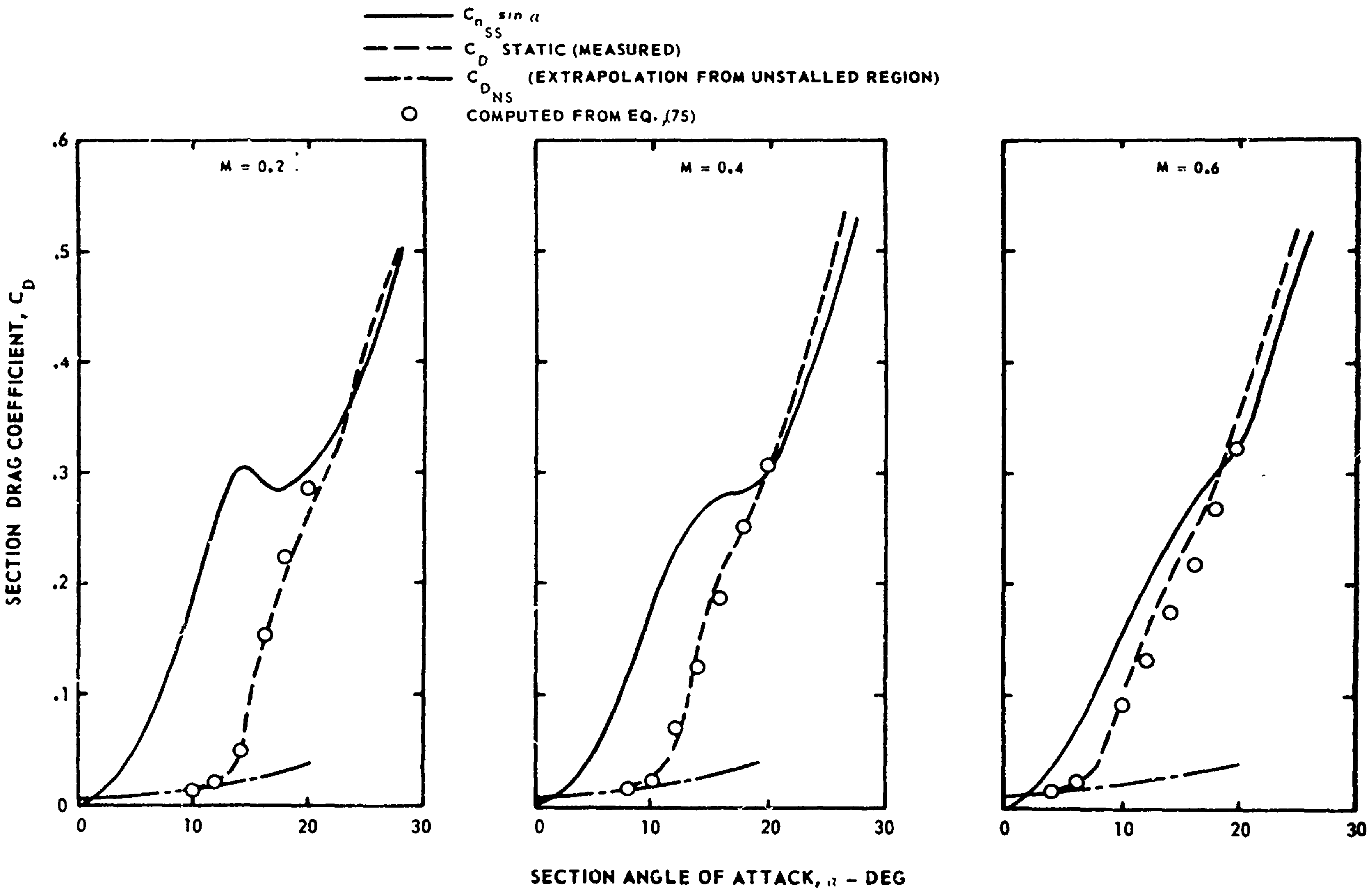

FIG. 45

FIG. 46

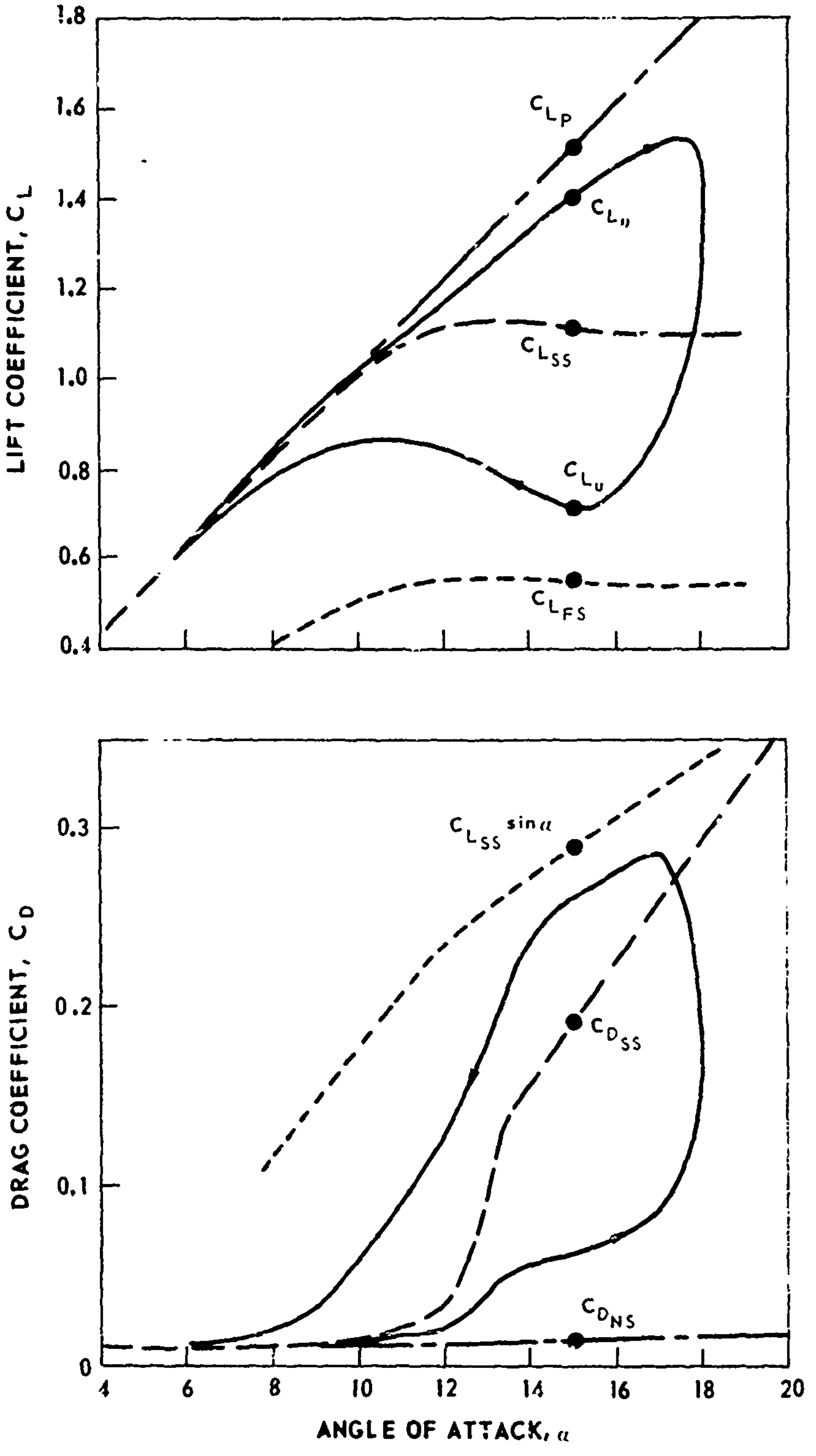TYPICAL UNSTEADY LIFT AND DRAG HYSTERESIS LOOPS